Control and Characterization of Organic Solar Cell Morphology Through Variable-Pressure Solvent Vapour Annealing

A Thesis Submitted to the College of

Graduate and Postdoctoral Studies

In Partial Fulfillment of the Requirements

For the Degree of Master of Science

In the Department of Chemistry

University of Saskatchewan

Saskatoon

By

Derek J. Zomerman

Permission to Use

In presenting this thesis in partial fulfillment of the requirements for a Postgraduate degree from the University of Saskatchewan, I agree that the Libraries of this University may make it freely available for inspection. I further agree that permission for copying of this thesis in any manner, in whole or in part, for scholarly purposes may be granted by the professor or professors who supervised my thesis work or, in their absence, by the Head of the Department or the Dean of the College in which my thesis work was done. It is understood that any copying or publication or use of this thesis or parts thereof for financial gain shall not be allowed without my written permission. It is also understood that due recognition shall be given to me and to the University of Saskatchewan in any scholarly use which may be made of any material in my thesis.

Requests for permission to copy or to make other uses of materials in this thesis in whole or part should be addressed to:

Head of the Department of Chemistry

University of Saskatchewan

170 Thorvaldson Building, 110 Science Place

Saskatoon, Saskatchewan S7N 5C9

Canada

OR

Dean

College of Graduate and Postdoctoral Studies

University of Saskatchewan

116 Thorvaldson Building, 110 Science Place

Saskatoon, Saskatchewan S7N 5C9

Canada

Abstract

Organic photovoltaics (OPVs) have recently experienced a tremendous increase in efficiency due to advancements in light absorbing materials and improvements in film morphology control. Solvent vapour annealing (SVA) of OPVs is an important post deposition method for controlling film morphology; however, current OPV SVA methods are difficult to reproduce, provide limited control over morphology, and lack scalability. In this thesis, it is shown that a flow through variable-pressure solvent vapour annealing (VP-SVA) system can be used to reproducibly and selectively anneal OPV active layers to controlled morphologies. VP-SVA is useful not only for the well-studied P3HT:$PC_{61}BM$ model system, but also for modern OPV active layers based on non-fullerene acceptors. Phase separation and material crystallinity are tuned by controlling the chloroform vapour concentration used in the annealing process; this was monitored by photo-induced force microscopy (PiFM) and grazing incidence wide angle X-ray scattering (GIWAXS), respectively. The results show that over-annealing can occur in both active layer blends, illustrating the importance of tuning the solvent vapour concentration.

Acknowledgements

I would like to thank my supervisor Dr. Timothy Kelly for his guidance throughout my program. He has been an amazing mentor both in and out of the lab. I have truly enjoyed my time here and Tim's guidance helped minimize the frustration when things didn't go as planned.

I would also like to thank all the Kelly group members for their help and guidance. Specifically, I would like to thank Kyle Fransishyn for "showing me the ropes" when I arrived, Nick Randell and Kianoosh Poorkazem for teaching me how to make solar cells, and Chase Radford for thoughtful (if sometimes distracting) discussions.

I am also thankful for the support staff; specifically, Ted Toporowski in the physics machine shop for fabricating all the sample holders required to perform my experiments. Additionally, I would like to thank Chang-Yong Kim and the other beamline scientists at HXMA for their assistance. Finally, I would like to thank my collaborators Seth McAfee and Gregory Welch for providing some of the materials used to complete this thesis, and Jessica Kong for performing the PiFM.

I would also like to thank my fiancée Maria Klok for supporting me through my degree. She sacrificed a lot to follow me to Saskatchewan so I could pursue my education. I greatly appreciate her support and commitment.

Finally, I would like to thank NSERC for funding.

Table of Contents

Permission to Use ..... **i**
Abstract ..... **ii**
Acknowledgements ..... **iii**
Table of Contents ..... **iv**
List of Tables ..... **vi**
List of Figures ..... **vii**
List of Charts ..... **x**
List of Abbreviations ..... **xi**
Chapter 1: Introduction **1**
1.1. Introduction to Solar Cells 1
1.2. Organic Photovoltaics 3
1.2.1. Characteristics of Organic Photovoltaics 3
1.2.2. Bulk Heterojunction 8
1.3. Morphology Control 9
1.3.1. Kinetics and Thermodynamics of Film Casting 9
1.3.2. Morphology Control Through Synthesis 10
1.3.3. Casting Solvents 11
1.3.4. Casting Solvent Additives 11
1.3.5. Thermal Annealing 13
1.4. Solvent Vapour Annealing 14
1.5. Organic Photovoltaic Materials 19
1.5.1. P3HT:$PC_{61}BM$ 19
1.5.2. Small Bandgap Donors 21
1.5.3. Non-Fullerene Acceptors 23
1.6. X-ray Diffraction 24
1.6.1. Grazing Incidence Wide Angle X-ray Scattering 26
1.7. Force Microscopy Techniques 33
1.7.1. Atomic Force Microscopy 33
1.7.2. Photo-induced Force Microscopy 36

1.8. Objectives 38
1.9. Co-Authorship Statement 39
1.10. Manuscript Permission 39
Chapter 2: Experimental 40
2.1. Materials 40
2.2. Characterization 40
2.3. GIWAXS Parameters 41
2.4. Device Characterization 41
2.5. Variable-Pressure Solvent Vapour Annealing 41
2.6. Substrate Preparation 42
2.7. ZnO Films 42
2.8. P3HT:$PC_{61}BM$ Films 43
2.9. PTB7-Th:PDI-DPP-PDI Films 43
2.10. OPV Device Fabrication 43
Chapter 3: Results and Discussion 44
3.1. Introduction 44
3.2. P3HT:$PC_{61}BM$ 45
3.2.1. UV-Visible Spectroscopy 45
3.2.2. Photo-induced Force Microscopy 49
3.2.3. Grazing Incidence Wide Angle X-ray Scattering 55
3.2.4. Device Performance 58
3.3. PTB7-Th:PDI-DPP-PDI 61
3.3.1. UV-Visible Spectroscopy 61
3.3.2. Photo-induced Force Microscopy 66
3.3.3. Grazing Incidence Wide Angle X-ray Scattering 70
3.3.4. Device Performance 77
Chapter 4: Conclusions 80
4.1. Summary 80
4.2. Future Work 82
Chapter 5: References 85

List of Tables

Table 3.1: Device performance parameters for P3HT:$PC_{61}BM$ devices annealed at various chloroform vapour concentrations 61
Table 3.2: Device performance parameters for PTB7-Th:PDI-DPP-PDI devices annealed at various chloroform vapour concentrations 78

List of Figures

Figure 1.1: p-n junction diagram..... 2
Figure 1.2: Circuit model for OPVs..... 5
Figure 1.3: OPV architectures..... 6
Figure 1.4: Band diagram of organic semiconductors. 7
Figure 1.5: Schematic overview of the phase separation processes during OPV casting..... 10
Figure 1.6: Schematic of the bell jar annealing apparatus 14
Figure 1.7: Schematic of the variable pressure solvent vapour annealing apparatus 16
Figure 1.8: Schematic of the flow through variable pressure solvent annealing apparatus. 18
Figure 1.9: Schematic of H and J aggregation 21
Figure 1.10: Molecular orbital diagram of generic push-pull polymer..... 22
Figure 1.11: Schematic diagram of grazing-incidence scattering geometry..... 28
Figure 1.12: GIWAXS pattern wedge removal 29
Figure 1.13: Illustrations of example diffraction patterns for different material orientations 30
Figure 1.14: Illustration of the P3HT backbone stacking orientation relative to a substrate..... 31
Figure 1.15: 2-D GIWAXS image of as-cast P3HT thin film 32
Figure 1.16: 2-D GIWAXS images of as-cast thin films of neat P3HT 32
Figure 1.17: AFM imaging of pentacene on Cu(111)..... 34
Figure 1.18: Phase shift in AFM frequency detected for phase imaging..... 35
Figure 1.19: Simplified schematic of the PiFM setup 37
Figure 1.20: Donor phase PiFM of PII-2T-PS/PPDI-T BHJ films..... 38
Figure 3.1: In situ UV/Vis spectroscopy of P3HT:$PC_{61}BM$ thin films annealed with various chloroform vapour concentrations 47
Figure 3.2: Post annealing UV/Vis spectra and absorbance at 600 nm as a function of time for P3HT:$PC_{61}BM$ thin films annealed at various chloroform concentrations. 48
Figure 3.3: PiFM images of P3HT:$PC_{61}BM$ thin films annealed at various chloroform vapour concentrations. 51
Figure 3.4: PiFM and ATR-FTIR spectra of films of pure P3HT and $PC_{61}BM$. 52
Figure 3.5: FFT of the PiFM signal of P3HT:$PC_{61}BM$ thin films annealed at various chloroform concentrations. 54

Figure 3.6: AFM topographic images of P3HT:$PC_{61}BM$ thin films annealed at various chloroform concentrations 55
Figure 3.7: GIWAXS patterns of P3HT:$PC_{61}BM$ thin films annealed at various chloroform vapour concentrations. 56
Figure 3.8: GIWAXS linecuts of P3HT:$PC_{61}BM$ thin films 57
Figure 3.9: Power conversion efficiency of P3HT:$PC_{61}BM$ devices annealed at various chloroform concentrations 60
Figure 3.10: UV/Vis spectra of neat PDI-DPP-PDI thin films annealed at various chloroform concentrations. 62
Figure 3.11: UV/Vis spectra of neat PTB7-Th thin films annealed at various chloroform concentrations 63
Figure 3.12: Post-annealing UV/Vis spectra and absorbance at 584 nm as a function of time for PTB7-Th:PDI-DPP-PDI thin films annealed at various chloroform vapour concentrations..... 64
Figure 3.13: In situ UV/Vis spectroscopy of PTB7-Th:PDI-DPP-PDI thin films annealed with various chloroform vapour concentrations 65
Figure 3.14: PiFM images of PTB7-Th:PDI-DPP-PDI thin films annealed at various chloroform vapour concentrations 67
Figure 3.15: PiFM and ATR-FTIR spectra of films of pure PTB7-Th and PDI-DPP-PDI 68
Figure 3.16: FFT of the PiFM signal for PTB7-Th:PDI-DPP-PDI thin films annealed at various chloroform concentrations. 69
Figure 3.17: AFM topographic images of PTB7-Th:PDI-DPP-PDI thin films annealed at various chloroform concentrations. 70
Figure 3.18: GIWAXS patterns of neat PTB7-Th thin films annealed at various chloroform vapour concentrations 72
Figure 3.19: GIWAXS patterns of neat PDI-DPP-PDI thin films annealed at various chloroform concentrations 72
Figure 3.20: GIWAXS linecuts of neat PDI-DPP-PDI thin films 73
Figure 3.21: GIWAXS patterns of PTB7-Th:PDI-DPP-PDI thin films annealed at various chloroform vapour concentrations 75
Figure 3.22: GIWAXS linecuts of PTB7-Th:PDI-DPP-PDI thin films..... 76

Figure 3.23: Power conversion efficiency of PTB7-Th:PDI-DPP-PDI devices annealed at various chloroform concentrations 78

List of Charts

Chart 1.1: Chemical structures of common OPV materials 19

Chart 3.1: Structures of organic photovoltaic active layer materials used in this thesis 45

List of Abbreviations

1-CN	1-Chloronaphthalene
2D	Two Dimensional
AFM	Atomic Force Microscopy
ATR-FTIR	Attenuated Total Reflection Fourier Transform Infrared
BCP	Block Copolymer
BDT	Benzodithiophene
BHJ	Bulk Heterojunction
CB	Conduction Band
CLS	Canadian Light Source
DIO	1,8-Diiodooctane
DPE	Diphenyl Ether
DPP	Diketopyrrolopyrrole
$DPP(TBFu)_2$	3,6-Bis(5-(benzofuran-2-yl)thiophen-2-yl)-2,5-bis(2-ethylhexyl)pyrrolo[3,4-c]pyrrole-1,4(2H ,5H)-dione
EPBT	Energy Payback Time
ETL	Electron Transport Layer
FF	Fill Factor
FFT	Fast Fourier Transform
FWHM	Full-Width-at-Half-Maximum
GIWAXS	Grazing Incidence Wide Angle X-ray Scattering
HOMO	Highest Occupied Molecular Orbital
HTL	Hole Transport Layer
HXMA	Hard X-ray MicroAnalysis
IT4F	3,9-bis(2-methylene-((3-(1,1-dicyanomethylene)-6,7-difluoro)-indanone))-5,5,11,11-tetrakis(4-hexylphenyl)-dithieno[2,3-d:2',3'-d']-s-indaceno[1,2-b:5,6-b']dithiophene

ITIC	3,9-bis(2-methylene-(3-(1,1-dicyanomethylene)-indanone))-5,5,11,11-tetrakis(4-hexylphenyl)-dithieno[2,3-d:2',3'-d']-s-indaceno[1,2-b:5,6-b']dithiophene
ITO	Indium Tin Oxide
J_{max}	Current Density at the Maximum Power Point
J_{SC}	Short Circuit Current Density
L-L	Liquid-Liquid
L-S	Liquid-Solid
LUMO	Lowest Unoccupied Molecular Orbital
NFA	Non-fullerene Acceptor
ODT	1,8-Octanedithiol
OPV	Organic Photovoltaic
P3HT	Poly(3-hexylthiophene)
$PC_{61}BM$	Phenyl-C_{61}-Butyric Acid Methyl Ester
PCE	Power Conversion Efficiency
PDI	Perylene Diimide
PEDOT:PSS	Poly(3,4-ethylenedioxythiophene): Polystyrene Sulfonate
PiFM	Photo-induced Force Microscopy
P_{in}	Power In
PII-2T-PS	Poly(isoindigo-bithiophene) with 10 mol % polystyrene side chains
P_{out}	Power Out
PPDI-T	Poly(5-(thiophen-2-yl)-2,9-di(tridecan-7-yl)anthra[2,1,9-def:6,5,10-d'e'f']diisoquinoline-1,3,8,10(2H,9H)-tetraone)
PTB7	Poly[[4,8-bis[(2-ethylhexyl)oxy]benzo[1,2-b:4,5-b']dithiophene-2,6-diyl][3-fluoro-2-[(2-ethylhexyl)carbonyl]thieno[3,4-b]thiophenediyl]]

PTB7-Th	Poly{4,8-bis[5-(2-ethylhexyl)thiophen-2-yl]benzo[1,2-b:4,5-b ']dithiophene-2,6-diyl-alt-3-fluoro-2-[(2-ethylhexyl)carbonyl]thieno[3,4-b]thiophene-4,6-diyl}
PXRD	Powder X-ray Diffraction
RMS	Root Mean Squared
R_S	Series Resistance
R_{Sh}	Shunt Resistance
S-S	Solid-Solid
SCCM	Standard Cubic Centimeters per Minute
SdiPBI-Se	Se-bay-annulated 2,2',9,9'-tetra(undecan-6-yl)-[5,5'-bianthra[2,1,9-def:6,5,10-d'e'f']diisoquinolin]-1,1',3,3',8,8',10,10'(2H,2'H,9H,9'H)-octaone
SVA	Solvent Vapour Annealing
TEM	Transmission Electron Microscopy
T_g	Glass Transition Temperature
TT	Thieno[3,4-b]thiophene
UV/Vis	Ultraviolet-Visible Light
VB	Valence Band
V_{max}	Voltage at the Maximum Power Point
V_{OC}	Open Circuit Voltage
VP-SVA	Variable Pressure Solvent Vapour Annealing
XRD	X-ray Diffraction

Chapter 1: Introduction

1.1. Introduction to Solar Cells

With increasing concern about global climate change, many scientists and citizens alike are turning their attention towards the research and implementation of green energy sources. The government of Canada is attempting to phase out coal-fired electricity production by the year 2030, leaving a large gap in energy production to be filled by green energy. The prairies are the largest producers of coal-fired electricity in Canada, but long sunny days make them a prime location for solar energy production.

Currently, solar energy production is mainly performed by silicon solar cells. Silicon solar cells have high efficiencies, and a stable, non-toxic, and abundant absorber making them the most favourable material for solar farms to date.[1] One figure of merit for solar cells is their energy payback time (EPBT), which is the time required for a solar cell to produce as much energy as was required to fabricate, install, and dispose of it.[2] For silicon solar cells, EPBTs are high due to the energy intensive processing techniques required to purify semiconductor grade silicon.[3] The most common method of producing semiconductor grade silicon first requires the production of metallurgical grade silicon using a high temperature (≈ 2000 °C) reduction of quartz.[3] Following this, the silicon must be chlorinated, distilled, and then deposited by chemical vapour deposition.[3] Chemical vapour deposition of silicon requires a large amount of energy and forms chlorinated silicon waste byproducts.[3] The silicon must then be crystallized and doped, cut into wafers, and processed into solar cells, all of which require more energy.[3]

Silicon solar cells operate via a p-n junction. A p-type (positive) semiconductor primarily transports holes (a hole is the lack of an electron) and an n-type (negative) semiconductor primarily transports electrons.[4] For silicon to act like a p-type or n-type semiconductor it requires a dopant, commonly boron and phosphorus, respectively.[4] In a p-n junction, electrons diffuse from the n-type semiconductor towards the p-type semiconductor. At the p-n boundary, a positive charge builds up in the n-type semiconductor as electrons diffuse away, and a negative charge builds on the p-type semiconductor as electrons diffuse in **(Figure 1.1)**.[5] As the potential difference between the p and n type materials rises, the electrostatic repulsion force and the diffusion force reach an equilibrium and a depletion zone is formed where no free charge carriers are present.[5] Another way to visualize the p-n junction is through band diagrams. The p and n type dopants in silicon change the Fermi level (E_f).[5] The fermi level is defined as the theoretical energy level with a 50% chance of being occupied. When you place two materials together, their Fermi levels equilibrate; for doped silicon this results in the band structure seen in **Figure 1.1**.[5]

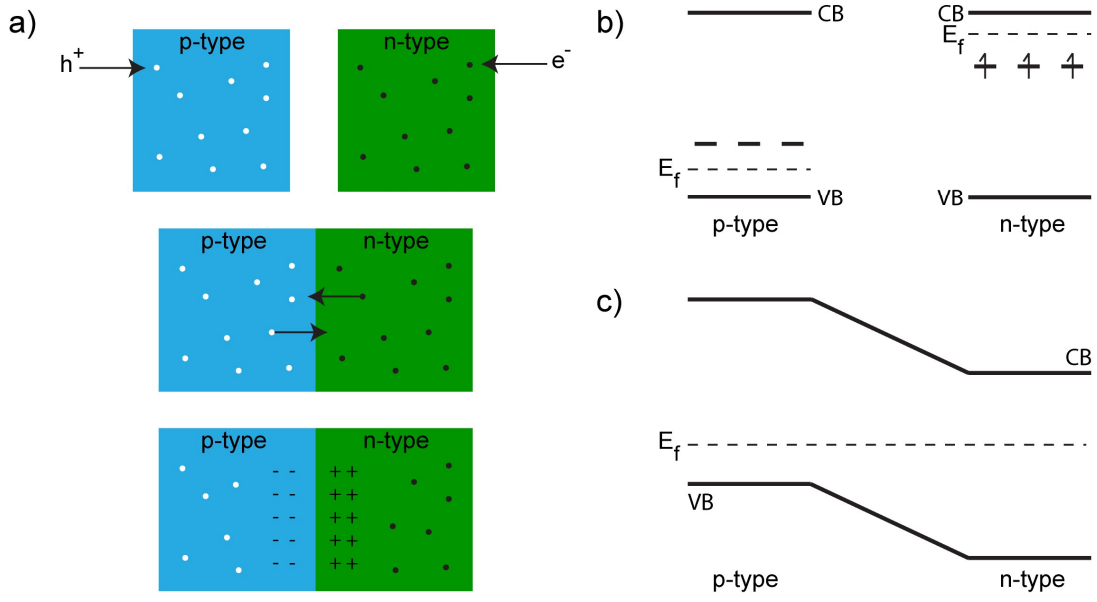

Figure 1.1: (a) p-n junction diagram. (b) Doped silicon band diagram. (c) Silicon p-n junction band diagram. Conduction band (CB) and valence band (VB) are noted.

When a semiconductor absorbs light, an exciton (an excited electron-hole pair) is formed.[5] In silicon, a Wannier-Mott type exciton is formed which has a binding energy low enough to be overcome by thermal energy.[5] Once the exciton is split, the electron flows towards the n-type region through the conduction band and the hole flows towards the p-type region through the valence band; this is due to the built-in potential caused by the depletion zone.[5] The electron can then be collected and used to perform work.

While silicon solar cells are efficient, the modules are brittle and heavy, and their processing is energy intensive, limiting their applications.[3] Other types of solar cells, such as cadmium telluride[6] and perovskite solar cells,[7] have remarkable efficiencies as well; however, toxicity and stability issues have reduced their market share. Dye sensitized,[8] and kesterite[9] solar cells are less toxic alterative solar cell materials; however, poor performance has limited the widespread use of these technologies. Organic solar cells (also known as organic photovoltaics (OPVs)) are less toxic, have tunable electronic properties, come in a variety of colours, are flexible, and allow for solution processing;[2] they will be the focus of this thesis.

1.2. Organic Photovoltaics

1.2.1. Characteristics of Organic Photovoltaics

Research into organic photovoltaics has gained momentum in recent years with efficiencies reaching beyond 14%.[10,11] With natural flexibility, light weight, and tunable colours, OPVs find applications in flexible electronics and solar windows.[12–14] Due to the solution processability of organic molecules, high throughput fabrication methods such as roll-to-roll processing can be used to reduce production costs and energy consumption, lowering the EPBT.[2,15] As a result, OPVs are in the initial stages of commercialization.[2,13,16]

To compare OPVs between labs, different figures of merit and standard testing practices have been generally agreed upon by the solar cell community. Short circuit current density (J_{SC}) is the current produced at short circuit (no applied voltage) divided by the area of the device **(Figure 1.2)**.[2] The open circuit voltage (V_{OC}) is the voltage produced by the device when there is zero current flow.[2] The fill factor (FF) is a measure of the squareness of the J-V curve and can be calculated using **Equation 1.1**,[2] where J_{max} and V_{max} are the current density and voltage at the maximum power point, respectively. FF is affected by the series (R_S) and shunt (R_{Sh}) resistances of the devices.[2] R_S is the resistance along the circuit;[2] low R_S is desired **(Figure 1.2)**.[2] R_S is a result of the inherent resistance in connecting wires, at layer interfaces, and through the material.[2] R_S can be minimized by using materials with high charge carrier mobilities and good interface compatibility. The R_{Sh} is the resistance to parasitic current flow;[2] a high R_{Sh} is favored.[2] R_{Sh} can be maximized by increasing active layer thickness, and removing pinholes. Power conversion efficiency (PCE) is the power output (P_{out}) of the device divided by the input power (P_{in}) **(Equation 1.2)**.[2] To ensure reproducibility from lab to lab, AM 1.5G standard conditions are used to determine PCE.[17] AM 1.5G represents the solar spectrum at 1.5 air masses, and is typically used at an intensity of 100 mW/cm^2 for determining the PCE of OPVs.[17,18]

$$FF = \frac{V_{max} \times J_{max}}{V_{OC} \times J_{SC}} \times 100\% \tag{1.1}$$

$$PCE = \frac{P_{out}}{P_{in}} \times 100\% = \frac{V_{OC} \times J_{SC} \times FF}{P_{in}} \times 100\% \tag{1.2}$$

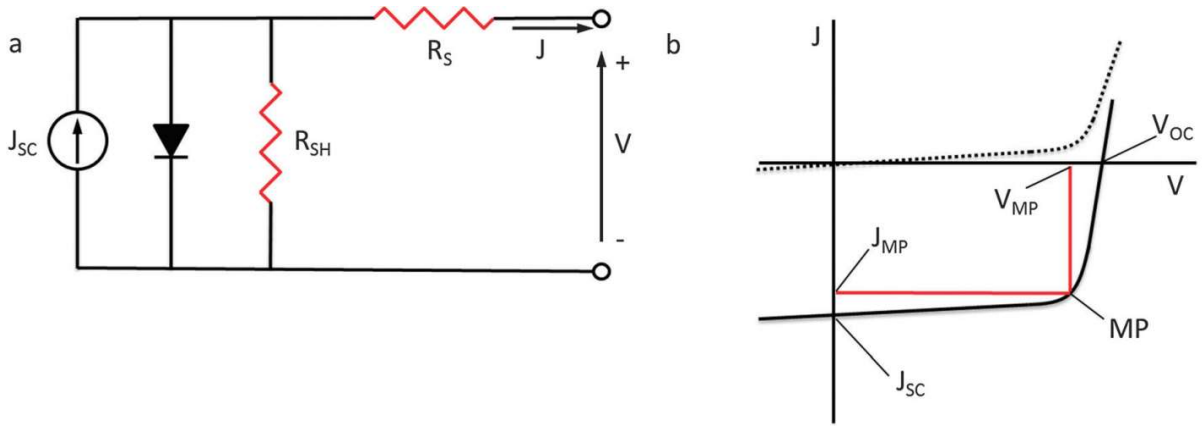

Figure 1.2: (a) Equivalent circuit model for OPV and (b) current density–voltage (J–V) curves of an organic solar cell, (dotted) dark, (solid) illuminated. Reproduced from Mazzio, K. A.; Luscombe, C. K. *Chem. Soc. Rev.* **2015**, *44*, 78 with permission of The Royal Society of Chemistry.[2]

When fabricating an OPV, a substrate is coated in a transparent conductive layer, usually ITO (indium tin oxide), which functions as an electrode **(Figure 1.3)**.[2] In a standard architecture device, a hole transport (or electron blocking) layer (HTL) is coated onto the ITO to facilitate charge transport.[2] Next the active layer (light absorbing layer) is applied;[2] the most common active layer deposition technique in laboratories is spin coating. On top of this an electron transport layer (ETL), and a top electrode (usually a low work function metal) are applied by thermal evaporation under high vacuum.[2] The low work function top electrode (usually aluminium) can be readily oxidized in air, reducing the stability and lifetime of the devices.[2] To combat this, the inverted architecture was developed with a robust high work function electrode (Ag or Au).[2] In inverted devices, the ETL is applied over the ITO layer, followed by the active layer; then the HTL and top electrode are deposited using thermal evaporation under high vacuum.[2] The primary ETLs used are LiF and Ca for regular architecture devices and ZnO for inverted devices.[2] Common HTLs include PEDOT:PSS (poly(3,4-ethylenedioxythiophene) mixed with polystyrene sulfonate) for regular architecture, and MoO_{3-x}, and V_2O_{5-x} for inverted architecture devices.[2]

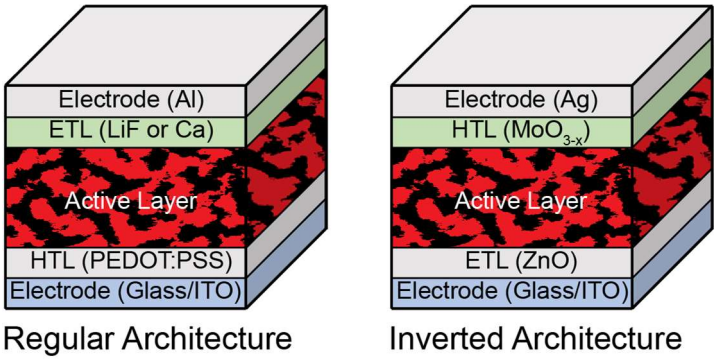

Figure 1.3: Regular and Inverted OPV architectures. Common materials are emphasized.

When light is absorbed by an OPV active layer an exciton is formed.[2] In contrast to inorganic solar cell materials, organic molecules tend to have a lower relative permittivity ($\varepsilon \approx 3.5$ for poly(3-hexylthiophene) (P3HT),[19] and $\varepsilon \approx 12$ for silicon)[20] which leads to tightly bound excitons called Frenkel excitons.[21] Frenkel excitons are excitons with a binding energy too large to be overcome by thermal energy (approximately 0.1 – 0.4 eV in organic semiconductors).[21] Therefore, to separate excitons into useable electrons and holes, a heterojunction consisting of an electron donor (p-type) and acceptor (n-type) must be present.[21] In an OPV heterojunction, the acceptor has a lower energy HOMO and LUMO (highest occupied molecular orbital, and lowest unoccupied molecular orbital, respectively) than the donor to facilitate electron transfer from donor to acceptor **(Figure 1.4)**.[21] Once an exciton is formed in an OPV it travels to the boundary of the donor and acceptor materials through either a Förster resonance energy transfer or a Dexter transfer mechanism.[21] Once at the donor-acceptor boundary the electron is transferred to the acceptor (or the hole is transferred to the donor) creating a geminate electron-hole pair which is bound together by coulombic attraction.[21] The built-in driving force created by the difference in energy levels of the donor LUMO and acceptor LUMO separates the geminate pair into free charge carriers.[21] The free charge carriers must then travel to their respective transport layers and be collected by the electrodes.[21]

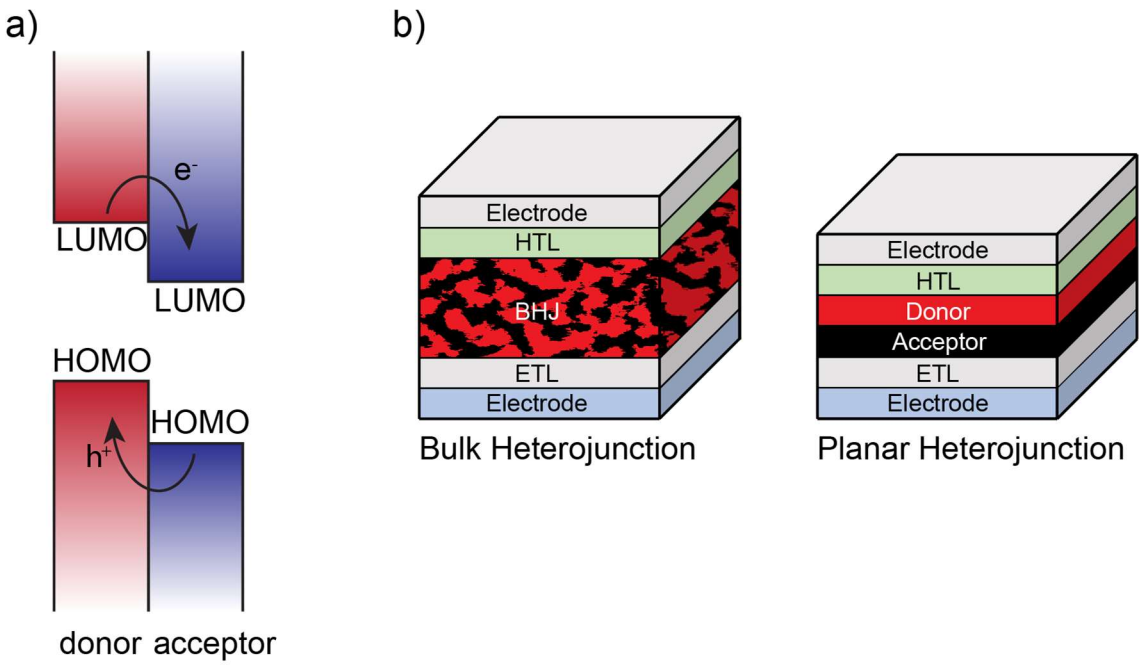

Figure 1.4: (a) Band diagram of organic semiconductors. (b) OPV architectures.

The planar heterojunction was introduced by Tang in 1985 as the first example of a donor acceptor heterojunction **(Figure 1.4)**.[22] The planar heterojunction benefits from simplicity and can effectively split excitons at the donor acceptor interface; however, the average distance an exciton can travel before recombination is 20 nm.[21] If the exciton cannot reach a domain boundary within its lifetime it geminately recombines, emitting heat or light.[21] Therefore, the optimal thickness for each layer in a planar heterojunction is less than 40 nm; however, due to the poor light absorption of organic molecules, 40 nm of material is not sufficient to absorb all the light passing through the solar cell.[21] To absorb all available light, OPVs need a thicker active layer while keeping the donor-acceptor interfaces within the size range of 40 nm. The bulk heterojunction (BHJ), which is an intimate mixture of donor and acceptor materials, was invented by the Heeger group to increase layer thickness while keeping donor-acceptor interfaces close.[23]

1.2.2. Bulk Heterojunction

The most common active layer architecture in OPVs is a BHJ **(Figure 1.4)**.[21] To fabricate a BHJ, donor and acceptor materials are dissolved in the same solution and cast onto a substrate (which is usually pre-coated with a HTL or ETL). The solution can be cast in many ways; in a laboratory setting, active layers are primarily cast by spin coating. Unfortunately, spin coating wastes most of the solution as the materials are flung from the substrate during spinning. Additionally, spin coating is not scalable as the logistics of spinning large substrates becomes increasingly problematic. Other more scalable and less wasteful casting techniques include: blade coating,[24] slot die coating,[25] and inkjet printing.[26] As the films dry, the materials phase separate and (often) form discrete domains of donor and acceptor materials as well as some intermixed domains.[27] Each casting technique has different film formation kinetics and results in different BHJ morphologies.

Controlling the blend morphology of the BHJ is of the utmost importance to device performance. As mentioned previously, to effectively split excitons the optimal blend morphology will have domain sizes smaller than 40 nm in at least one direction.[21] If the domains of the material that absorbed light are too large, recombination of the electron-hole pair occurs before the exciton can find a donor-acceptor interface (geminate recombination) and the energy contained within it is reemitted as a photon or lost as heat.[21] Conversely, the domain sizes need to be large enough in at least one dimension to allow efficient charge transport to the hole and electron transport layers and ultimately the electrodes.[21] If a free hole and free electron meet in the BHJ (perhaps due to being trapped in small domains) they can recombine (non-geminate recombination).[21] Additionally, the active layer films must be thick enough that sufficient light is absorbed, but not

so thick as to hinder charge transport to the electrodes.[21] Thus, much work has been performed to optimise OPV materials and BHJ blend morphology.

1.3. Morphology Control

1.3.1. Kinetics and Thermodynamics of Film Casting

When casting BHJ active layer solutions there is typically a mixture of three materials: the casting solvent, the donor, and the acceptor. The interactions of the materials in solution can be thermodynamically modeled using the Flory-Huggins equation **(Equation 1.3)**.[27,28] Where ΔG_m is the Gibbs free energy of mixing, R is the ideal gas constant, T is absolute temperature, φ_i is the volume fraction of the component, N_i is a parameter related to the molecular size of the materials, and χ is the Flory-Huggins parameter which describes the compatibility of two materials.[27] The Flory-Huggins parameters determine how well the donor and acceptor materials mix with the solvent, and how they mix with each other as the films dry.[27] If the physical compatibility of the materials is too high, a well blended homogenous phase is formed, which leads to high rates of non-geminate recombination; however, if the compatibilities are too low, large domains of pure materials form, hindering the formation of free charge carriers.[27]

$$\frac{\Delta G_m}{RT} = [\varphi_S\, ln(\varphi_S) + \left(\frac{\varphi_D}{N_D}\right) ln(\varphi_D) + \left(\frac{\varphi_A}{N_A}\right) ln(\varphi_A) + \chi_{SD}\varphi_S\varphi_D + \chi_{SA}\varphi_S\varphi_A + \chi_{DA}\varphi_D\varphi_A] \quad (1.3)$$

The interactions of the materials during film drying can occur by liquid-liquid (L-L) interactions, liquid-solid (L-S) interactions, or neither **(Figure 1.5)**.[27,29,30] For most systems, the solution begins as a single phase when the donor and acceptor concentrations are low.[27] As the solvent begins to evaporate, L-L separation can be induced by repulsions between the donor and acceptor if they have poor compatibility factors (χ).[27] The L-L separation leads a to high degree of phase separation and large domains, often leading to poor device performance.[27] L-S interactions

occur as the donor or acceptor material reaches its saturation concentration and begins to aggregate and precipitate.[27] The kinetics of aggregation and solvent evaporation play a key role in the degree of phase separation caused by L-S separation.[27] Additionally, as one material aggregates and precipitates, it decreases the relative concentration of that material in solution reducing (or even eliminating) the effect of L-L separation.[27] The L-L and L-S processes may occur simultaneously or sequentially, and a homogenous blend of donor and acceptor forms if neither process occurs.[27] Solid-solid (SS) interactions can also be induced in the film once it has dried through techniques such as annealing.[29]

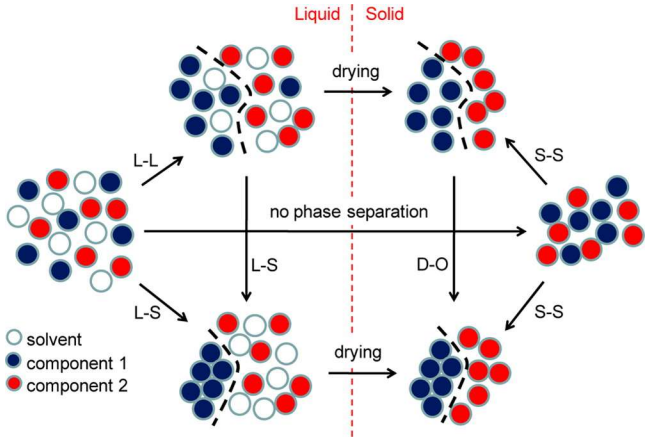

Figure 1.5: Schematic overview of the phase separation processes that may occur during drying of a solution that contains two components. L−L, L−S, and S−S are liquid−liquid, liquid−solid, and solid−solid phase separations, respectively, and D−O is disorder−order transition. Reprinted with permission from Kouijzer, S; Michels, J. J.; van den Berg, M.; Gevaerts, V. S.; Turbiez, M.; Wienk, M. M.; Janssen, R. A., J. *J. Am. Chem. Soc.* **2013**, *135*, 12057. Copyright 2013 American Chemical Society.[29]

1.3.2. Morphology Control Through Synthesis

Many synthetic strategies have been developed to control the morphology of BHJ active layers. The first methods of morphology control involved side chain engineering,[31] polymer regioregularity,[32] and molecular weight.[33] Side chains were initially used to improve the solubility of conjugated molecules;[34] however, they have been shown to drastically affect the self assembly,

packing, and crystallite orientation of polymer chains.[35–37] Long alkyl chains can disrupt the π stacking of adjacent molecules, decreasing charge transport in the bulk materials;[38] however, alkyl chain interdigitation can improve donor-acceptor mixing and crystallinity, which minimizes recombination losses.[39]

1.3.3. Casting Solvents

The simplest morphology control parameters are solvent selection and solvent additives.[40] The solubility of the donor and acceptor materials, and the drying rate (solvent vapour pressure and boiling point) are the primary factors that go into casting solvent choice.[27,41] P3HT cast from chloroform (a low boiling point solvent) results in a kinetically trapped amorphous film[42] with the aromatic backbone primarily oriented parallel with the substrate;[43] in contrast, P3HT films cast from chlorobenzene (a higher boiling point solvent) have a longer drying time, resulting in a higher degree of aggregation[42] and the aromatic backbone stacking primarily perpendicular to the substrate.[43] P3HT is highly soluble in both chloroform and chlorobenzene (14.1 and 15.9 mg/mL, respectively);[44] therefore the changes in morphology are primarily attributed to solvent drying rates. Ensuring the solvent choice is cheap, green, and capable of being recovered and reused or disposed of safely is also a growing concern as OPVs are beginning to be produced on industrial scales.[37,45–49]

1.3.4. Casting Solvent Additives

Casting solvent additives were invented accidentally by Peet et. al. in 2006, when they added a surfactant to the casting solvent.[27,50] The surfactant was intended to incorporate gold nanoparticles into a P3HT:$PC_{61}BM$ (Phenyl-C_{61}-butyric acid methyl ester) OPV; however, they found that excess surfactant improved the morphology of the devices.[50] Immediately following this discovery Peet et. al. were able to show that different alkanethiol solvent additives were able

to improve the efficiency of a BHJ blend that was unresponsive to annealing.[27,51] It was initially believed that the best solvent additives would increase the drying time of the active layer to induce crystallization, and selectively solvate one BHJ component; therefore most solvent additives have been designed around this concept.[27] More recently, with the development of L-L, L-S, and Flory-Huggins models **(Equation 1.3)**, the role of solvent additives on BHJ morphology is better understood.[27]

The most popular solvent additives are 1,8-diiodooctane (DIO), 1,8-octanedithiol (ODT), 1-chloronaphthalene (1-CN), and diphenyl ether (DPE).[27] DIO has a high boiling point and low vapour pressure. When DIO is added to a BHJ casting solution the active layer remains slightly solvated after casting, which does not overly affect the total film thickness, but allows more time for materials to assemble to an L-S controlled product.[52] Additionally, DIO dissolves fullerenes preferentially over polymers, decreasing the L-L phase separation and increasing the L-S de-mixing time afforded to the polymeric donor.[27] Unfortunately, DIO has been shown to degrade films over time if not fully removed after casting.[52–54] Other solvent additives perform a similar function to DIO, albeit with different material selectivities, drying times, and nucleation mechanisms resulting in different final morphologies.[27] DIO tends to increase domain sizes and is therefore used in more amorphous systems[27,55,56] while 1-CN has been used to decrease domain sizes, which can be beneficial in systems prone to over-crystallization.[27,57–59] Solvent selection and solvent additives often do not achieve the most thermodynamically stable state, so once the solution has fully solidified, post-processing treatments may be used if further S-S interactions are required to optimise BHJ morphology.[56]

1.3.5. Thermal Annealing

P3HT:$PC_{61}BM$ cast from a fast drying solvent is an example of a system that undergoes little L-L or L-S phase separation while casting.[29,60] For these systems, annealing techniques are required to induce S-S phase separation to achieve optimum morphology.[29] When a BHJ blend is heated above the glass transition temperature (T_g) of one or more of the materials, the materials can begin to rearrange to a more thermodynamically stable state.[61] The enthalpy of crystallization is often higher than the entropy of mixing in many of the conjugated materials used for OPVs; as a result, thermal annealing of BHJ blends can lead to phase separated crystal domains.[43,62] In 2003 Padinger et. al. showed that thermal annealing of P3HT:$PC_{61}BM$ increased device efficiency from 0.4% to 3.5%.[63] When cast, the mixed phase of P3HT:$PC_{61}BM$ materials is trapped by the kinetics of the casting procedure.[64] Once the BHJ blend is heated above the T_g of P3HT, the P3HT chains increase their mobility in the solid state and the $PC_{61}BM$ migrates out of the P3HT in favour of forming pure domains of P3HT and $PC_{61}BM$.[64] The improved crystallinity and reduction of mixed phases increases charge transport and decreases non-geminate recombination in the P3HT:$PC_{61}BM$ BHJ.[64]

Not all OPV systems increase in efficiency with thermal annealing.[27,65–67] Many modern amorphous polymer donors do not require annealing to achieve the optimal morphology, and over annealing polymer:fullerene blends can lead to a large degree of PCBM aggregation.[65–68] This leads to the formation of large domains causing high geminate recombination rates.[65] Thermal annealing also has a few disadvantages: it has a large energy cost associated with heating, and the potential to degrade materials.

1.4. Solvent Vapour Annealing

Solvent vapour annealing (SVA) is another common post-deposition method of morphology control. SVA uses solvent vapour to partially solvate a BHJ film, lowering the T_g of the materials to below ambient temperature; this allows the BHJ materials to rearrange to a more thermodynamically stable state.[69]

The initial report of the solvent annealing effect is attributed to the Yang group.[70] They decreased the drying rate of P3HT:$PC_{61}BM$ films (cast with a slow drying solvent (1,2-dichlorobenzene)) by covering them in a petri dish after spin coating the active layer.[70] They also dried films in ambient or slightly elevated temperatures (50 and 70 °C) to reduce the drying times.[70] The devices that were dried slowly showed an increase in efficiency from 1.36% to 3.52% (for the fastest and slowest drying times, respectively).[70]

Following Yang's discovery, the methods of SVA were improved. The current standard SVA method is the bell jar method.[71] The bell jar SVA method involves placing a BHJ film in a sealed jar with solvent **(Figure 1.6)**.[71] The solvent vapour fills the headspace of the jar and swells the BHJ film, lowering the T_g as described earlier.[71] The film is then removed from the jar and the solvent vapour dissipates immediately, solidifying the film and trapping the new morphology.[71]

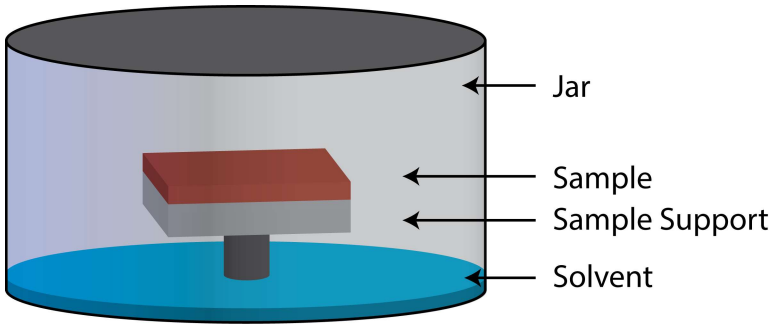

Figure 1.6: Bell jar annealing apparatus.

SVA has been used extensively to anneal P3HT:$PC_{61}BM$ devices.[72–77] The solubility of P3HT and $PC_{61}BM$ in the annealing solvent can be controlled through solvent selection.[72,75,77] Control of solubility has a large effect on the morphology of the films, and consequently the device performance. It was shown by Park et. al. that acetone (a non-solvent for both P3HT and $PC_{61}BM$) increased the device efficiency from 0.94% (as-cast) to 3.29%, while chloroform (a good solvent for both P3HT and $PC_{61}BM$) only increased the efficiency to 2.66%.[72] They showed through atomic force microscopy (AFM) that annealing with chloroform produced larger domains of P3HT and $PC_{61}BM$, and that there was a loss of P3HT face-on orientation by grazing incidence X-ray diffraction when compared to annealing with acetone.[72] Additionally, they showed that when P3HT:$PC_{61}BM$ films were annealed with chloroform, the hole mobility (μ_h) of the films was higher than films annealed with acetone.[72] This showed that larger domains of P3HT and $PC_{61}BM$ increase charge transport but hinder free charge carrier generation (as shown by a decrease in device performance even though charge carrier mobility increases).[72]

Hu et al. showed that devices annealed with 2-chlorophenol (a good solvent for $PC_{61}BM$ and a non-solvent for P3HT) performed better than devices annealed with toluene (a poor solvent for both P3HT and $PC_{61}BM$) or chlorobenzene (a good solvent for both P3HT and $PC_{61}BM$).[75] They claimed that annealing P3HT with a good solvent for short periods of time increases P3HT crystallinity; however, extended periods of annealing decreases P3HT crystallinity by re-dissolving P3HT crystallites.[75] They also showed that $PC_{61}BM$ crystallite size continues to grow as the annealing time is increased, indicating that the precise ratio of P3HT and $PC_{61}BM$ crystallite sizes can be tuned by selecting appropriate solvents.[75]

The bell jar method has also been used to increase the device performance of modern systems.[78–80] Sun et al. solvent vapour annealed a diketopyrrolopyrrole (DPP) based small

molecule BHJ system, DPP(TBFu)$_2$:PC$_{71}$BM **(Chart 1.1)**.[79] The PCE of the devices increased from 0.55% (as cast) to 5.16% when annealed using carbon disulfide vapour.[79] Annealing with carbon disulfide produced fine fiber-like crystallites of DPP(TBFu)$_2$ and fine domains of PC$_{71}$BM increasing charge transport and photocurrent, respectively.[79] Zheng et al. could increase the efficiency of PTB7:PC$_{71}$BM **(Chart 1.1)** devices from 6.55% to 8.13% using SVA in methanol.[81]

In the bell jar technique, the solvent vapour pressure depends on the surface area of the solvent, the headspace of the jar, the volatility of the solvent, and the time the system is allowed to equilibrate. Due to the various sizes of jars, with different headspace and solvent capacities, the lab to lab variation in bell jar annealing is high.[71] Variable-pressure solvent vapour annealing (VP-SVA) was introduced as an improvement to the bell jar technique.[75,77,82–86] In the VP-SVA method, solvent is added to a tube that is closed on the bottom and open to atmosphere on the top **(Figure 1.7)**.[75] The solvent vapour diffuses up the tube and creates an equilibrium gradient with the atmosphere.[75] The vapour pressure of the annealing solvent applied to the BHJ film can be controlled by varying the height of the sample in the tube.[75]

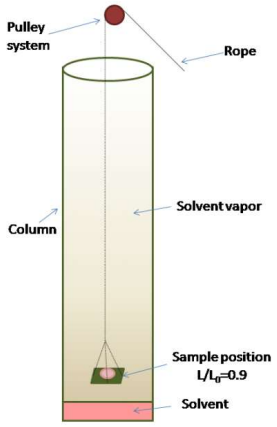

Figure 1.7: Schematic of the solvent vapor annealing apparatus: Variation in solvent vapor pressure during annealing is achieved by changing the position of wafer surface with respect to the solvent surface. Reproduced from Hu, S.; Dyck, O.; Chen, H.; Hsiao, Y.; Hu, B.; Duscher, G.; Dadmun, M.; Khomami, B. *RSC Adv*. **2014**, *4*, 27931 with permission of The Royal Society of Chemistry.[75]

Tang et al. showed that multi solvent VP-SVA can be used to fine tune the morphology of P3HT:$PC_{61}BM$ devices.[77] Using saturated THF for the first solvent annealing step Tang found large $PC_{61}BM$ crystallites formed by transmission electron microscopy (TEM) and AFM.[77] During the second annealing step in CS_2 (at 80% of the saturation vapour pressure) the crystallinity of the P3HT increased and the $PC_{61}BM$ crystallites reduced in size, presumably due to partial solvation of the $PC_{61}BM$.[77] By fine tuning the morphology, Tang et al. increased the efficiency of P3HT:$PC_{61}BM$ devices from 1.6% (as cast) to 3.9%, an efficiency higher than they achieved with thermal annealing (3.2%).[77]

The tube method of VP-SVA allows for selective annealing of BHJ films; however, it requires several hours to equilibrate the vapour concentration gradient and is inherently a small batch process.[75] Researchers in the field of block copolymers (BCPs) have developed an elegant solution, termed here flow through VP-SVA.[71,87–98] In the flow through VP-SVA system a stream of dry carrier gas is split and sent into two (or more) flow controllers **(Figure 1.8)**. One stream of carrier gas remains dry and the other stream(s) flow through solvent bubblers, becoming saturated in solvent vapour (p_{sat}). The streams then mix and flow over the sample. The vapour pressure of the solvent in the chamber (p) is varied by changing the ratio of dry carrier gas and solvent saturated carrier gas.

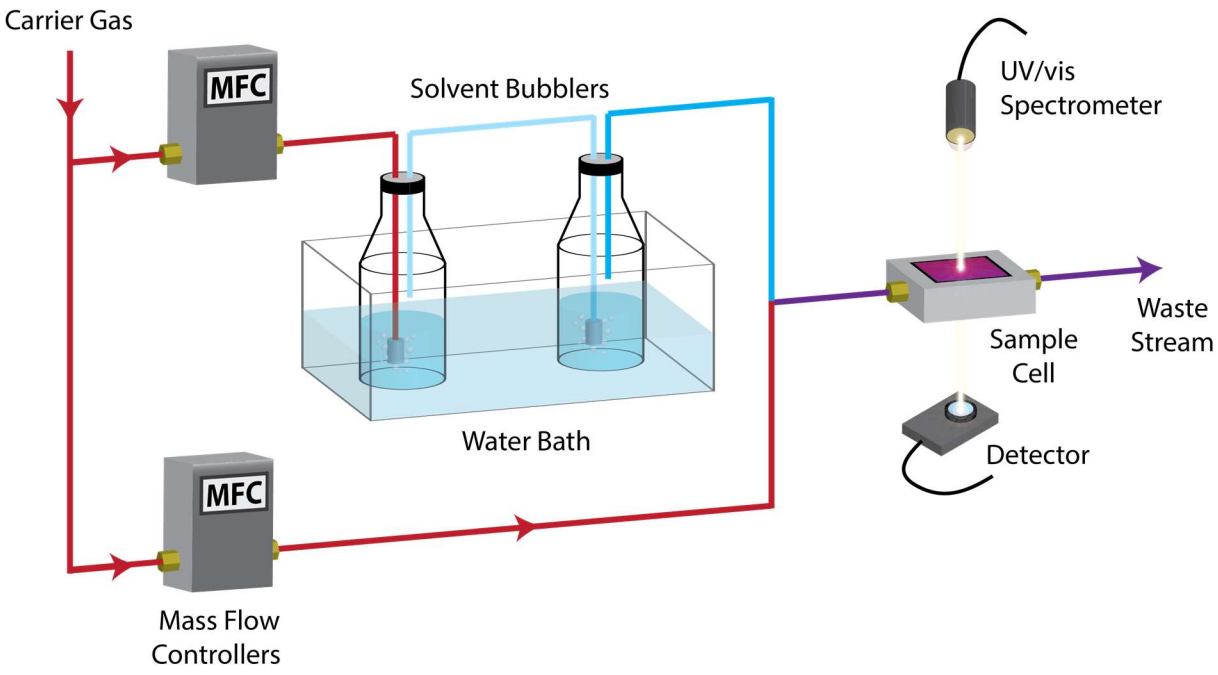

Figure 1.8: Flow through VP-SVA apparatus. Reprinted with permission from Zomerman, D.; Kong, J.; McAfee, S. M.; Welch, G. C.; Kelly, T. L. *ACS Appl. Energy Mater*. **2018**, acsaem.8b01214. Copyright 2018 American Chemical Society.[99]

BCPs with dissimilar enough blocks (high χ) can self assemble into many morphologies useful for nano-lithography; however, like BHJ blends, they can be kinetically trapped when cast and occasionally require post deposition treatments.[71] Bai et al. showed that the swelling and drying rates used in the flow through VP-SVA system can be used to tune the orientation and morphology of polystyrene-*b*-polydimethylsiloxane.[94] Albert et al. showed that varying the relative concentration of two annealing solvents (using a microfluidic flow through annealing setup) poly(styrene-*b*-isoprene-*b*-styrene) could be manipulated to self-assemble into many patterns.[96] Gotrik et al. showed that by adding two different solvents to the flow through VP-SVA system, the morphology of BCP could be controlled to a finer level than mixed solvent bell jar annealing.[88] They showed many different morphologies were accessible from the polystyrene-*b*-polydimethylsiloxane by varying the ratio of toluene and n-heptane used in the annealing process.[88] In addition to different solvent concentrations, wetting and drying rates (which are

difficult to control with the bell jar method) have been shown to affect morphology in BCP and BHJ films, illustrating the importance of having a VP-SVA apparatus.[82,98] Despite the success in BCP self-assembly, few reports have used the flow through VP-SVA system to control OPV morphology.[43,69,100,101]

1.5. Organic Photovoltaic Materials

1.5.1. P3HT:$PC_{61}BM$

Poly(3-hexylthiophene) is one of the most studied OPV donor materials to date and $PC_{61}BM$ is the most studied acceptor for P3HT **(Chart 1.1)**.[102,103] P3HT:$PC_{61}BM$ solar cells were among the first solar cells to produce a promising efficiency, prompting many people to study it.[63,103–105] Cheap, scalable, and low energy synthesis,[106] moderate efficiencies,[107] robust physical properties,[108] and a large base of research allows P3HT to remain a model system.[102,103]

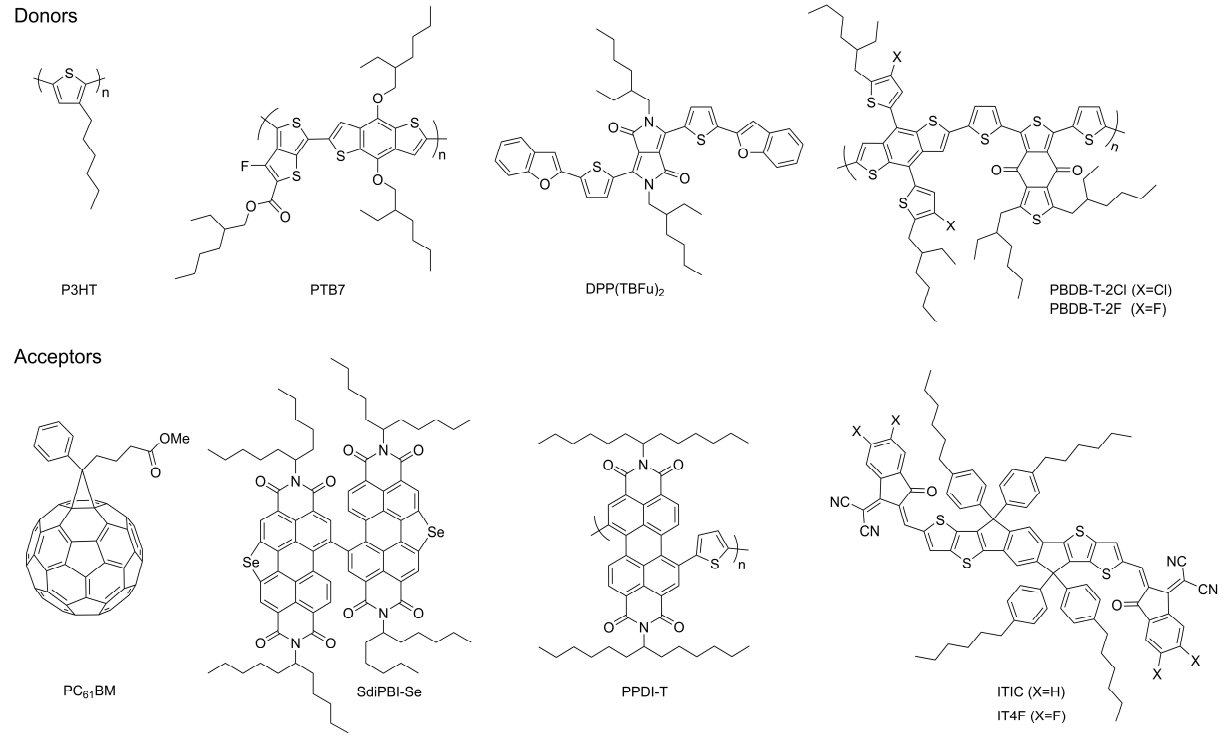

Chart 1.1: Chemical structures of common OPV materials.

The morphology and efficiency of P3HT:$PC_{61}BM$ devices improves with annealing.[102] The application of heat[61] (100 -180°C)[102] or solvent vapour[43] provides the polymer chains enough energy to rearrange locally and increase packing efficiency. Efficient packing brings the chromophores into closer proximity and excitons can begin to couple.[109] Exciton coupling results in a splitting of energy levels much like molecular orbitals.[110] In a J aggregate, excitons couple head to tail, resulting in a lower energy excited state **(Figure 1.9)**.[109,110] Conversely, H-aggregation results from excitons coupling parallel to each other resulting in a higher energy excited state (due to electrostatic repulsion) **(Figure 1.9)**.[109,110] P3HT has been shown to undergo H-aggregation with annealing.[109,111,112] Unlike small molecules, polymers have inter and intra-chain interactions, which result in multiple aggregation types.[109] The intra-chain orientation of repeat units in the regio-regular polymer act like J-aggregates aligning head to tail, and the inter-chain π-π stacking aggregation has H character.[109] The complex interplay between aggregation types leads to hybrid photo-physical properties which can be examined using UV-Visible (UV/Vis) spectroscopy.[109] The increase of π-π stacking from H-aggregation increases conjugation lengths in the P3HT; this lowers the band gap producing a red shift in the UV/Vis absorbance spectrum and increases charge carrier transport between P3HT chains.[72,109]

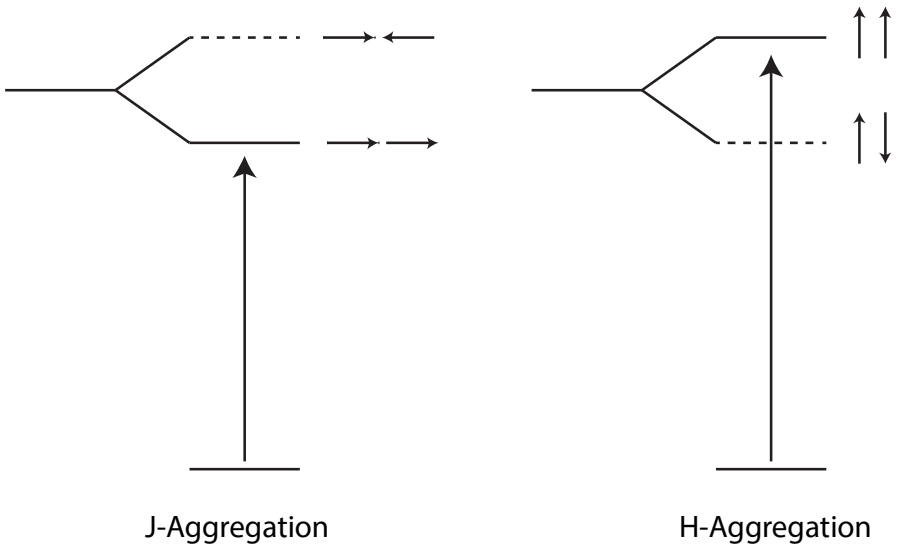

Figure 1.9: Schematic of H and J aggregation.

Despite the extensive study of P3HT:$PC_{61}BM$ morphology, device efficiencies are still limited by the inherent properties of the materials.[103] Due to the large bandgap of P3HT, light with wavelengths longer than 650 nm is not absorbed, and $PC_{61}BM$ has poor light absorbance overall.[103] This leaves much of the infrared (IR) light unabsorbed. To increase OPV efficiencies further, researchers examined and addressed the weaknesses of P3HT and $PC_{61}BM$ leading to higher efficiency modern OPV systems. To improve the light absorption of OPVs, researchers have investigated smaller band gap donors,[113] and designed non-fullerene acceptors (NFAs) that are better light absorbers.[114–117]

1.5.2. Small Bandgap Donors

The most common method used to lower the bandgap of donor materials is the push-pull system.[17] By adding an electron rich moiety (push) and an electron poor moiety (pull) to the donor polymer, the band gap is reduced by mixing of the push and pull regions' molecular orbitals **(Figure 1.10)**.[17] Additionally, the orbital energies (HOMO and LUMO) of the push-pull polymers can be tuned as the HOMO is primarily dictated by the push moiety, and the LUMO is primarily

dictated by the pull moiety.[17,118–120] Another method to lower the band gap is to stabilize the quinoidal resonance structure of the polymer.[2] The quinoidal resonance structure can contribute to increased light absorbance and higher charge carrier mobility;[2,121] cross-conjugation where there is no access to the quinoidal form has been shown to result in a large loss in device performance.[122]

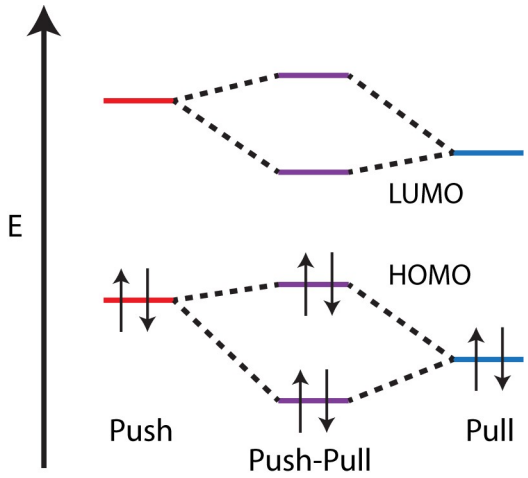

Figure 1.10: Molecular orbital diagram of generic push-pull polymer.

The PBDTTT family are among the most commonly used low band-gap donors and have become an important model system for modern push-pull donors.[103,113] The PBDTTT family is a group of polymers that contain a benzodithiophene (BDT) push moiety, a thieno[3,4-b]thiophene (TT) pull moiety, and various side groups; an example of a PBDTTT polymer is PTB7 shown in **Chart 1.1**.[113] PTB7 uses a combination of push-pull, and quinoidal resonance to lower the bandgap and increase light absorbance, and has reached efficiencies over 10%.[2,113] Another important family of push-pull donor polymers is the PBDB-T-2X family **(Chart 1.1)**, which at the time of writing held the record for highest OPV efficiency when paired with a NFA.[10,11]

Polymeric donors can suffer from a lack of reproducibility due to batch to batch variability of the molecular weights of polymers. To improve the reproducibility of lab to lab device performance, small molecule donors have also been investigated. Some of them (such as the

diketopyrrolopyrrole based DPP(TBFu)$_2$, **(Chart 1.1)**) perform well with solvent vapour annealing;[79,123] however, due to the lower performance of such devices (when compared to polymeric donors),[124–126] small molecule donors will not be discussed further.

1.5.3. Non-Fullerene Acceptors

Fullerenes make good electron acceptors because they have an isotropic π-system capable of accepting electrons from any angle. Additionally, they have good isotropic charge transport, and can break up donor stacking to form interpenetrating networks. Unfortunately, fullerenes have many drawbacks: they are expensive, they have poor light absorption, and their energy levels are not easily tunable.[114] To address these issues, researchers have recently focused on the development of non-fullerene acceptors.[114–116,127] NFAs have easily tunable band gaps and energy levels, allowing for selective light absorption and donor energy matching, respectively.[114–117] Efforts have been made to make NFAs affordable and easy to synthesize; however, the highest performing NFAs remain expensive (albeit cheaper than fullerenes) and synthetically challenging.[11]

NFAs fall into two primary categories, rylene diimides and push-pull conjugated materials.[116,117] Rylene diimides, such as perylene diimide (PDI), are excellent light absorbers, have high electron affinity, good charge transport, and low cost. PDI has a large conjugated π system that stacks to form large crystallites which improves charge transport.[117,127–130] Unfortunately, large crystallites can produce extremely large domains which leads to high geminate recombination losses as excitons are unable to diffuse to the boundary between the donor and PDI.[117] In an effort to improve PDI morphology, the PDI units are usually attached to a linker designed to break up π stacking in the material; however, a careful balance must be maintained to not decrease the charge transport properties while reducing domain sizes.[78,115,117,128,131–134] The

most effective approach to break up aggregation while maintaining charge transport is to add a linker to the PDI which induces a twist in the molecule, but still allows the PDI "paddles" to interact and transport charge, exemplified by SdiPBI-Se **(Chart 1.1)**.[78,117,135,136] PDI NFAs can be produced cheaply and with fewer synthetic steps than push-pull NFAs; however, challenges still remain with fine tuning solubility, morphology control, and charge transport, which currently limits efficiencies to around 10%.[78,135,136]

NFAs with a push-pull system currently hold the record for OPV efficiency (IT4F, 14.5%, **Chart 1.1**) when matched with a modern donor.[10,11] The push-pull NFAs follow the same principles as push-pull donors, which decreases the band gap of the material **(Figure 1.10)** and localizes the HOMO on the electron rich units and the LUMO on the electron poor units.[116] The localized HOMO and LUMO serve two purposes. First, the large intramolecular charge transfer between push and pull units leads to a strong, broad light absorption.[114] Second, if the LUMO of the acceptor molecule is less sterically hindered, the donor molecule will have a higher probability of LUMO overlap with the acceptor molecule; this increases the probability of electron transfer from the donor molecule to the acceptor molecule.[116,137]

1.6. X-ray Diffraction

X-ray diffraction (XRD) experiments probe the atomic spacing between planes of atoms using a phenomenon known as diffraction. When two X-rays (of the same wavelength) are reflected off different planes of a crystal they can interact constructively or destructively depending on the spacing of the crystal planes.[138] If the difference in distance travelled is equal to an integer value of the wavelength of the X-ray, the two waves interact constructively, and otherwise they interact destructively.[138] This gives rise to Bragg's Law, **(Equation 1.4)** where n is an integer, λ is

the wavelength of light, d is the spacing between lattice planes of the crystal, and θ is the incidence angle of the light.[138]

$$n\lambda = 2dsin(\theta) \quad (1.4)$$

Single crystal XRD can provide a complete picture of the unit cell and extended packing of a crystalline material;[138] however, OPV materials tend to be amorphous or semi-crystalline and single crystals can be difficult to obtain.[78] Powder XRD (PXRD) provides less information than single crystal XRD as the signals from many smaller crystallites overlap, broadening diffraction signals from small dots to rings.[139] Despite this, PXRD is a powerful tool for determining the crystalline properties of molecules.[140] As an analytical technique, PXRD can be used to examine the fingerprint of a crystalline material to determine the make up of a blend of crystalline powders.[139] However, one must take care when using PXRD as an analytical technique as any amorphous impurities will not diffract and remain unseen by the PXRD pattern.[139] Additionally, if a close enough model exists, a Rietveld refinement can be performed to determine the crystalline structure of the powder material.[139] However, due to the large variation in stacking, and only partial crystallinity of common OPV materials, a Rietveld refinement is difficult, time consuming, and usually requires a computational starting point. More useful for this thesis, the peak broadening of PXRD signals can be related to crystallite size and strain using the Scherrer equation **(Equation 1.5)**,[141] where τ is the mean size of crystallite domains, K is the shape factor, λ is the X-ray wavelength, β is the line broadening of the diffraction peak, and θ is the Bragg angle.

$$\tau = \frac{K\lambda}{\beta cos\theta} \quad (1.5)$$

1.6.1. Grazing Incidence Wide Angle X-ray Scattering

Grazing incidence wide angle X-ray scattering (GIWAXS) is a variation of PXRD, where a collimated X-ray beam interacts with the sample at a low incident angle. Organic molecules have a low Z (atomic number) which results in poor interaction with X-rays because scattering occurs when X-rays interact with the electron density of atoms.[139] By using a grazing incidence angle, the path length of the X-rays in the organic sample is increased, which increases the probability of X-rays scattering from the organic material.[142] This increases signal to noise and allows the examination of thin films of organic molecules.[142]

Benchtop GIWAXS setups are available; however, most GIWAXS experiments are performed at synchrotrons. Synchrotron radiation has a high X-ray flux, allowing for faster measurements than benchtop X-ray sources which facilitates *in situ* and *operando* measurements.[143] In a synchrotron, a cluster of electrons is fired from an electron gun and accelerated to injection velocity by a linear particle accelerator.[143] Once injected the electron cluster is accelerated around a booster ring where they reach relativistic speeds.[143] Once up to relativistic speed the electron cluster is injected into the storage ring where the cluster is accelerated around corners at specific locations.[143] The accelerating electrons give off broad spectrum radiation called synchrotron radiation which is collected by beamlines.[143] At the Canadian Light Source (CLS) (where the GIWAXS for this thesis was performed) the Hard X-ray MicroAnalysis (HXMA) beamline collects hard X-rays by using filters to remove all lower and higher energy photons. The hard X-rays are then diffracted off a Si (111) crystal monochromator which uses Bragg diffraction to select a single X-ray wavelength.[143] The X-ray beam is then sent through a vertical and horizontal slit to collimate the beam.[143]

When analysing GIWAXS data some experimental considerations such as the scattering geometry must be examined **(Figure 1.11)**.[144] The scattering vector (q) is the momentum transfer vector of diffracted X-rays in reciprocal space and can be represented using **Equation 1.6**.[145] When Bragg's law **(Equation 1.4)** is substituted into the scattering vector equation **(Equation 1.6)** it is shown that the scattering vector is independent of the wavelength of incident light and only depends on the d spacing of the material **(Equation 1.7)**; this makes it a useful unit of measurement for synchrotron diffraction experiments where the wavelength of incident X-rays is easily varied. The total scattering vector (q) can be broken down into its component vectors, q_x, q_y, and q_z.[144] When considering two dimensional (2D) GIWAXS patterns, the q_x and q_y vectors are in the plane of the substrate and overlap; the sum of q_x and q_y is defined as q_r **(Equation 1.8)**.[144] The program GIXSGUI written and distributed by Zhang Jiang can be used to calibrate GIWAXS patterns using a standard diffraction pattern (usually silver behenate for organic molecules) collected at the same sample to detector distance and scattering geometry as the sample.[144]

$$q = 4\pi \frac{\sin(\theta)}{\lambda} \tag{1.6}$$

$$q = \frac{2\pi}{d} \tag{1.7}$$

$$q_r = ({q_x}^2 + {q_y}^2)^{1/2} \tag{1.8}$$

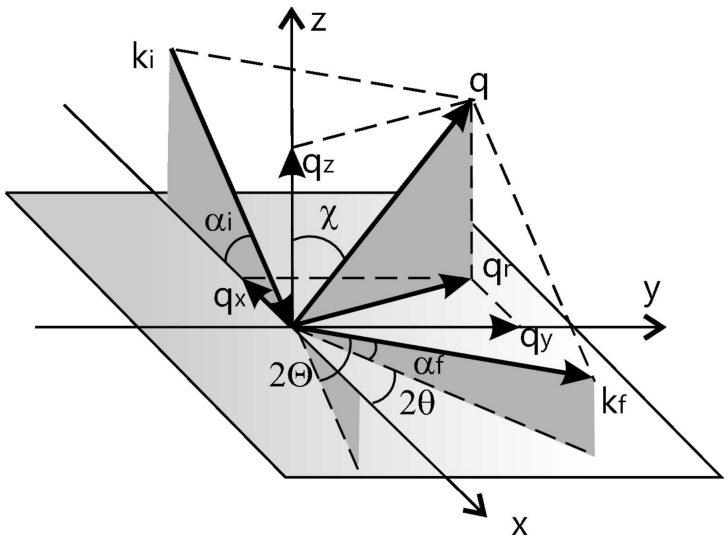

Figure 1.11: Schematic diagram of grazing-incidence scattering geometry in the sample reference frame. Reproduced with permission of the International Union of Crystallography from reference Jiang, Z. *J. Appl. Cryst.* **2015**, *48*, 917.[144]

The scattering vectors are vectors in reciprocal space with exact magnitudes and directions. An infinite number of scattering vectors in all directions with the same overall momentum can be modelled using an interaction sphere called the Ewald sphere.[146] Where the Ewald sphere interacts with a point on the reciprocal lattice diffraction occurs.[146] Unfortunately, when the Ewald sphere interacts with a 2D detector in real space, the entire sphere cannot be imaged.[144] This results in a warping of the diffraction pattern on the detector which must be corrected with post processing and results in a missing wedge along q_z **(Figure 1.12)**.[144]

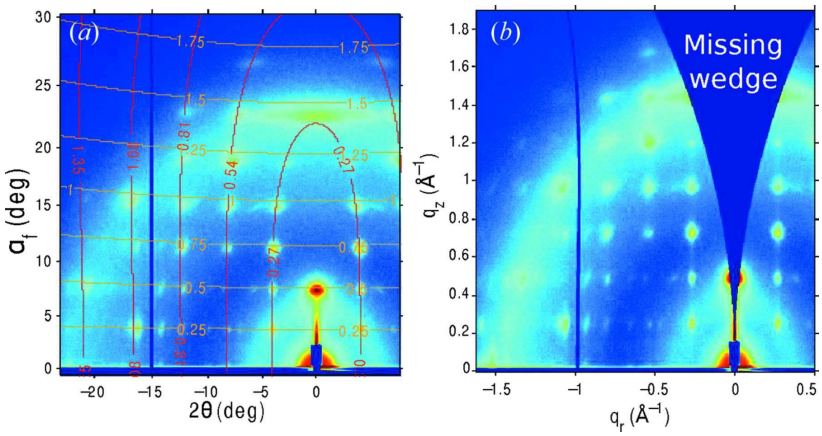

Figure 1.12: GIWAXS pattern (a) before and (b) after reshaping with respect to q_z and q_r, whose contour lines are shown in gold and red in (a). Reproduced with permission of the International Union of Crystallography from reference Jiang, Z. *J. Appl. Cryst.* **2015**, *48*, 917.[144]

An isotropic distribution of crystallites in a thin film will produce a ring with equal intensity across q_z and q_r; however, some materials orient themselves preferentially (with respect to the substrate) when cast in thin films.[147] Preferred orientation is shown in diffraction patterns as a reduction of intensity at specific parts of the diffraction ring **(Figure 1.13)**.[147] Whether the intensity increases or decrease along q_z or q_r depends on the orientation of the planes (parallel or perpendicular to the substrate).[147] In the example in **Figure 1.13** the crystallite planes oriented parallel to the substrate increased diffraction intensity along the q_z axis and decreased intensity along the q_r axis.[147]

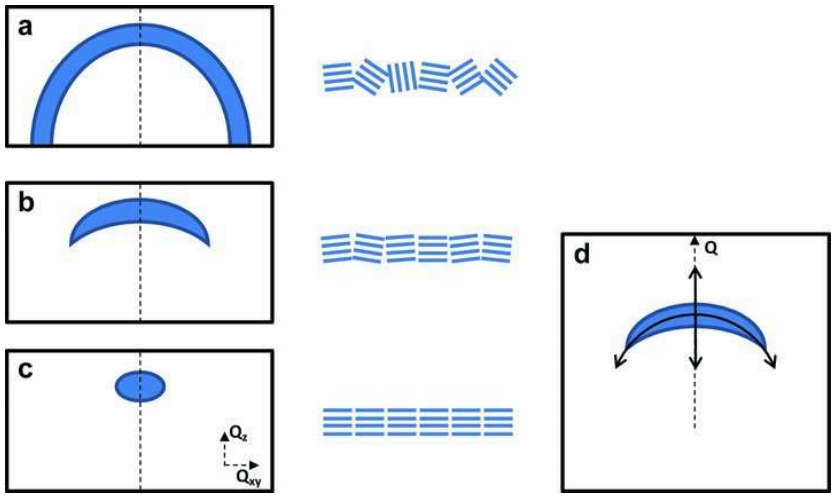

Figure 1.13: Illustrations of example diffraction patterns for different microstructures. (a) Randomly oriented films produce a sharp ring, (b) oriented films with broad orientation distribution produce an arc, and (c) highly oriented films produce an ellipse. The inset shows the crystal orientation distribution that produced the pattern. (d) Diagram of the measurement scan for a q_z scan for measuring plane spacing and a rocking curve for measuring orientation distribution. Reproduced from DeLongchamp, D. M.; Kline, R. J.; Fischer, D. A.; Richter, L. J. Toney, M. F. *Adv. Mater.* **2011**, *23*, 319. Copyright © 2011 WILEY-VCH Verlag GmbH & Co. KGaA, Weinheim.[147]

The crystallinity of P3HT has been well studied by GIWAXS in the literature.[24,43,60,61,147–150] P3HT often adopts a preferred orientation with the aromatic thiophene ring lying either parallel (face on) or perpendicular (edge on) to the substrate **(Figure 1.14)**.[149] **Figure 1.15** illustrates the diffraction pattern of primarily face on P3HT with a minor amount of edge on oriented crystallites and labels the diffraction peaks.[43] For face on orientation the P3HT (100) peak intensity is weighted towards the q_{xy} (q_r) axis, and the intensity of the (010) π stacking peak is weighted towards the q_z axis, and vice-versa for edge on orientation.[43] P3HT tends to adopt edge on orientation under slow drying conditions,[43,151] and thermal annealing,[61] indicating that edge on orientation is the thermodynamically favoured orientation for P3HT.[152,153] Face on orientation in P3HT has been achieved by kinetically trapping P3HT using a fast drying casting solvent such as chloroform.[43,151] Face on orientation of P3HT results in the π stacking direction perpendicular to the substrate which has been shown to increase charge transport in P3HT;[151,153,154] however, one

report by Gargi et al. suggests that the increased charge transport is mainly due to other factors (casting spin speed, molecular weight, casting solvent) which are difficult to isolate from P3HT orientation.[149]

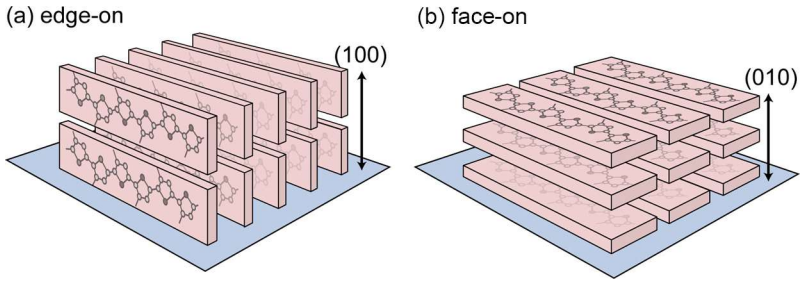

Figure 1.14: Illustration of the P3HT backbone stacking orientation relative to a substrate for an edge-on (a) and a face-on (b) stacking configuration. Adapted with permission from Gargi, D.; Kline, R. J.; DeLongchamp, D. M.; Fischer, D. A.; Toney, M. F.; O'Connor, B. T. *J. Phys. Chem. C* **2013**, *117*, 17421. Copyright 2013 American Chemical Society.[149]

One of the primary inspirations for the work done in this thesis is a report from Verploegen et al. that explores *in situ* GIWAXS of P3HT during solvent vapour annealing with various solvents.[43] Verploegen et al. showed that as cast films of neat P3HT, and 3:1 and 1:1 blend ratio BHJ films of P3HT:$PC_{61}BM$ showed preferred orientation of P3HT face on when cast from chloroform (kinetically trapped) and edge on when cast from chlorobenzene (thermodynamically favoured) **(Figure 1.15** and **Figure 1.16)**.[43] They found that films cast from chlorobenzene did not undergo significant changes with SVA and opted to discuss chloroform cast films.[43] They found that during SVA with all solvents tested, the P3HT films swelled (as indicated by an increase in the layer spacing of the lamellar stacking), and after annealing they de-swelled; however, the d spacing remained larger after annealing than the as cast films.[43] It was also shown that chloroform and THF vapours decreased the full width at half maximum (FWHM) of the P3HT (100) peak indicating an increase in crystallite size after annealing.[43] Hexanes on the other hand resulted in little decrease in the FWHM, indicating that the crystallite sizes remained constant.[43] Finally, they

showed that they were able to maintain face on orientation after SVA, indicating that unlike thermal annealing,[61] SVA did not allow the polymer films enough freedom of movement to change orientations.[43]

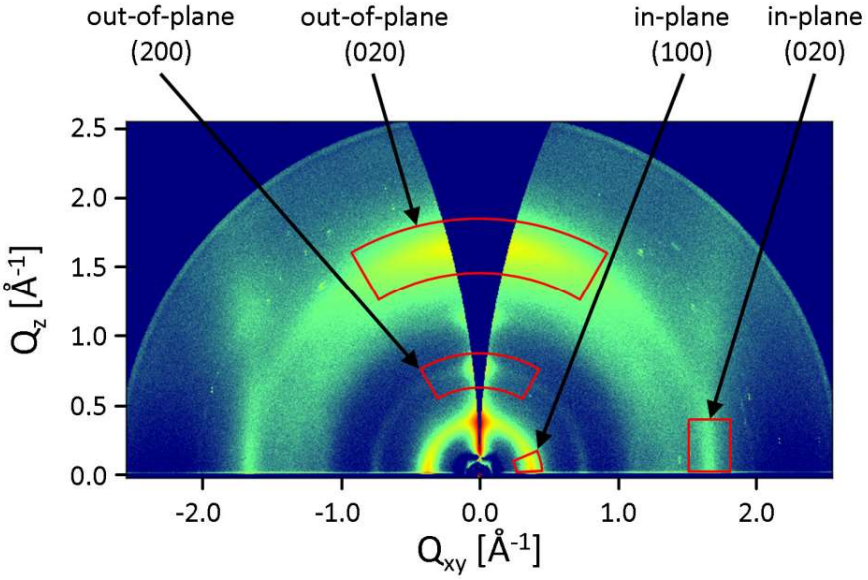

Figure 1.15: 2-D GIWAXS image of as-cast P3HT thin film. Reproduced with permission from Verploegen, E.; Miller, C. E.; Schmidt, K.; Bao, Z.; Toney, M. F. *Chem. Mater*. **2012**, *24*, 3923. Copyright 2012 American Chemical Society.[43]

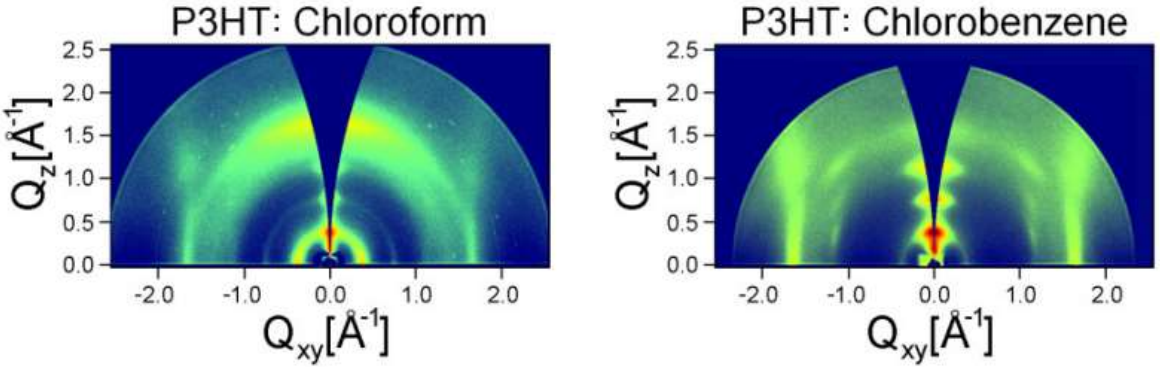

Figure 1.16: 2-D GIWAXS images as-cast thin films of neat P3HT cast from chloroform and chlorobenzene. Adapted with permission from Verploegen, E.; Miller, C. E.; Schmidt, K.; Bao, Z.; Toney, M. F. *Chem. Mater*. **2012**, *24*, 3923. Copyright 2012 American Chemical Society.[43]

1.7. Force Microscopy Techniques

1.7.1. Atomic Force Microscopy

Atomic force microscopy is an imaging technique that scans a sharp probe across a sample measuring changes in sample height.[155] The instrument consists of a sharp tip mounted on a cantilever, a laser and 2D detector, and a piezoelectric crystal.[155,156] A piezoelectric material changes size in at least one dimension when an electric field is applied. To operate an AFM, a laser is reflected off the back of the cantilever and is centered on the 2D detector.[157] In contact mode, the tip is then scanned along the surface of the sample and changes in sample height are detected as the tip bends the cantilever and the laser moves on the 2D detector.[157] In constant force mode, the piezoelectric crystal expands or contracts as needed to lower or raise the AFM tip respectively.[157] The vertical motion of the piezoelectric crystal is then recorded as height information at each pixel scanned by the tip.[157] In constant height mode, the fixed end of the cantilever remains at the same height as it is rastered over the sample; deviations in sample height are measured by the defection of the cantilever and converted into a height image.[157]

AFM records images of the material surface and the resolution is only limited by the size and radius of curvature of the tip. The image taken in AFM is a convolution of the tip and the surface characteristics.[147] Therefore, when the tip is functionalized with a single carbon monoxide molecule, the electron density of chemical bonds can be imaged **(Figure 1.17)**;[158] however, dull or damaged tips greatly reduce image resolution and can induce imaging artifacts.[157] Artificial broadening of sample features occurs when the edge of the AFM tip comes into contact with a rise in the sample before the point of the tip does. This occurs when there are sudden dramatic changes in sample height.[157] Additionally, artifacts such as twinning of the image features or loss of resolution can occur if the tip breaks or picks up material from the sample.[157]

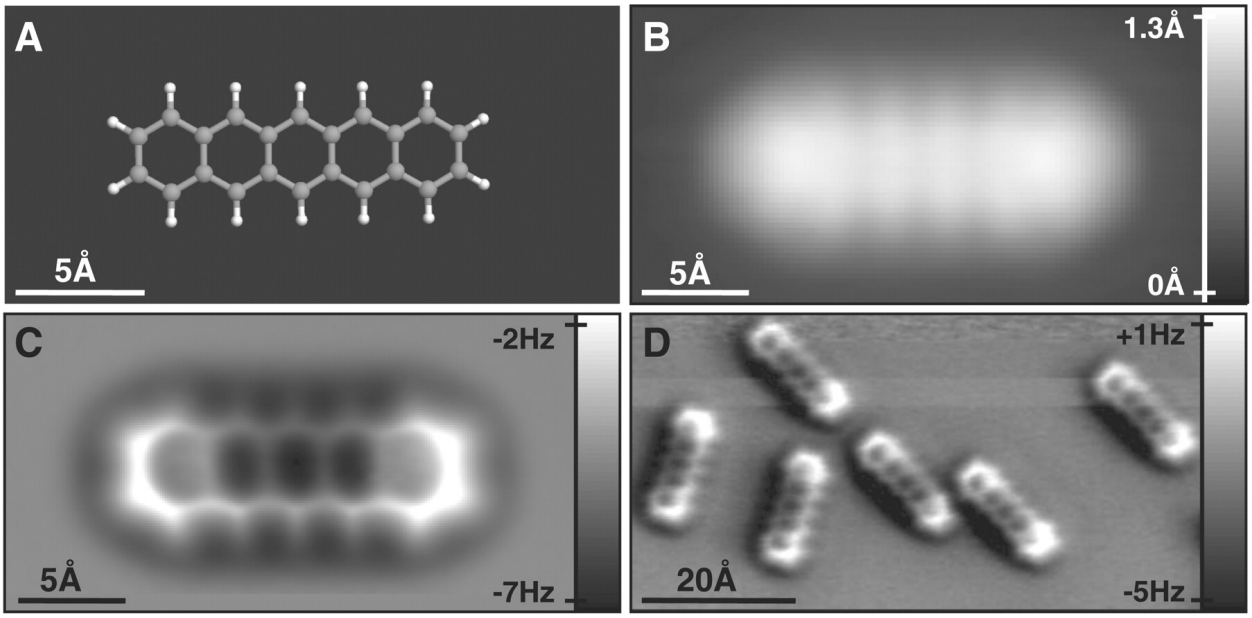

Figure 1.17: Scanning tunnelling microscopy and AFM imaging of pentacene on Cu(111). (a) Ball-and-stick model of the pentacene molecule. (b) Constant-current scanning tunnelling microscopy and (c and d) constant-height AFM images of pentacene acquired with a CO-modified tip. Imaging parameters are as follows: (b) set point I = 110 pA, V = 170 mV; (c) tip height z = –0.1 Å [with respect to the scanning tunnelling microscopy set point above Cu(111)], oscillation amplitude A = 0.2 Å; and (d) z = 0.0 Å, A = 0.8 Å. The asymmetry in the molecular imaging in (d) (showing a "shadow" only on the left side of the molecules) is probably caused by asymmetric adsorption geometry of the CO molecule at the tip apex. From Gross, L.; Mohn, F.; Moll, N.; Liljeroth, P.; Meyer, G. *Science* **2009**, *325* (5944), 1110. Reprinted with permission from AAAS.[158]

In contact mode AFM, there are high lateral forces exerted on the sample by the tip. These can be reduced by using a more flexible tip or using tapping mode. In "intermittent contact" or "tapping mode" AFM, the tip oscillates and taps the surface (or close to the surface in non-contact mode) of the sample.[155] When in tapping mode, the cantilever is being driven at some oscillation frequency (usually at or near the cantilever's natural resonant frequency).[155] When the tip comes in close proximity to a sample it is first attracted (Van der Waal's forces, dipole-dipole interactions, etc.) and then repelled (electrostatic forces) by the material's surface, which alters the amplitude of oscillation.[159] The piezoelectric crystal then adjusts the height of the cantilever to regenerate the appropriate oscillation amplitude and the movement of the piezoelectric is recorded as height

information. Inelastic collisions between the sample surface and the AFM tip result in a loss of energy and consequently a change in phase of the cantilever oscillation **(Figure 1.18)**.[160,161] The degree of phase changes between the drive signal and the response signal can be measured and plotted as the tip is rastered across the sample surface resulting in a phase image.[160] Therefore materials in a blend can be distinguished in a phase image if they have sufficiently different mechanical properties.[155]

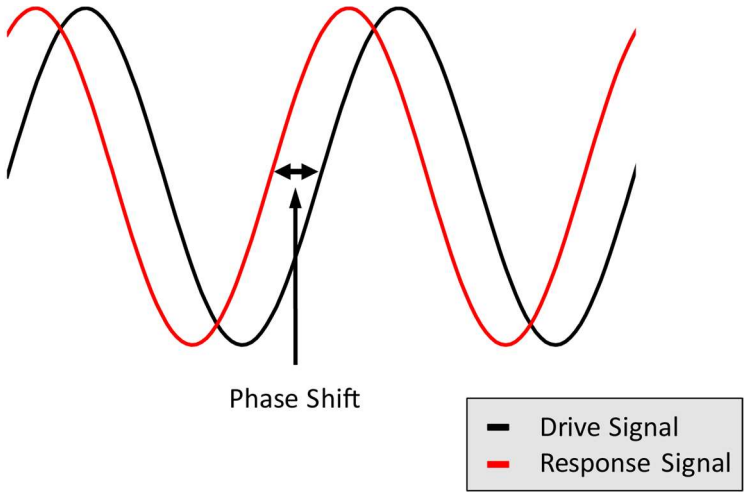

Figure 1.18: Phase shift in AFM frequency detected for phase imaging.

Tapping mode is more suitable for imaging organic materials because it greatly reduces the lateral forces on the sample, and the phase image can be used to distinguish materials (provided there is a large enough difference in mechanical properties).[155,162] The cantilever phase changes are dependent on tapping force, and tip-sample interactions; therefore, it is often difficult to ascertain which phase corresponds to which material without more advanced atomic force microscopy techniques.[57,161–163]

One method to determine specific material placement in a BHJ film was developed by Jovanov et al.[162] They chose PTB7 as the donor and PCBM as the acceptor, which have sufficiently different mechanical properties to be distinguished by phase AFM.[162] A phase reference standard

was created by doctor blading PTB7 onto a glass substrate and annealing the sample to remove solvent; PCBM was then drop cast onto a corner of the film in cyclohexane (a non-solvent for PTB7) to prevent film mixing.[162] After drying, a phase image was taken at the edge of the PCBM droplet overlapping the PTB7 film.[162] The phase of neat PCBM and neat PTB7 were then recorded.[162] Using the reference phases for the materials they could determine which cantilever phase corresponded to which material in the film.[162] They found that PCBM formed large "flake-like clusters" (that increased in size as the PCBM content was increased) imbedded in a PTB7 matrix.[162] Devices showed an increase in J_{SC} and a decrease in R_S as the size of the PCBM clusters increased, indicating better charge transport through the devices leading to higher efficiencies.[162] While this technique is useful for material determination, care must be taken when performing phase experiments to ensure the settings of the AFM are chosen correctly and remain consistent throughout the experiment. The phase of the cantilever can invert if the force exerted by the cantilever on the sample is changed.[161] Additionally, AFM is a surface sensitive technique, so care must be taken when applying AFM results to interpret bulk material morphology.

1.7.2. Photo-induced Force Microscopy

Photo-induced force microscopy (PiFM) can image materials in a film directly provided they have a unique IR absorbance. PiFM uses a quantum cascade laser to excite vibrations in molecules with IR light while performing tapping mode atomic force microscopy with a metal coated tip **(Figure 1.19)**.[57,163] The absorbance selection rules for IR spectroscopy require a change in dipole moment of the absorbing molecule; this change in dipole induces a dipole in the metal AFM tip, generating an attractive force.[163] The IR laser is pulsed at the difference frequency (f_m) between the AFM topographic detection frequency (f_1) and the PiFM detection frequency (f_0) ($f_m = f_1 -$

f_0) which is known as side band modulation mode.[163] Operating in side band modulation mode maximises the amplitude of the PiFM signal in the localized force region of the of the tip to sample distance, which in turn increases the clarity of the PiFM signal.[163]

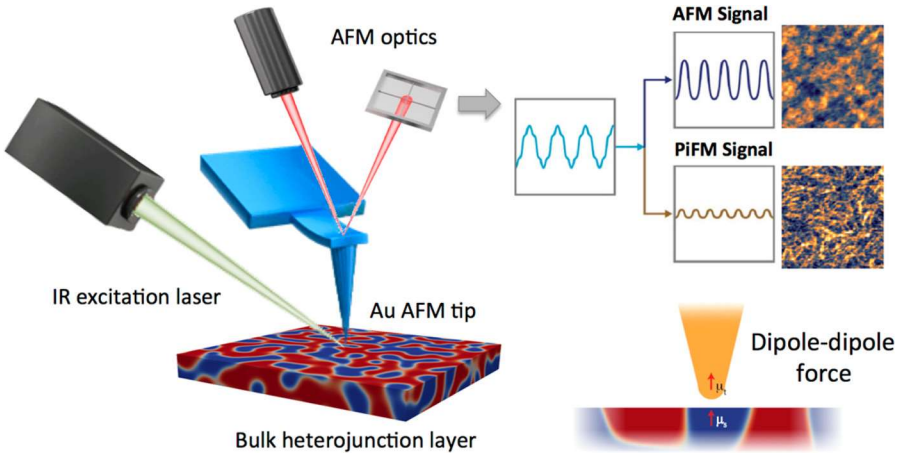

Figure 1.19: Simplified schematic of the PiFM setup. Reprinted with permission from Gu, K. L.; Zhou, Y.; Morrison, W. A.; Park, K.; Park, S.; Bao, Z. *ACS Nano*, **2018**, *12*, 1473. Copyright 2018 American Chemical Society.[57]

Gu et al. were able to image the domains of an all polymer BHJ using PiFM.[57] Due to the similarities in optical and mechanical properties of the donor and acceptor polymers, phase AFM, and electron and optical microscopy techniques provide poor material distinctions; however, PiFM can distinguish between two polymeric materials provided they have at least one unique IR absorbance.[57] Gu examined the morphology of a BHJ blend of poly(isoindigo-bithiophene) with 10 mol % polystyrene side chains (PII-2T-PS) as the donor and a polymeric PDI based acceptor **(**PPDI-T, **Chart 1.1)** cast with various concentrations of the casting additive 1-CN.[57] They could quantitatively determine domain sizes which they reproduced with resonant soft X-ray scattering to confirm the results.[57] The results showed that the domain sizes of the BHJ materials decreased with increasing 1-CN concentration.[57] More importantly, they showed that PiFM could image

domains of BHJ that were too similar to examine by AFM topography or phase imaging **(Figure 1.20)**.[57]

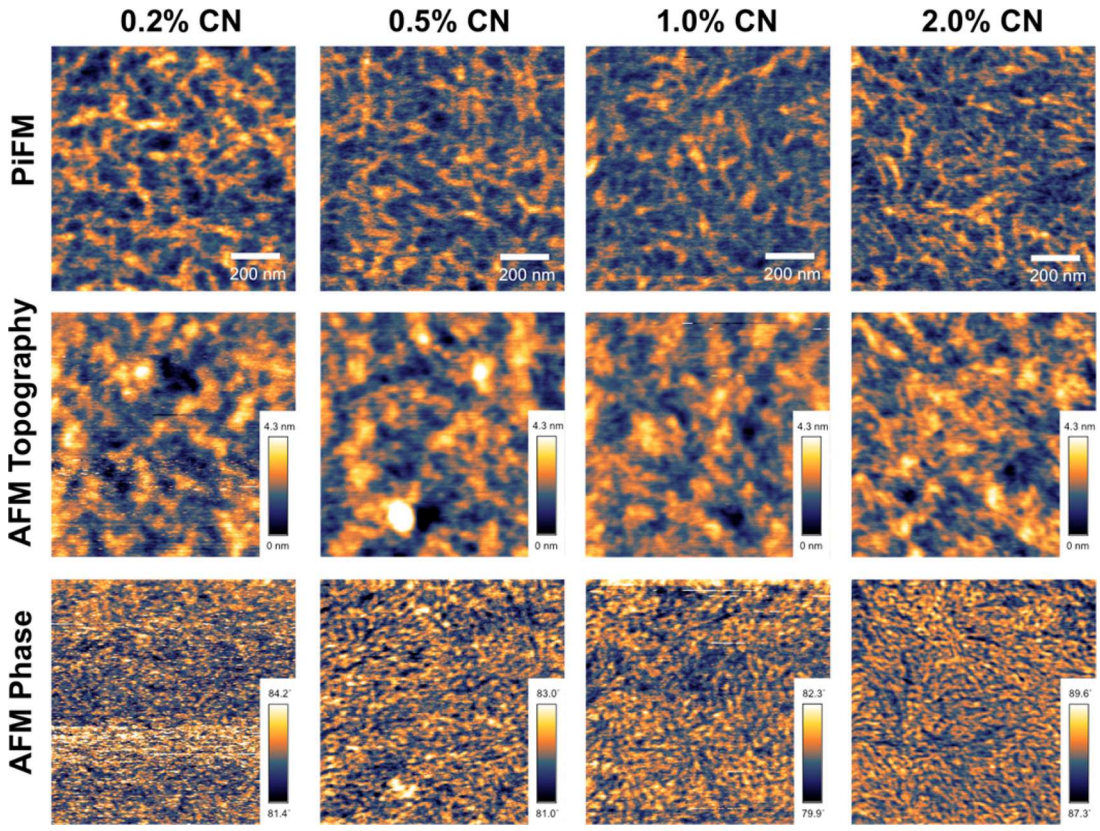

Figure 1.20: Donor phase PiFM (top), AFM topography (middle), and AFM phase (bottom) of PII-2T-PS/PPDI-T BHJ films. All images are 1 × 1 μm. Reprinted with permission from Gu, K. L.; Zhou, Y.; Morrison, W. A.; Park, K.; Park, S.; Bao, Z. *ACS Nano*, **2018**, *12*, 1473. Copyright 2018 American Chemical Society.[57]

1.8. Objectives

The primary hypothesis of the thesis is that: **The morphology of organic solar cells can be controlled by tuning the solvent vapour concentration during solvent vapour annealing**.

The primary objective of the research was to increase the level of OPV morphology control in the solvent vapour annealing technique. To accomplish this objective, several secondary objectives were identified:

1. Adapt the variable pressure flow through solvent vapour annealing apparatus commonly used in block copolymers to anneal OPVs.
2. Use the flow through VP-SVA apparatus to anneal a well-known model system P3HT:$PC_{61}BM$ to validate the system's control over morphology.
3. Use the flow through VP-SVA system to control the morphology of a modern OPV system and illustrate the versatility of the variable pressure flow through solvent vapour annealing system.

1.9. Co-Authorship Statement

I am the primary author and I carried out all the experimental work with the following exceptions. Kyle Fransishyn from the University of Saskatchewan helped design the UV/Vis and GIWAXS chambers and assisted with the GIWAXS experiments at the CLS. Nick Randell, Rick Pettipas, and Timothy Kelly from the University of Saskatchewan assisted with GIWAXS experiments at the CLS. Seth McAfee from the University of Calgary synthesized **PDI-DPP-PDI** and provided casting conditions. Jessica Kong from the University of Washington performed the PiFM measurements.

1.10. Manuscript Permission

Chapter 2: Experimental

2.1. Materials

All materials were used as received unless otherwise stated. Poly(3-hexylthiophene) (M_w = 57000 g/mol, dispersity (Đ) = 2.4, 91% regioregularity) was purchased from Rieke Metals. Phenyl-C_{61}-butyric acid methyl ester was purchased from Nano-C. Poly{4,8-bis[5-(2-ethylhexyl)thiophen-2-yl]benzo[1,2-b:4,5-b']dithiophene-2,6-diyl-alt-3-fluoro-2-[(2-ethylhexyl)carbonyl]thieno[3,4-b]thiophene-4,6-diyl} (PTB7-Th) was purchased from Luminescence Technology Inc. (Lot: S9139-170220001). PDI-DPP-PDI was provided by Seth McAfee from the Welch group at the University of Calgary.[78] Zinc acetate dihydrate, acetone, isopropanol and chloroform were purchased from Fisher Scientific. Silver behenate, 2-methoxyethanol, and ethanolamine were purchased from Sigma-Aldrich.

2.2. Characterization

UV/Vis spectroscopy was carried out on thin films deposited on glass/ZnO substrates using a Cary 6000i spectrophotometer. *In situ* experiments were carried out in a custom-built, gas-tight aluminium chamber. Scans were performed from 900 nm to 250 nm at a rate of 1010 nm/min. Attenuated total reflection Fourier transform infrared (ATR-FTIR) experiments were carried out on a Bruker Alpha Platinum-ATR FTIR spectrometer. PiFM was performed by Jessica Kong on thin films on ITO/ZnO substrates using a Molecular Vista microscope at the University of Washington. Images were acquired in sideband mode, where the PiFM and topography images were obtained at the first and second mechanical resonance frequencies of a Pt coated, Si

MikroMasch cantilever (320 kHz and 1.9 MHz, respectively). Scans were acquired at 0.25-0.35 lines/sec with time constants of 10-20 ms.

2.3. GIWAXS Parameters

GIWAXS experiments were performed at the CLS using the HXMA beamline. A photon energy of 12.7 keV was selected using a Si(111) monochromator. GIWAXS patterns were collected with a SX165 charge-coupled device detector (80 μm pixel size; 16.3 cm diameter), which was placed 158 mm from the sample center. The beam slits were set to a 0.10 mm vertical gap and a 0.30 mm horizontal gap. Thin film samples were deposited on <100> silicon wafers with a ~ 100 nm thermal oxide layer, and the angle of incidence of the X-ray beam was set to 0.02°. The GIWAXS data were calibrated against a silver behenate standard and analyzed using GIXSGUI.[144]

2.4. Device Characterization

Current-voltage measurements on OPV devices were performed inside a nitrogen-filled glovebox using a Keithley 2400 source-measure unit. The cells were illuminated by a 450 W Class AAA solar simulator equipped with an AM1.5G filter (Oriel Instruments, Sol3A) at a calibrated intensity of 1 Sun, as determined by a standard silicon reference cell (Oriel Instruments, 91150V). The cell area was defined to be 0.0708 cm^2 by a non-reflective anodized aluminum mask.

2.5. Variable-Pressure Solvent Vapour Annealing

VP-SVA was performed using a stream of nitrogen carrier gas connected to two Alicat MC-500SCCM-D/5M mass flow controllers set to a combined total flow rate of 250 standard cubic centimeters per minute (SCCM). One gas stream was passed through two solvent bubblers

connected in series to become saturated with solvent vapour. The second gas stream remained dry. The two gas streams were mixed, with the relative flow rates defining the partial pressure of the solvent vapour (p). The solvent concentrations are reported as p/p_{sat} where p_{sat} is the saturation vapour pressure. All annealing experiments were performed by flowing dry nitrogen over the sample for two minutes, followed by 30 minutes of solvent vapour annealing and 30 minutes of drying under a flow of dry nitrogen.

2.6. Substrate Preparation

Glass substrates (Fisherbrand glass microscope slides) and <100> oriented silicon wafers (100 nm thermal oxide, University Wafer) were prepared by cutting into 25 mm × 25 mm squares, and ITO-patterned glass substrates (25 mm × 25 mm, R_s = 20 Ω/sq) were purchased from Xin Yan Technology Ltd. The substrates were cleaned by successive sonication for 20 minutes in 2% Extran detergent in distilled water, Millipore water, acetone, and isopropanol and stored under isopropanol until use. All substrates were blown dry with filtered nitrogen and UV/ozone cleaned for 15 minutes immediately prior to use.

2.7. ZnO Films

ZnO sol-gel precursor solutions were prepared by dissolving zinc acetate dihydrate (108 mg, 0.49 mmol) and ethanolamine (30 µL, 0.50 mmol) in 2-methoxyethanol (1.0 mL) and stirring vigorously overnight. The solution was then filtered through a 0.45 µm PTFE syringe filter; 50 µL was spin coated onto glass or ITO-coated glass substrates at 5000 r.p.m. for 60 s with an acceleration of 2500 r.p.m./s. The films were then annealed at 180 °C for 15 minutes, and brought into a nitrogen-filled glovebox while still above 120 °C.

2.8. P3HT:$PC_{61}BM$ Films

1:0.6 (w/w) P3HT:$PC_{61}BM$ (10 mg/mL total concentration) solutions in chloroform (dried over 4 Å molecular sieves and degassed in vacuo) were prepared inside a nitrogen-filled glovebox. The solutions were weighed then stirred overnight at room temperature. In the morning, the vials were weighed again and topped up with an appropriate amount of chloroform. The solutions were then filtered through a 0.45 μm PTFE syringe filter before being spin coated (1000 r.p.m. for 15 seconds and 3000 r.p.m. for 45 seconds) onto either glass/ZnO, ITO/ZnO, or silicon substrates. The films were then solvent annealed as described in chapter 3.

2.9. PTB7-Th:PDI-DPP-PDI Films

Neat PTB7-Th (10 mg/mL), PDI-DPP-PDI (10 mg/mL), and 2:3 (w/w) PTB7-Th:PDI-DPP-PDI (10 mg/mL total concentration) solutions in chloroform were prepared in air. The solutions were weighed then stirred overnight at room temperature. In the morning, the vials were weighed again and topped up with an appropriate amount of chloroform. The solutions were then filtered through a 0.45 μm syringe filter before being spin coated (1500 r.p.m. for 60 s, with an acceleration of 10000 r.p.m./s) onto either glass/ZnO, ITO/ZnO, or silicon substrates. The films were then solvent annealed as described in chapter 3.

2.10. OPV Device Fabrication

After depositing and annealing the ITO/ZnO/P3HT:$PC_{61}BM$ and ITO/ZnO/PTB7-Th:PDI-DPP-PDI films, MoO_{3-x} (7 nm, 0.1 Å/s) and Ag (100 nm, 0.3 Å/s) were thermally evaporated at a base pressure of 1×10^{-6} mbar.

Chapter 3: Results and Discussion

3.1. Introduction

In this thesis, a flow through VP-SVA apparatus was designed to control the morphology of OPV active layers **(Figure 1.8)**. P3HT:$PC_{61}BM$ **(Chart 3.1)** was used to validate the ability of the flow through VP-SVA system to control active layer morphology. P3HT:$PC_{61}BM$ is an excellent model system because it has been well studied and its morphological changes are well known.[43,70,72,77,104,111] Once the system was validated, a PTB7-Th:PDI-DPP-PDI blend was examined as a representative of modern OPV BHJ blends **(Chart 3.1)**.[78] PTB7-Th:PDI-DPP-PDI has been shown to over anneal in saturated chloroform concentrations, making it an ideal candidate for flow through VP-SVA.[78] In this thesis it is shown that SVA with increasing chloroform vapour concentration increases phase separation in the BHJ blends as indicated by UV/Vis spectroscopy and PiFM. The crystallite sizes of the active layer materials also increase with chloroform vapour concentration for both neat materials and BHJ blends as shown by GIWAXS. Finally, it is shown that the combination of phase separation and increasing crystallite size can improve the device performance of the selected BHJ blends; however, over annealing can cause a loss in performance due to the creation of overly large domains and a loss of preferred orientation, illustrating the importance of variable-pressure solvent annealing.

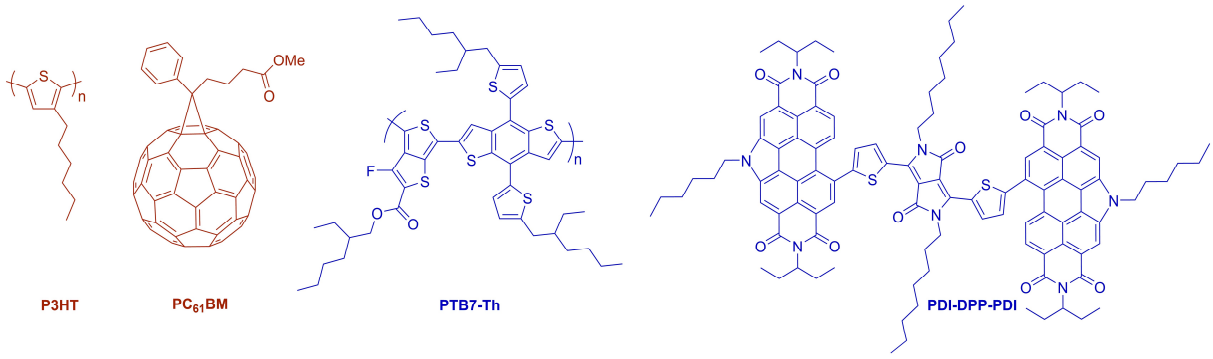

Chart 3.1: Structures of organic photovoltaic active layer materials used in this thesis

3.2. P3HT:$PC_{61}BM$

3.2.1. UV-Visible Spectroscopy

In order to investigate changes in P3HT aggregation during the SVA process, an *in situ* UV/Vis spectroscopy chamber was designed and incorporated into a flow through VP-SVA setup **(Figure 1.8)**. Annealing P3HT induces aggregation which can be seen in the UV/Vis spectrum as absorbance shoulders at 548 nm and 600 nm.[42] Thin films of 1:0.6 w/w P3HT:$PC_{61}BM$ were cast from chloroform to kinetically trap the system in a homogenous disordered morphology, allowing for maximum control over morphology changes. Dry nitrogen was purged over the samples for two minutes and the samples were annealed for 30 minutes followed by a 30 minute drying period where the sample chamber is flushed with dry nitrogen. *In situ* UV/Vis spectra were collected during the annealing process at a rate of one scan every two minutes **(Figure 3.1)**. The spectra of the as cast and annealed films are provided in **Figure 3.2** to illustrate the overall effects of SVA at different chloroform vapour concentrations. The as cast P3HT:$PC_{61}BM$ films show a broad peak with an absorbance maximum at 503 nm and little shouldering at 548 and 600 nm, indicating a low degree of aggregation due to the kinetic trapping of the P3HT chains. During annealing at p/p_{sat} = 0.25 there is a gradual increase of the absorbance and a red shift to 513 nm of the peak maximum **(Figure 3.1** and **Figure 3.2a)**. Additionally, there is a gradual increase in the absorbance

at both 548 and 600 nm during annealing. Upon drying there is immediately a small jump in absorbance for all peaks and the final scan shows more pronounced aggregation shoulders at 548 and 600 nm. When the concentration of chloroform is increased to p/p_{sat} = 0.50 and 0.75, the increase in absorbance and the red shift of the primary absorbance peak occur more quickly, and the absorbance of the aggregation shoulders at 548 and 600 nm increases further **(Figure 3.1b,c** and **Figure 3.2)**. Increasing the chloroform vapour concentration to p/p_{sat} = 0.95 rapidly increases the absorbance of the primary absorbance peak, but to a lesser degree than p/p_{sat} = 0.50 and 0.75 **(Figure 3.1d** and **Figure 3.2)**. At p/p_{sat} = 0.95, the shoulder at 548 nm increases to a lesser degree than films annealed at p/p_{sat} = 0.75, while the shoulder at 600 nm increases to a larger degree relative to p/p_{sat} = 0.75. The changes in absorbance for all films indicate that increasing the annealing vapour pressure of chloroform increases P3HT aggregation.

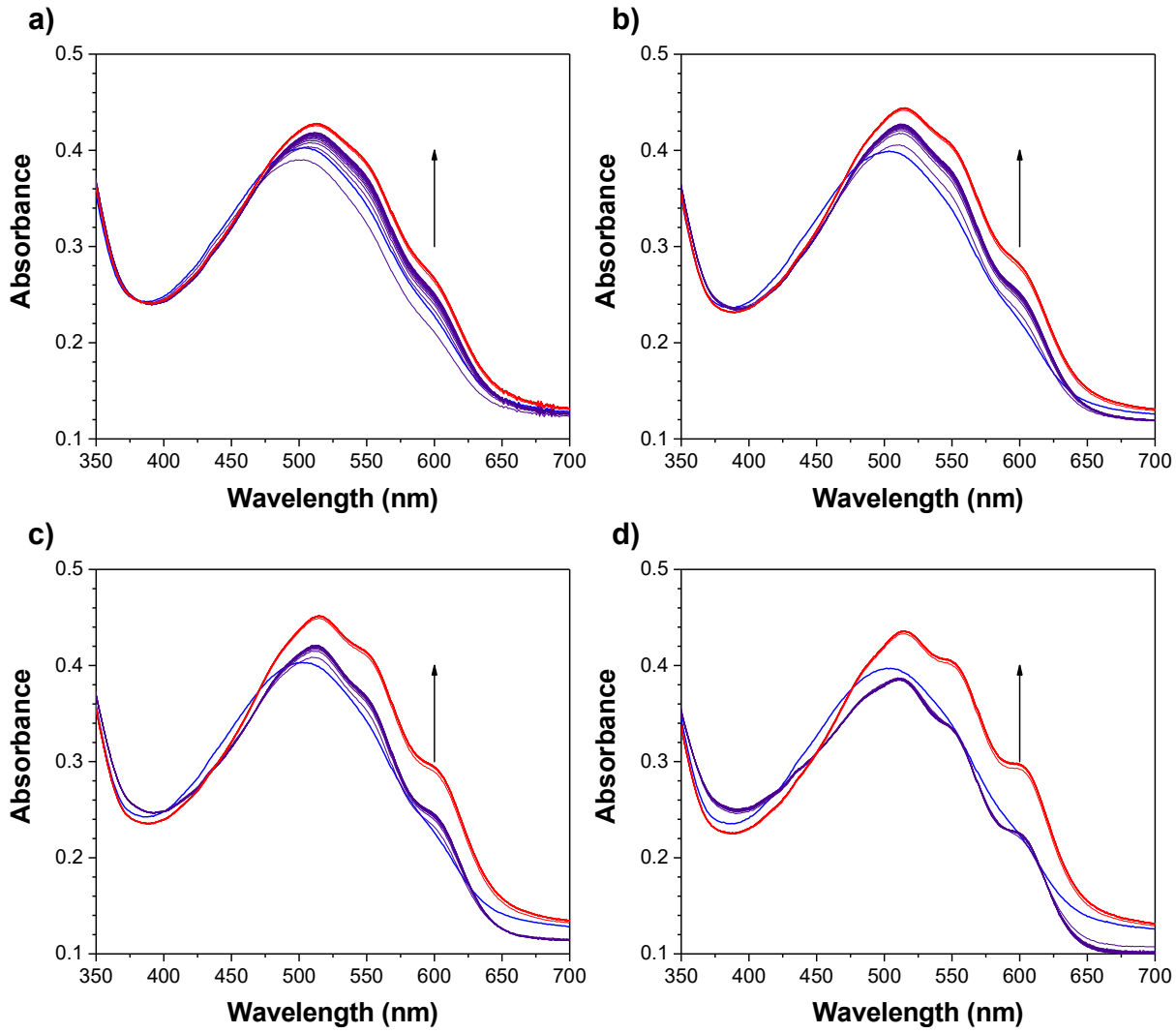

Figure 3.1: *In situ* UV/Vis spectroscopy of 1:0.6 (w/w) P3HT:$PC_{61}BM$ thin films annealed with chloroform vapour concentrations (p/p_{sat}) of: (a) 0.25, (b) 0.50, (c) 0.75, and (d) 0.95. Spectra were acquired at two minute intervals. The direction of change is indicated by arrows. Spectra for the initial (as cast), solvent exposure, and drying stages are shown in blue, purple, and red, respectively.

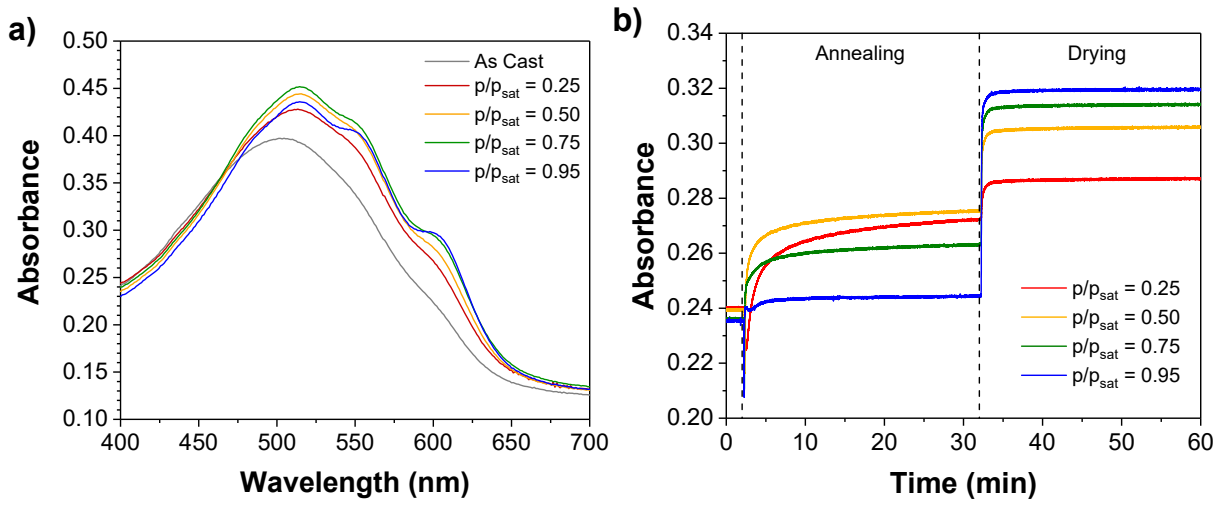

Figure 3.2: (a) Post annealing UV/Vis spectra and (b) absorbance at 600 nm as a function of time for P3HT:$PC_{61}BM$ thin films annealed at various chloroform concentrations.

It is clear from the *in situ* absorbance scans that the P3HT morphology changes rapidly upon the introduction of solvent vapour and information was being lost due to the time limitation of two minutes per scan. To increase the temporal resolution of the UV/Vis measurements, the absorbance of P3HT:$PC_{61}BM$ thin films at 600 nm was measured *in situ* as a function of time during the annealing process **(Figure 3.2)**. Samples were annealed the same as before, where dry nitrogen was flowed over the sample for two minutes to attain a baseline absorbance; chloroform solvent vapour (at various concentrations) was then introduced to the chamber for 30 minutes followed by a dry nitrogen purge for 30 minutes. Within the first minute of introducing chloroform vapour to the sample chamber, a decrease in absorbance was seen for all annealing concentrations indicating a loss in aggregation as the film initially swelled. After the initial swelling, there is an increase in absorbance at 600 nm for all samples indicating an increase in aggregation. At a chloroform vapour concentration of $p/p_{sat} = 0.25$ the absorbance at 600 nm increased throughout the annealing process, indicating that the P3HT chains have low mobility at low chloroform vapour concentrations. A 30 minute annealing time was insufficient for full rearrangement of P3HT into the most thermodynamically stable state. Increasing the chloroform concentration to $p/p_{sat} = 0.50$, 0.75, and

0.95 allows the P3HT chains enough freedom of movement to quickly reach a thermodynamically favored morphology. During annealing, the P3HT aggregation is greatest with p/p_{sat} = 0.50 and decreases as chloroform vapour concentration increases, indicating that increasing the chloroform vapour concentration increases film swelling. Once the solvent is removed, the absorbance at 600 nm of all films increases immediately, indicating the P3HT is aggregating upon drying. The trend shows that increasing chloroform vapour concentration increases the degree of P3HT aggregation. The annealing time appears to be less important than the solvent vapour concentration once at or above p/p_{sat} = 0.50, which should aid in the reproducibility of the process from lab to lab.

3.2.2. Photo-induced Force Microscopy

Film morphology and domain sizes greatly affect device performance in OPVs. AFM and PiFM provide a direct image of film roughness and surface domains respectively. PiFM was used to examine the morphology of P3HT:$PC_{61}BM$ thin films as cast and after annealing at various chloroform vapour concentrations **(Figure 3.3)**. PiFM can directly identify materials in a blend based on their unique IR absorbance.[57,163] A frequency of 810 cm^{-1} **(Figure 3.4)**, corresponding to the out of plane C-H bend in the thiophene ring, was used to image P3HT.[164] For $PC_{61}BM$, a frequency of 1740 cm^{-1} was used, corresponding to the carbonyl stretch on the ester group **(Figure 3.4)**. For the as cast film and the film annealed at p/p_{sat} = 0.25, it is difficult to differentiate domains of P3HT and $PC_{61}BM$ from noise in the PiFM images, indicating that the films are a mostly homogenous blend of P3HT and $PC_{61}BM$. Upon increasing the chloroform vapour concentration to p/p_{sat} = 0.50, domains of phase pure P3HT can be seen in the PiFM image at 810 cm^{-1}; however, the image at 1740 cm^{-1} remains noisy. Increasing the chloroform vapour concentration further to p/p_{sat} = 0.75 induces phase separation in the BHJ blend as evidenced by pure domains of P3HT and $PC_{61}BM$ in the PiFM images. The largest degree of phase separation is seen when the

annealing concentration of chloroform vapour reaches p/p_{sat} = 0.95; large globules of $PC_{61}BM$ form in a P3HT network as the domains increase in size and purity.

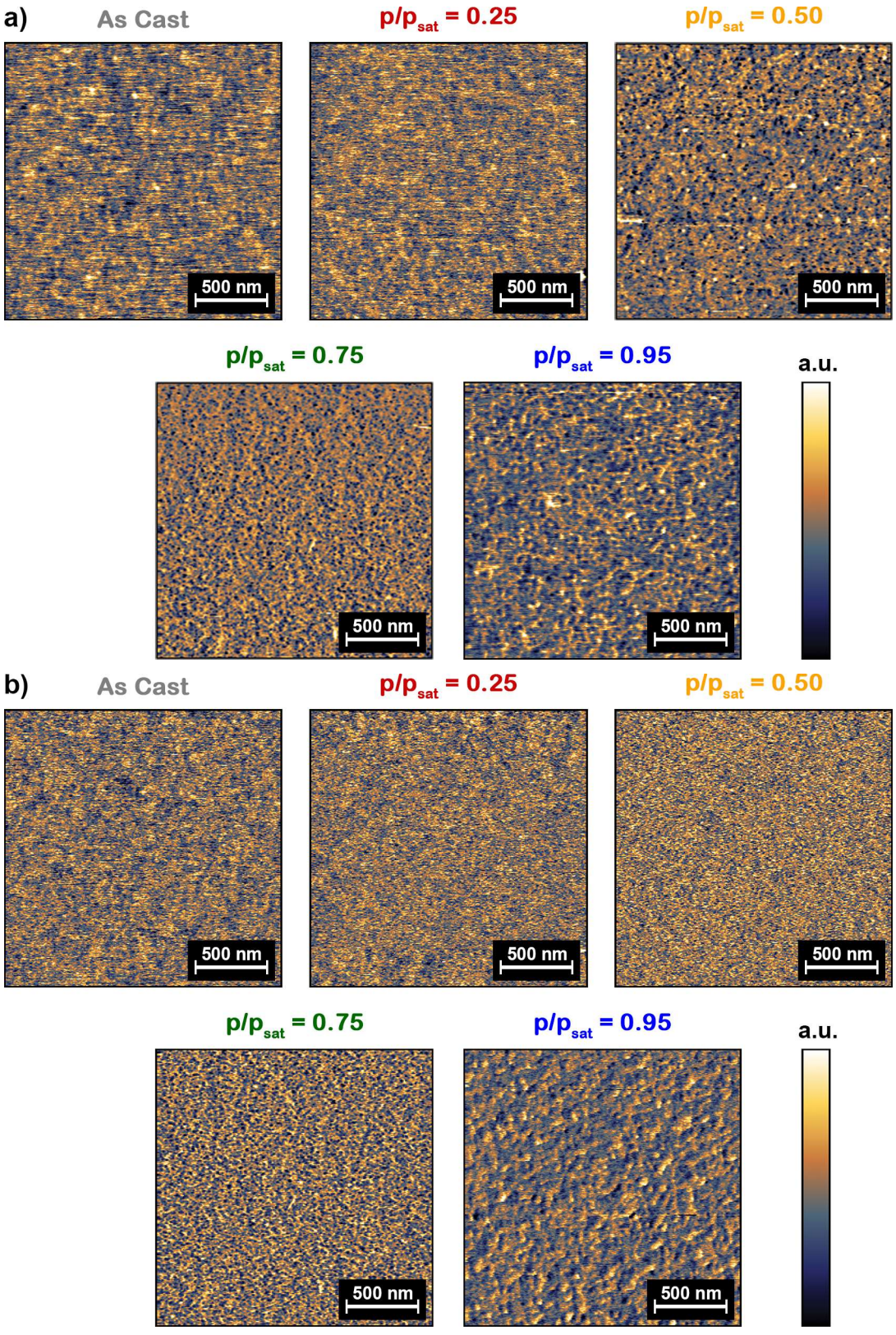

Figure 3.3: PiFM images of P3HT:$PC_{61}BM$ thin films annealed at various chloroform vapour concentrations. Excitation at (a) 810 cm^{-1} and (b) 1740 cm^{-1}.

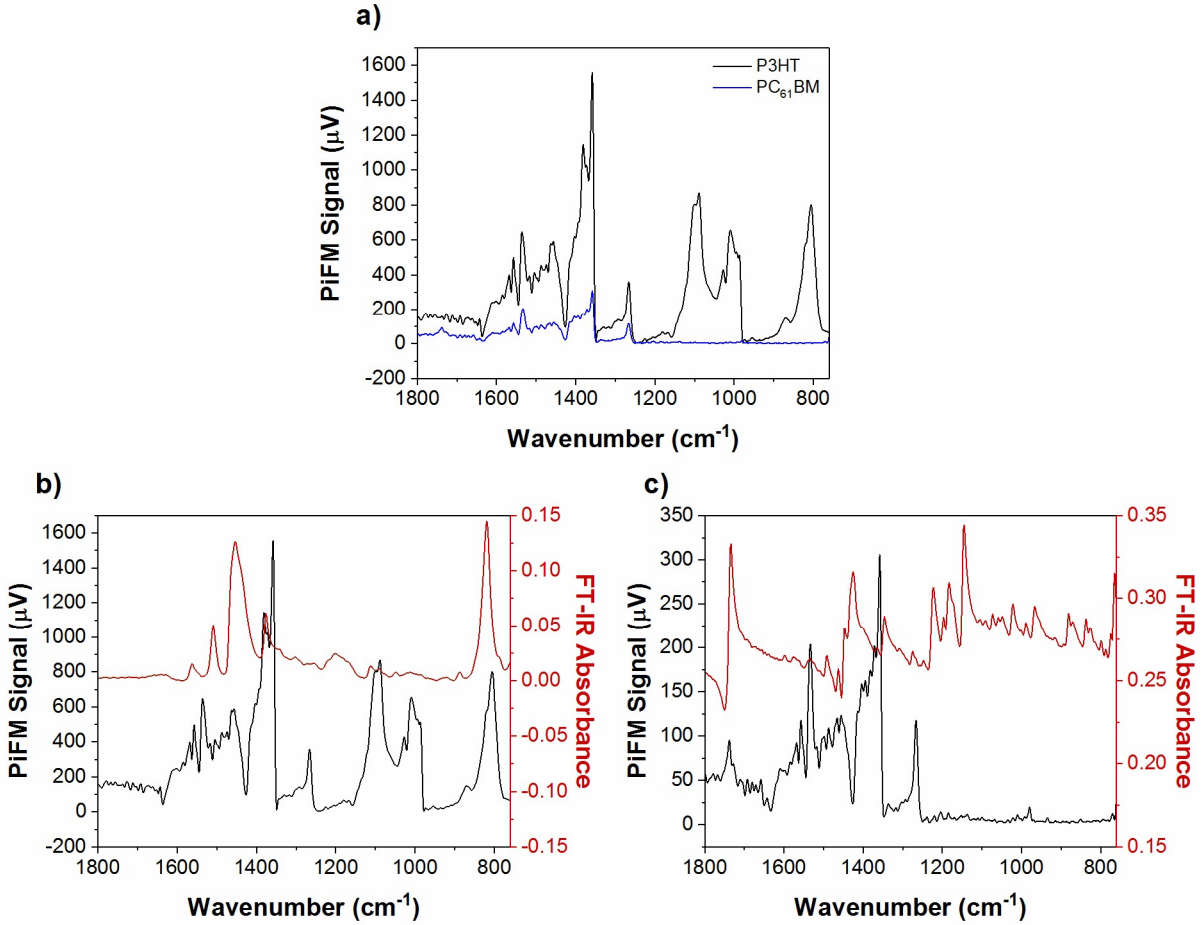

Figure 3.4: (a) PiFM spectra of films of pure P3HT and $PC_{61}BM$. PiFM and ATR-FTIR spectra of pure (b) P3HT and (c) $PC_{61}BM$.

The fast Fourier transform (FFT) of the PiFM images further confirms the trend seen visually in the PiFM images **(Figure 3.5)**. In a FFT image, lower spatial frequencies appear in the center and higher frequencies appear around the edges; this results in larger domains appearing as signals in the central low spatial frequency region of the FFT image, and smaller domains appearing around the edges of the FFT image in the high frequency region. The FFT of the PiFM images for P3HT:$PC_{61}BM$ films as cast and annealed at p/p_{sat} = 0.25 reveal that the images primarily consist of line scan noise as indicated by the large vertical line with equal intensity and spacing. The PiFM FFT of the films annealed at p/p_{sat} = 0.50 show a reduction in noise and larger domains of P3HT

in the 810 cm^{-1} image; however, the image at 1740 cm^{-1} remains largely noise. Once the concentration of chloroform vapour is increased to p/p_{sat} = 0.75 and 0.95, the domains of P3HT and $PC_{61}BM$ become larger and phase separated, indicated by a reduction of line scan noise and the collapse of the FFT signal towards the center of the image.

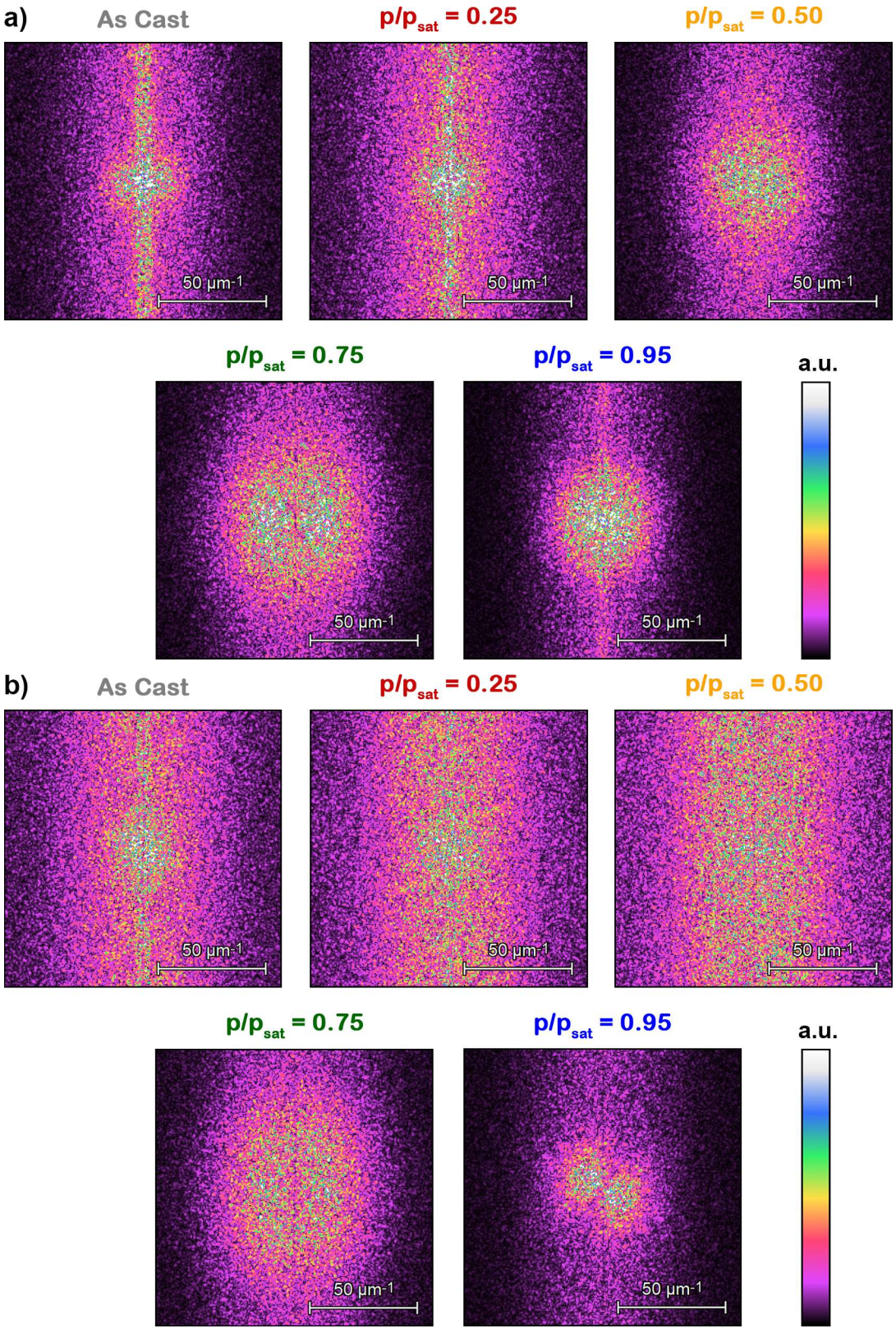

Figure 3.5: FFT of the PiFM signal at (a) 810 cm^{-1} and (b) 1740 cm^{-1} for P3HT:$PC_{61}BM$ thin films annealed at various chloroform concentrations.

Topographic AFM images can be collected in conjunction with PiFM images providing more information about the surface of BHJ samples. The topographies of the as cast film and the films annealed at p/p_{sat} = 0.25 and 0.50 have root mean squared (RMS) surface roughnesses (R_q) of 0.58 nm, 0.68 nm, and 0.56 nm respectively **(Figure 3.6)**. The relatively low surface roughness of these samples validates the homogeneity of the BHJ seen in PiFM. Upon increasing the chloroform concentration to p/p_{sat} = 0.75 and 0.95 there is a large increase in RMS roughness to 0.80 nm and 1.99 nm respectively, which is consistent with the formation of larger discrete domains of P3HT and $PC_{61}BM$ globules, as seen in the PiFM images.

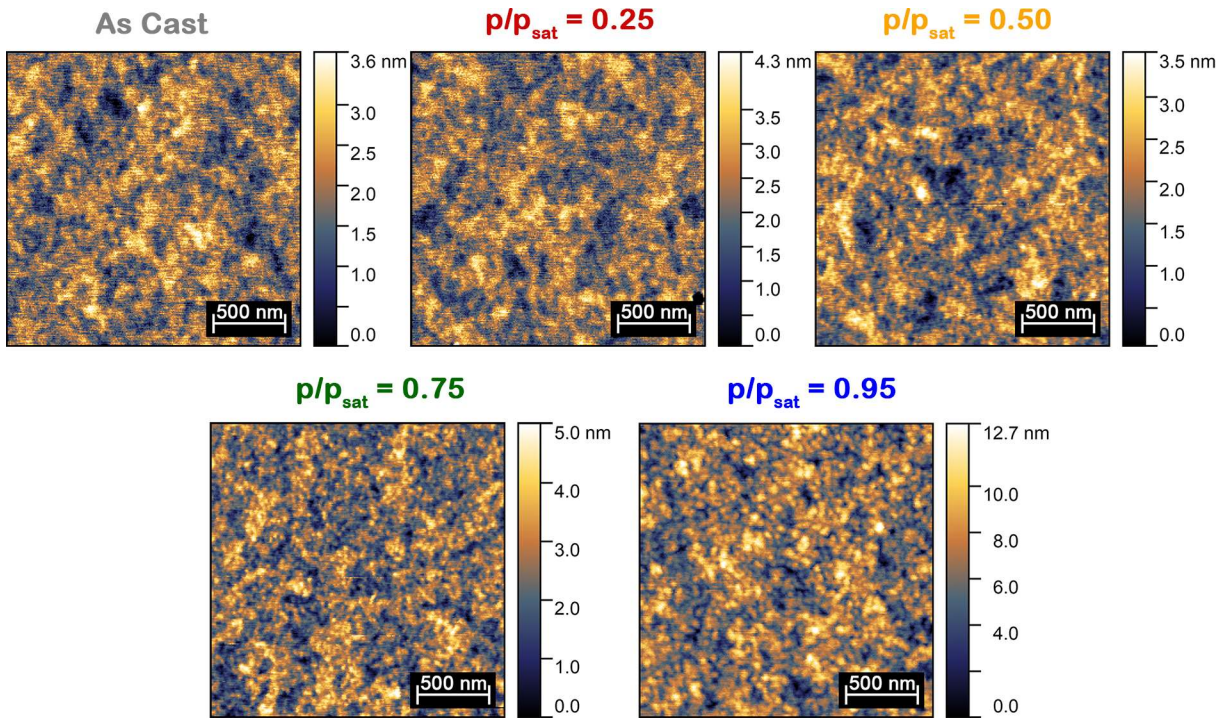

Figure 3.6: AFM topographic images of P3HT:$PC_{61}BM$ thin films annealed at various chloroform concentrations. R_q = 0.58, 0.68, 0.56, 0.80, and 1.99 nm for the as cast film and films annealed at p/p_{sat} = 0.25, 0.50, 0.75, and 0.95, respectively.

3.2.3. Grazing Incidence Wide Angle X-ray Scattering

The crystallinity and orientation of crystallites greatly affect charge transport in OPVs. To examine the effect of VP-SVA on crystallinity, GIWAXS was performed on as cast and annealed films of P3HT:$PC_{61}BM$ **(Figure 3.7)**. The as cast film shows a P3HT (100) peak at q ≈ 0.35 $Å^{-1}$

with higher intensity in the q_r plane indicating preferential face-on orientation as shown in the linecuts along q_r and q_z **(Figure 3.8)**.[43,149] There was also a broad P3HT (010) π-π stacking peak at $q \approx 1.6$ Å^{-1} oriented in the q_z plane further indicating preferred face-on stacking.[43] The broad peak of weakly ordered $PC_{61}BM$ at $q \approx 1.3$ Å^{-1} is mostly isotropic indicating little to no $PC_{61}BM$ preferred orientation.[43]

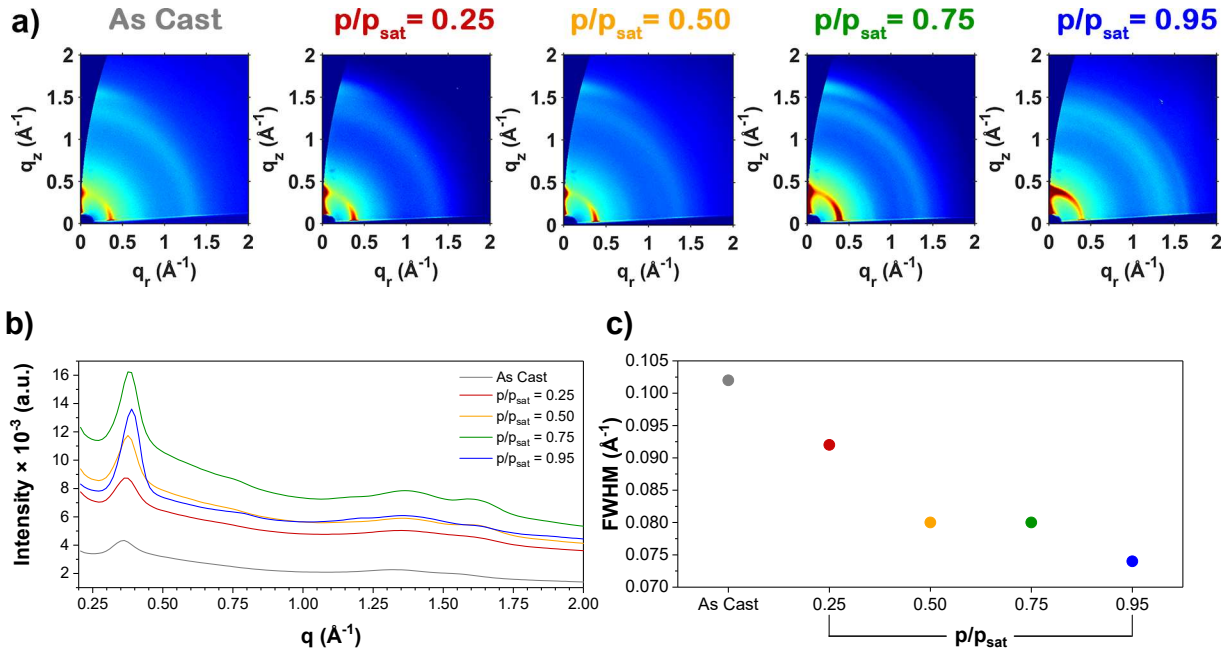

Figure 3.7: (a) GIWAXS patterns of P3HT:$PC_{61}BM$ thin films annealed at various chloroform vapour concentrations. (b) Azimuthally-integrated linecuts (from $\chi = -85°$ to 85°) of the GIWAXS patterns from (a). (c) FWHM of the P3HT (100) peaks after background subtraction.

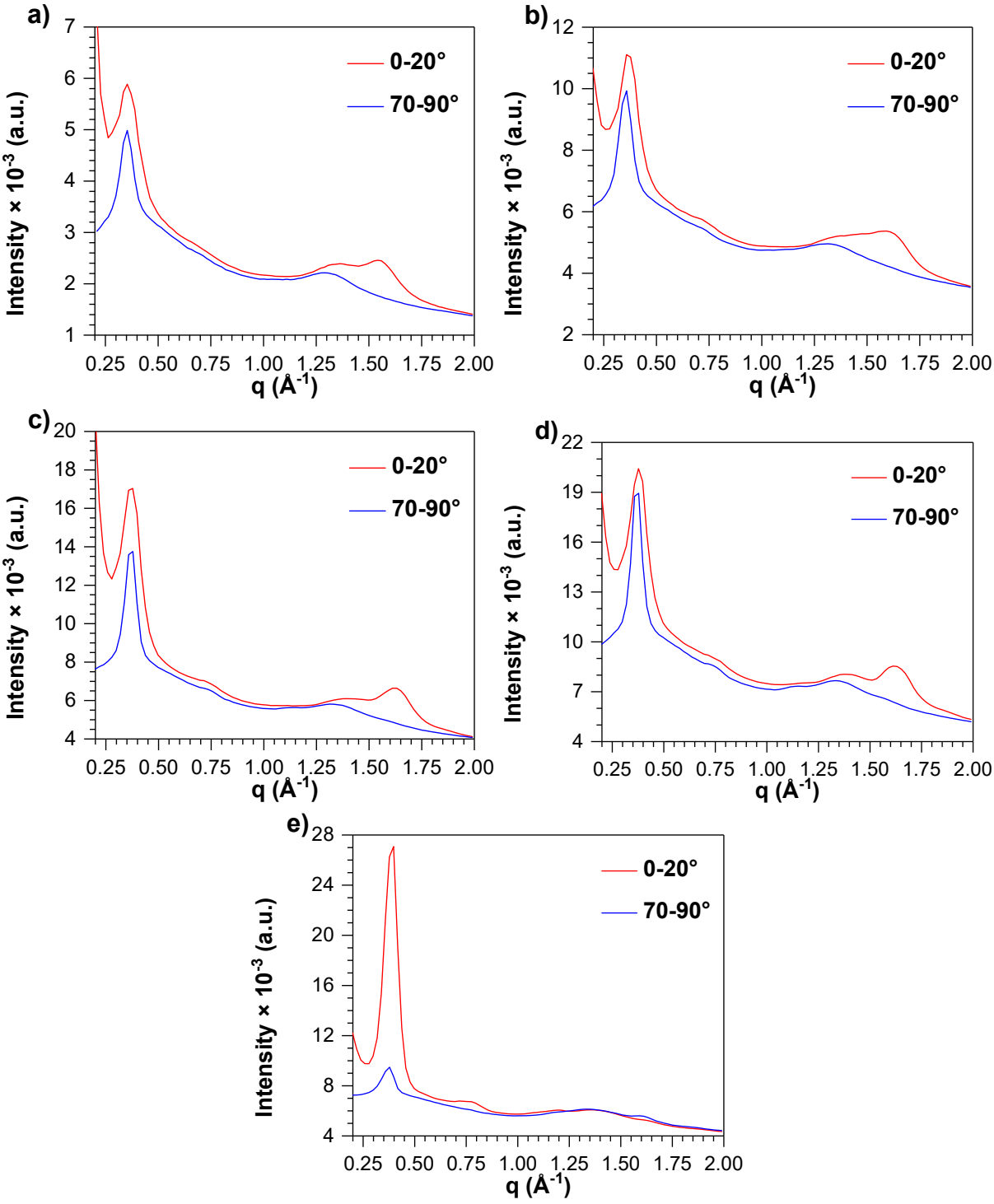

Figure 3.8: GIWAXS linecuts of P3HT:$PC_{61}BM$ thin films, azimuthally-integrated from χ = 0-20° and χ = 70-90°, where χ is the angle between q and q_z. P3HT:$PC_{61}BM$ films were: (a) as cast, and annealed at (b) 0.25, (c) 0.50, (d) 0.75, and (e) 0.95 p/p_{sat}.

The P3HT:$PC_{61}BM$ films annealed at chloroform vapour concentrations of p/p_{sat} = 0.25 and 0.50 show a rapid decrease in the FWHM of the P3HT (100) diffraction peak indicating the size of the crystallites are increasing **(Figure 3.7)**.[141] The exact crystallite size cannot be determined in these experiments due to the large degree of instrumental broadening that arises from the sample geometry; in this thesis the FWHM of diffraction peaks will be used as an approximation to compare the crystallite sizes between similar samples **(Equation 1.5)**. The films annealed at p/p_{sat} = 0.25 and 0.50 still show a high degree of face-on orientation in P3HT and higher order (200) peaks begin to appear at $q \approx 0.71$ $Å^{-1}$ **(Figure 3.8)**. As the concentration of annealing chloroform vapour is increased to p/p_{sat} = 0.75, there is little change in the FWHM of the P3HT (100) peak; however, the appearance of a higher order P3HT (300) peak at $q \approx 1.13$ $Å^{-1}$ indicates further crystallization as the material becomes more ordered. At p/p_{sat} = 0.95, the FWHM of the P3HT (100) peak decreases further and higher order (200) and (300) peaks are present, indicating larger P3HT crystallites and an overall larger degree of crystallinity than the less annealed samples. Additionally, there is an increase in the intensity of the (100), (200), and (300) P3HT peaks along the q_z axis, and the orthogonal (010) peak intensity orients more towards the q_r axis, indicating a change to predominantly edge-on morphology in P3HT **(Figure 3.8)**. The $PC_{61}BM$ peak remains relatively isotropic throughout the annealing process, regardless of chloroform vapour concentration.

3.2.4. Device Performance

P3HT:$PC_{61}BM$ devices were fabricated to correlate the effects of morphological changes to device performance. Devices were cast from chloroform, and annealed at various chloroform vapour concentrations. As cast P3HT:$PC_{61}BM$ devices had a relatively low PCE of 1.6 ± 0.1% **(Figure 3.9)**. Upon annealing with chloroform vapour at p/p_{sat} = 0.25, the device efficiency

increased to 2.4 ± 0.2%. The increase in efficiency can be attributed to an increase in J_{SC} and a decrease in R_S resulting in a higher FF **(Table 3.1)**. A small loss in V_{OC} also occurred **(Figure 3.9)**. The decrease in R_S and increase in J_{SC} are probably caused by an increase in P3HT charge carrier mobility. Increasing P3HT aggregation and crystallinity leads to an increase in interchain P3HT π-π orbital overlap; this has been shown to increase carrier mobility.[73] As the chloroform vapour concentration was increased to p/p_{sat} = 0.50 and 0.75, the PCE of the devices increased to 2.6 ± 0.2% and 2.9 ± 0.2%, respectively. The PCE increases can again be attributed to increases in J_{SC} and decreases in R_S as the films aggregated further and began to phase separate, thus increasing P3HT hole transport and the number of continuous charge transport pathways to the electrodes. The PCE dropped to 2.7 ± 0.2% for devices annealed at p/p_{sat} = 0.95. The drop in PCE is caused primarily by a drop in the J_{SC}, while FF, V_{OC}, and R_S remain similar. Geminate recombination due to overly large domains, and a decrease in charge transport are likely causes of lost efficiency.

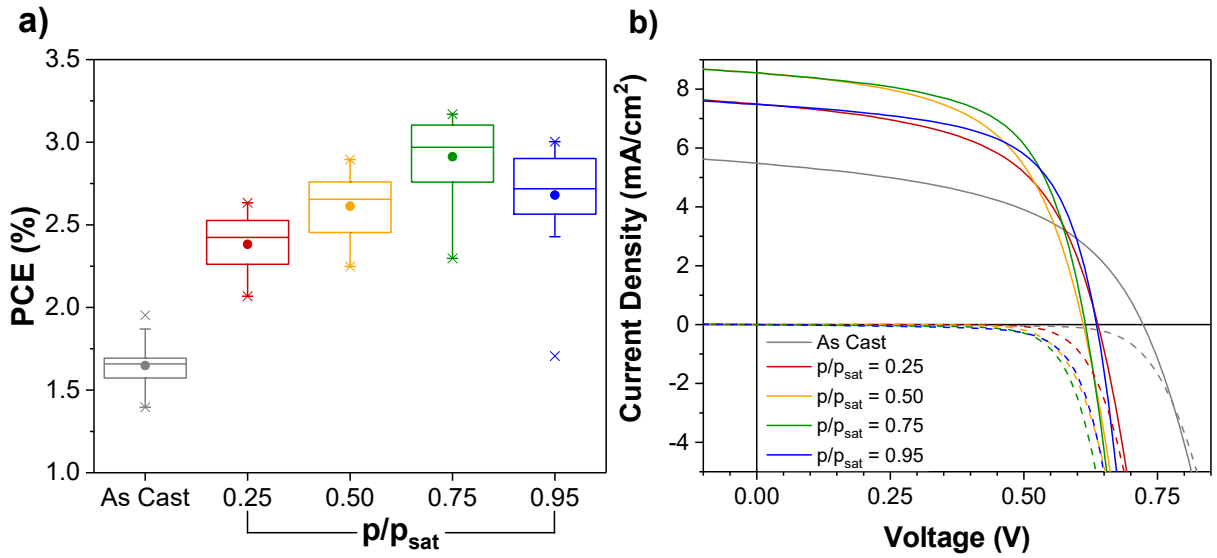

Figure 3.9: (a) Power conversion efficiency of P3HT:$PC_{61}BM$ devices annealed at various chloroform concentrations. The dots represent mean values, and the central lines the medians. The box defines the 25th and 75th percentiles, while the bars define the 5th and 95th percentiles. The maximum and minimum PCE values are each denoted by an ×. Device statistics were derived from measurements on a minimum of 27 devices (8 devices per substrate). (b) J-V curves in the light (solid) and the dark (dashed) for the highest performing P3HT:$PC_{61}BM$ devices annealed at various chloroform concentrations.

In OPVs, charge carriers must travel perpendicular to the substrate to be collected at the electrodes. The as cast film and the films annealed at p/p_{sat} = 0.25, 0.50, and 0.75 show predominantly face on P3HT orientation **(Figure 1.*14*** and **Figure 3.7)**; however, the film annealed at p/p_{sat} = 0.95 shows P3HT stacking predominantly in edge on orientation. The decrease in photocurrent in the p/p_{sat} = 0.95 devices could be a result of reduced hole mobility normal to the substrate due to the edge on orientation of the P3HT (where the π-π stacking direction is parallel to the substrate).[43] Further loss of photocurrent may be the result of larger domain sizes of both P3HT and $PC_{61}BM$. Larger domains could lead to increased geminate recombination as the bound excitons cannot migrate to a donor-acceptor interface within their lifetime.[21]

Table 3.1: Device performance parameters for P3HT:$PC_{61}BM$ devices annealed at various chloroform vapour concentrations.

Annealing Condition	N	V_{oc} (V)	J_{sc} [a] (mA·cm^{-2})	Fill Factor (%)	PCE [a] (%)	R_S [b] (Ω·cm^2)	$R_{Sh} \times 10^{-2}$ [b] (Ω·cm^2)
As Cast	32	0.726 ± 0.007	5.0 ± 0.3	45 ± 2	1.6 ± 0.1	41 ± 5	6.9 ± 0.7
p/p_{sat} = 0.25	31	0.642 ± 0.007	7.1 ± 0.3	52 ± 2	2.4 ± 0.2	22 ± 3	6.6 ± 0.6
p/p_{sat} = 0.50	32	0.607 ± 0.008	8.1 ± 0.4	53 ± 2	2.6 ± 0.2	18 ± 2	6 ± 1
p/p_{sat} = 0.75	30	0.609 ± 0.008	8.3 ± 0.4	57 ± 2	2.9 ± 0.2	14 ± 2	7.8 ± 0.7
p/p_{sat} = 0.95	27	0.626 ± 0.008	7.6 ± 0.4	58 ± 2	2.7 ± 0.2	14 ± 2	9 ± 1

[a] J_{sc} and PCE were calculated using the apertured device area (0.0708 cm^2). [b] Resistances were calculated based on the slope at V_{oc} and J_{sc} and the non-apertured device area (0.085 cm^2).

3.3. PTB7-Th:PDI-DPP-PDI

3.3.1. UV-Visible Spectroscopy

After successfully using the flow through VP-SVA system to control the morphology of the P3HT:$PC_{61}BM$ BHJ system, we examined a representative modern NFA system, PTB7-Th:PDI-DPP-PDI. This system was chosen because it was shown to increase efficiency with SVA, but was also susceptible to over annealing, illustrating the need for control over the annealing process.[78]

Since PTB7-Th and PDI-DPP-PDI are less studied than P3HT:$PC_{61}BM$, the neat materials were examined to gain insight into the effects of annealing on a less complicated system. Films of neat PDI-DPP-PDI were annealed at various chloroform concentrations and examined by UV/Vis spectroscopy **(Figure 3.10)**. The as cast film shows a broad absorbance centered around 642 nm involving the DPP core and two sharp absorbance peaks at 532 nm and 501 nm from the PDI terminal units.[78] Annealing at p/p_{sat} = 0.25 and 0.50 produced little change in the absorbance spectra. Increasing the chloroform vapour concentration to p/p_{sat} = 0.75 induced major changes to the absorbance spectrum; the PDI peak at 501 nm decreased in intensity greatly, the PDI peak at 532 nm red shifted to 539 nm and decreased in intensity, the broad DPP peak at 642 nm

disappeared, and a new DPP peak grew in at 579 nm. In a previous report by Payne et al. the changes in the UV/Vis absorbance spectrum of PDI-DPP-PDI were attributed to a rearrangement of the DPP core.[165] When the annealing chloroform vapour concentration was increased further to p/p_{sat} = 0.95, similar spectral changes occurred as at p/p_{sat} = 0.75, but to a greater degree. Neat PTB7-Th has absorbance peaks in the UV/Vis spectrum at 642 and 699 nm which undergo little change when annealed with chloroform at all concentrations **(Figure 3.11)**.

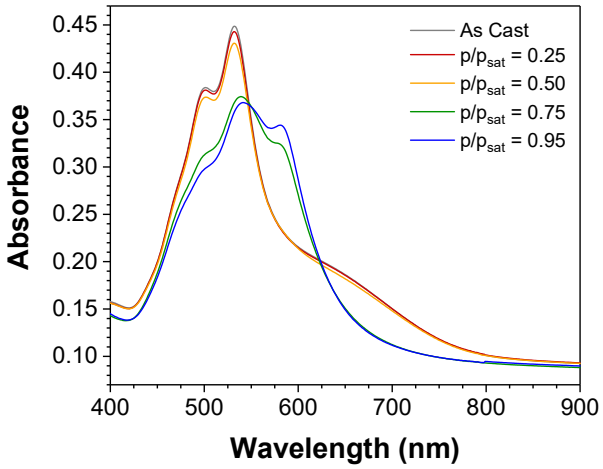

Figure 3.10: UV/Vis spectra of neat PDI-DPP-PDI thin films annealed at various chloroform concentrations.

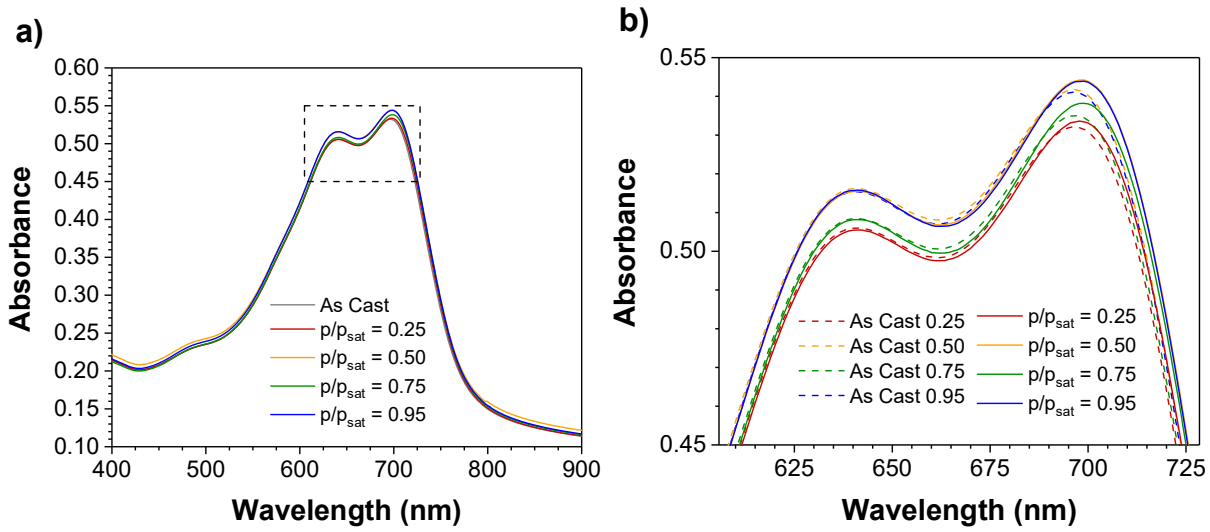

Figure 3.11: UV/Vis spectra of neat PTB7-Th thin films annealed at various chloroform concentrations: (a) full range and (b) expanded view. The expanded view of the absorption band shows that the small changes are not due to differences in solvent vapour concentration, but are primarily the result of variability in film thickness.

BHJ blend films of 1:1.5 w/w PTB7-Th:PDI-DPP-PDI were annealed at various chloroform concentrations and examined by UV/Vis spectroscopy **(Figure 3.12)**. The absorbance of the as cast blend is a superimposition of the spectra of the neat materials. PDI peaks remain at 500 and 531 nm and the absorbance peaks of PTB7-Th (642 and 699 nm) overlap with the broad DPP peak at 642 nm. The blend behaves similarly to the neat materials, with little overall change occurring after VP-SVA at low chloroform vapour concentrations (p/p_{sat} = 0.25, and 0.50). In the *in situ* VP-SVA experiments, a small decrease in the DPP absorbance can be seen during annealing (indicating swelling of the film) with slightly higher swelling for the p/p_{sat} = 0.50 film than the p/p_{sat} = 0.25 film **(Figure 3.13)**. At p/p_{sat} = 0.75 a large change in the absorbance profile occurred, similar to neat PDI-DPP-PDI. During annealing, there was a large decrease in absorbance in the region from 640 nm to 695 nm that is probably due to the loss of the broad DPP peak at 642 nm **(Figure 3.13)**; this change was seen in the neat PDI-DPP-PDI, but not in the neat PTB7-Th. Additionally, the absorbance of PDI at 500 nm decreases dramatically, and the absorbance originally at 530 nm decreases and red shifts to 537 nm. A new peak at 583 nm grows in indicating

a rearrangement of the DPP core in PDI-DPP-PDI is also present in the BHJ blends.[78] Upon annealing at p/p_{sat} = 0.95 the annealing effects are again similar to p/p_{sat} = 0.75 but occur to a greater extent.

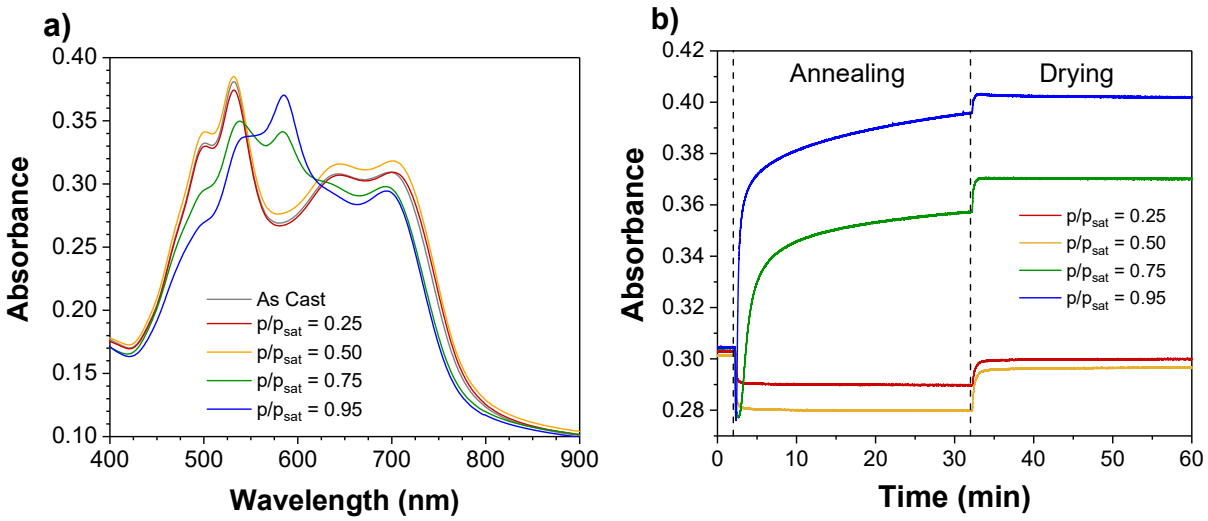

Figure 3.12: (a) Post-annealing UV/Vis spectra and (b) absorbance at 584 nm as a function of time for PTB7-Th:PDI-DPP-PDI thin films annealed at various chloroform vapour concentrations.

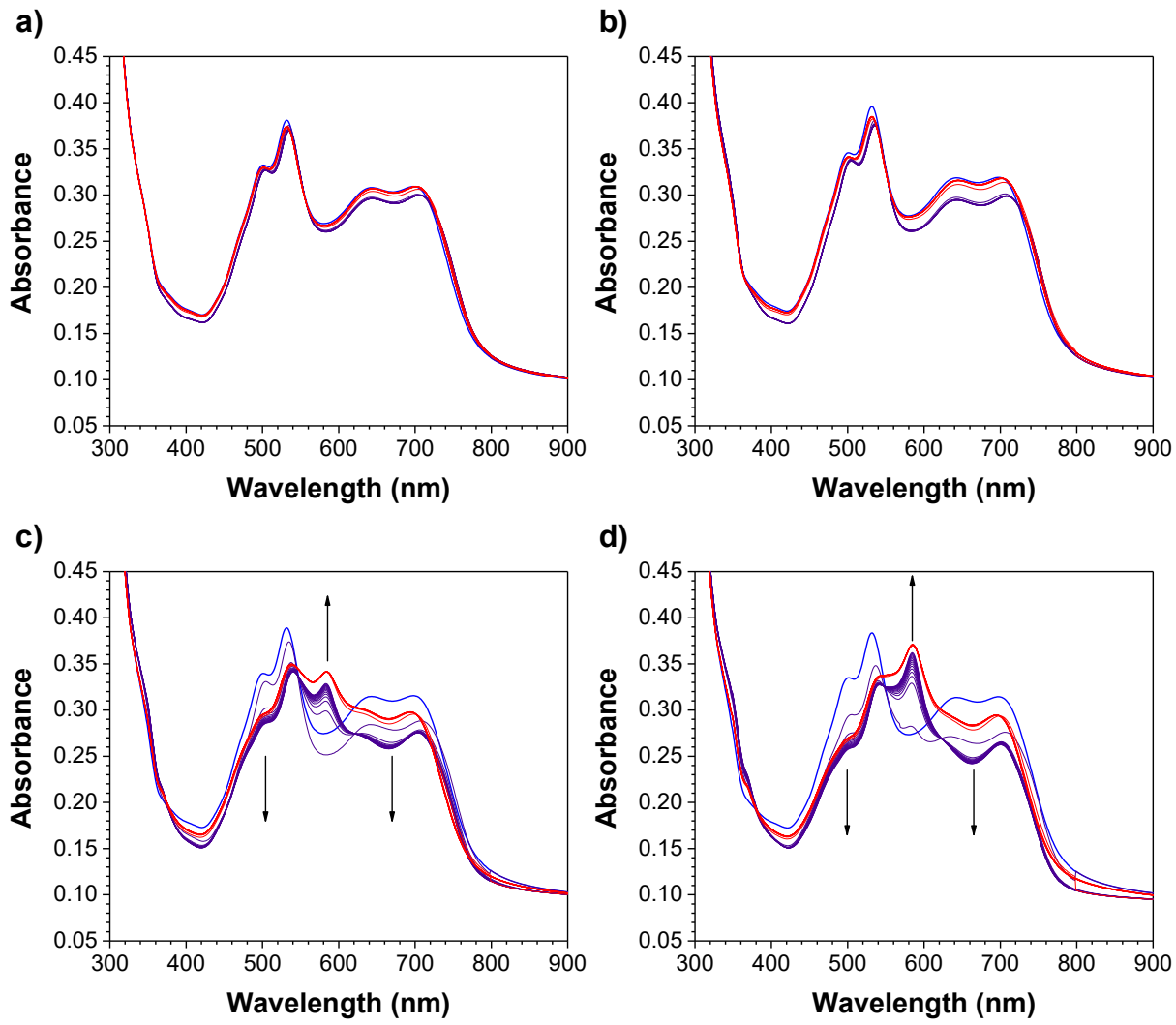

Figure 3.13: *In situ* UV/Vis spectroscopy of PTB7-Th:PDI-DPP-PDI thin films annealed with chloroform vapour concentrations (p/p_{sat}) of: (a) 0.25, (b) 0.50, (c) 0.75, and (d) 0.95. Spectra were acquired at two minute intervals. The direction of change is indicated by arrows. Spectra for the initial (as cast), solvent exposure, and drying stages are shown in blue, purple, and red, respectively.

The absorbance of PTB7-Th:PDI-DPP-PDI BHJ films was measured *in situ* at 584 nm over the annealing process to watch the growth of the new DPP stacking motif. The samples were subjected to a flow of dry nitrogen for two minutes to obtain a background absorbance, then chloroform vapour was introduced to the annealing chamber at various concentrations for 30 minutes followed by a 30 minute drying period. As with the P3HT:$PC_{61}BM$ samples, there is a

decrease in absorbance within the first 60 seconds of SVA as the films swell and DPP stacking decreases. At a solvent vapour concentration of p/p_{sat} = 0.25 and 0.50 the films remain swollen for the duration of the annealing and return to their original absorbance once the films are dry. Increasing the annealing concentration to p/p_{sat} = 0.75 induces major changes in the *in situ* absorbance profile. There is an increase in absorbance at 584 nm during annealing and the absorbance profile does not plateau indicating that increased annealing time would likely result in increased absorbance. Upon drying, the absorbance at 584 nm increases further indicating that the film de-swells and the DPP orients to the new orientation. As the concentration of chloroform vapour is increased to p/p_{sat} = 0.95 the growth of the absorbance at 584 nm increases rapidly during annealing, and there is an increase in absorbance immediately upon drying. The final absorbance at p/p_{sat} = 0.95 is higher than all other annealing concentrations, indicating an increased level of DPP rearrangement as the chloroform vapour concentration is increased.

3.3.2. Photo-induced Force Microscopy

To investigate the effect of SVA on the domain sizes and phase separation of the PTB7-Th:PDI-DPP-PDI BHJ blend, PiFM images were taken of BHJ films annealed at various chloroform vapour concentrations **(Figure 3.14)**. Due to the lack of a unique IR signal from PTB7-Th in the range of 800 cm^{-1} to 1800 cm^{-1} (the effective range of the quantum cascade laser), the only unique PiFM signal that can be used is the carbonyl stretch in PDI-DPP-PDI at 1694 cm^{-1} **(Figure 3.15)**. The PiFM at 1694 cm^{-1} of the as cast blend shows an intimate mixture of PTB7-Th and PDI-DPP-PDI as the phases can barely be distinguished from the noise. Upon annealing with chloroform vapour at p/p_{sat} = 0.25 and 0.50 the domain sizes of PDI-DPP-PDI remain small. Consistent with the UV/Vis spectra, there is a large change in surface morphology upon annealing at a chloroform vapour concentration of p/p_{sat} = 0.75. The domain sizes of PDI-DPP-PDI grow

visibly larger and areas lacking PDI-DPP-PDI (presumably areas with higher concentrations of PTB7-Th) appear in the PiFM image. Increasing the chloroform vapour concentration further to p/p_{sat} = 0.95 increases the domain sizes dramatically.

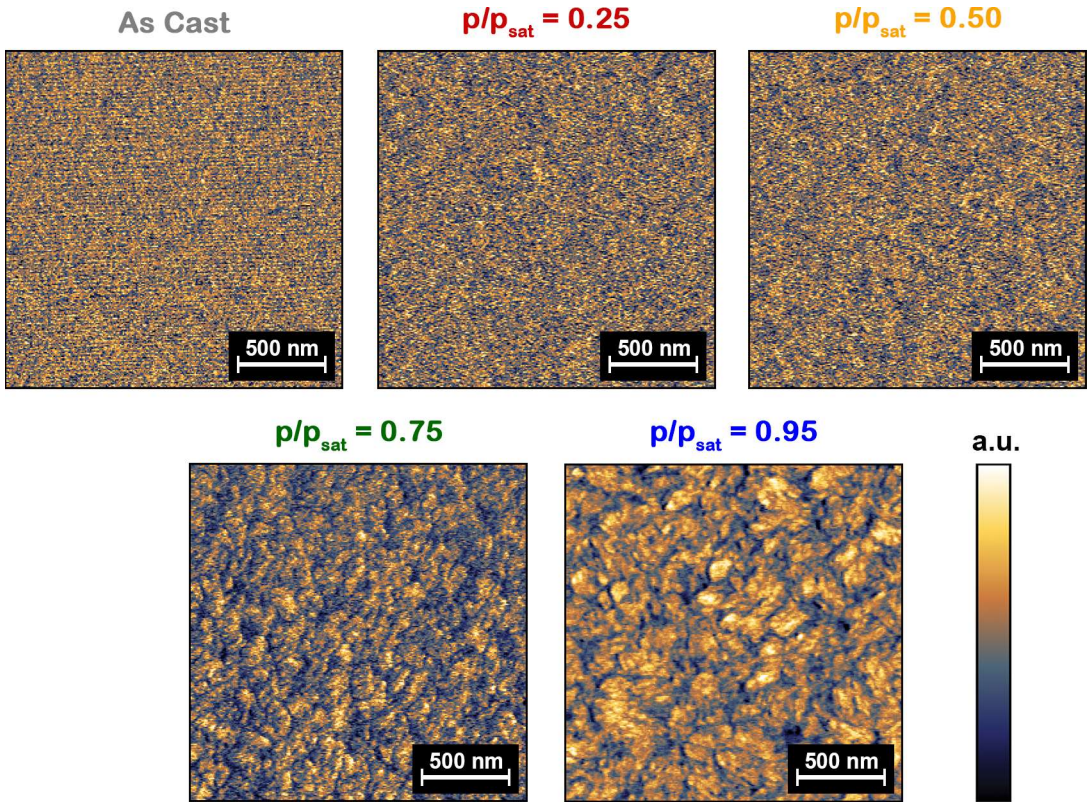

Figure 3.14: PiFM images of PTB7-Th:PDI-DPP-PDI thin films annealed at various chloroform vapour concentrations. Excitation at 1694 cm^{-1}.

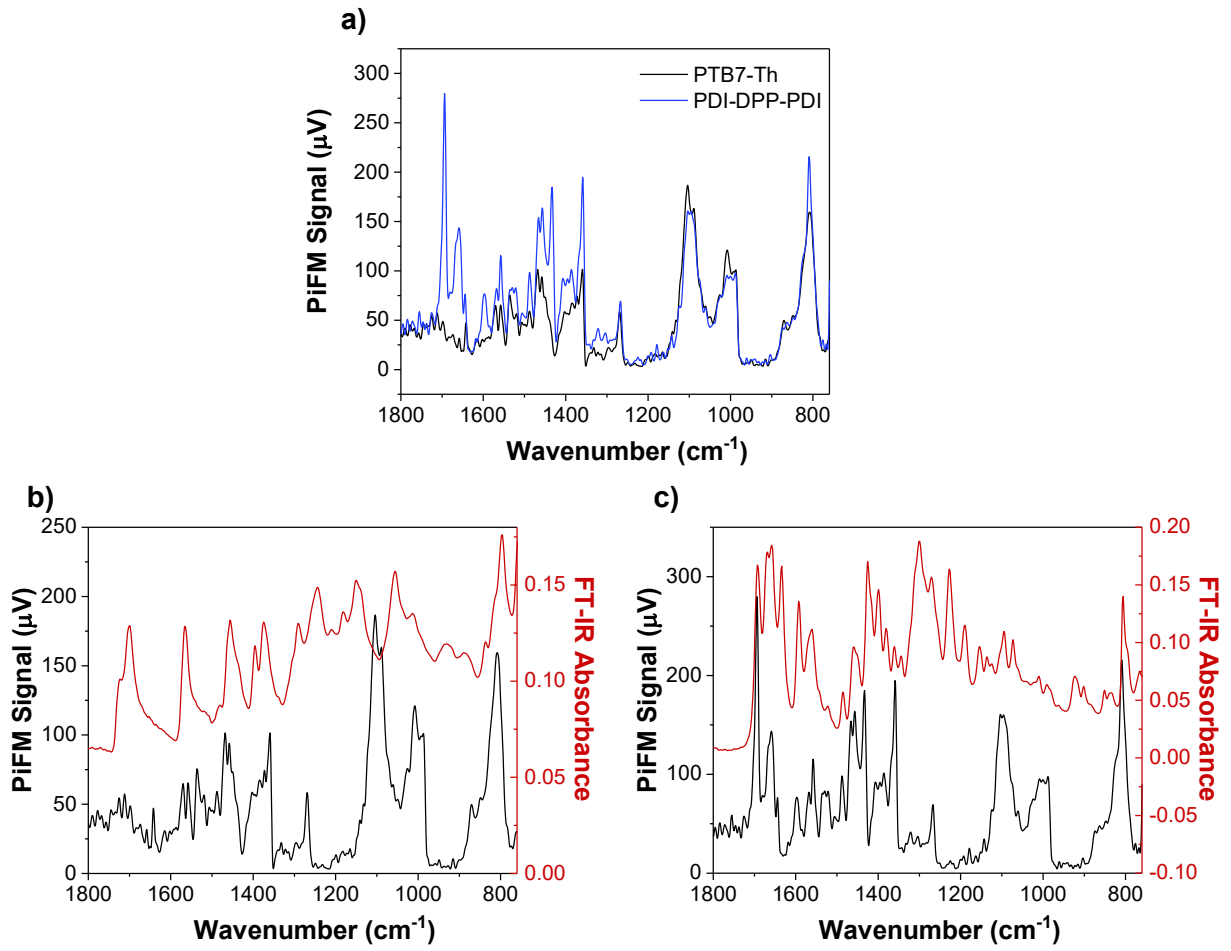

Figure 3.15: (a) PiFM spectra of films of pure PTB7-Th and PDI-DPP-PDI. PiFM and ATR-FTIR spectra of pure (b) PTB7-Th and (c) PDI-DPP-PDI.

The FFT of the PiFM images were used to examine trends in size distribution of the domains of PDI-DPP-PDI **(Figure 3.16)**. The as cast film and films annealed at $p/p_{sat} = 0.25$ and 0.50 show a broad distribution of domain sizes and a slight amount of line scan noise. As the chloroform concentration is increased to $p/p_{sat} = 0.75$, the distribution of domain sizes decreases and converges towards the low frequency region of the FFT image (indicating larger material domains); however, line scan noise is still present. Increasing the chloroform concentration to $p/p_{sat} = 0.95$ further concentrates the distribution of domain sizes towards the low frequency region of the FFT with a small amount of line scan noise.

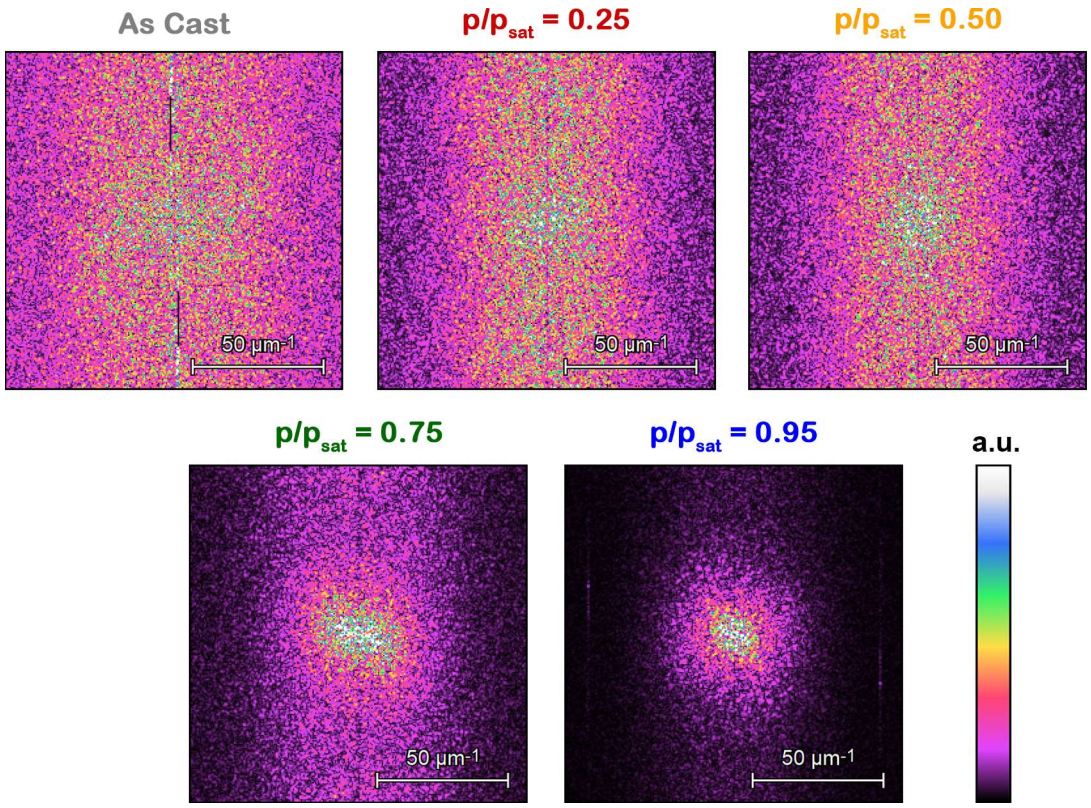

Figure 3.16: FFT of the PiFM signal at 1694 cm^{-1} for PTB7-Th:PDI-DPP-PDI thin films annealed at various chloroform concentrations.

AFM topography images of PDI-DPP-PDI were collected simultaneously with the PiFM images **(Figure 3.17)**. The topography for the as cast film is moderately rough (RMS roughness 0.96 nm) when compared to P3HT:$PC_{61}BM$ samples. For the films annealed at p/p_{sat} = 0.25 and 0.50 there was a slight decrease in surface roughness (0.61 nm and 0.58 nm respectively); the swelling and deswelling of the films during annealing may have had a smoothing effect on the surface. There is a large jump in surface roughness for films annealed at p/p_{sat} = 0.75 and 0.95 (1.49 nm and 2.31 nm respectively), which supports the conclusion that domain sizes increase significantly once a chloroform vapour concentration threshold of p/p_{sat} = 0.75 is reached.

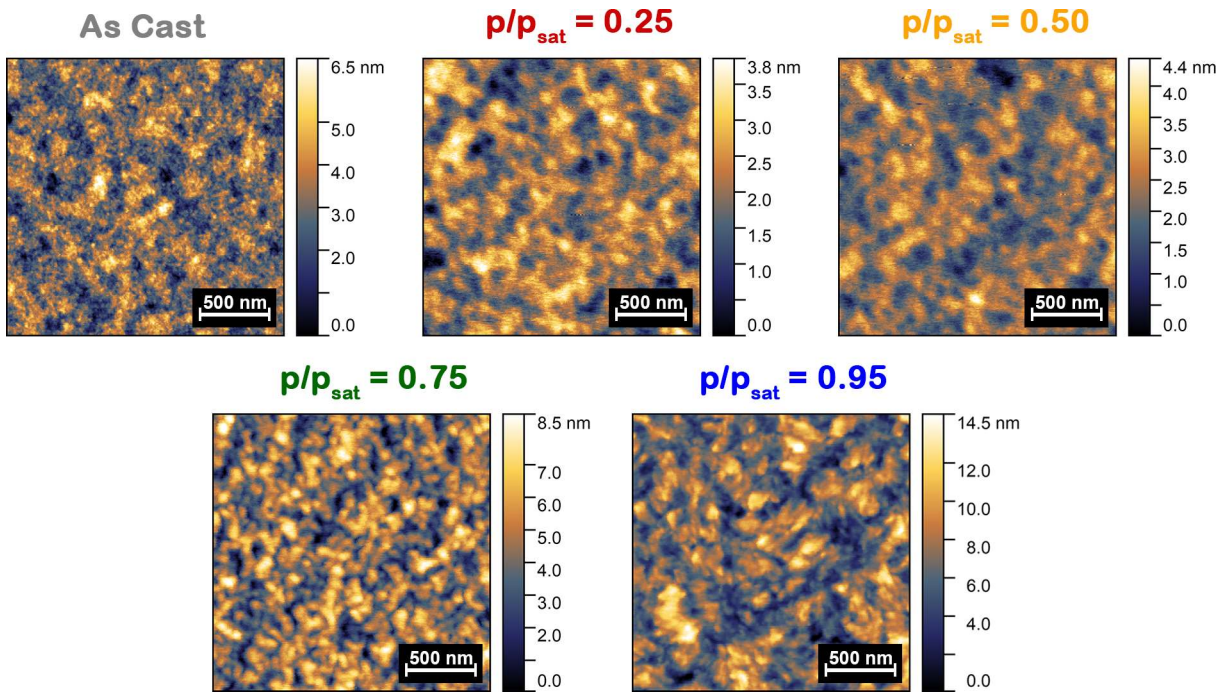

Figure 3.17: AFM topographic images of PTB7-Th:PDI-DPP-PDI thin films annealed at various chloroform concentrations. R_q = 0.96, 0.61, 0.58, 1.49, and 2.31 nm for the as cast film and films annealed at p/p_{sat} = 0.25, 0.50, 0.75, and 0.95, respectively.

3.3.3. Grazing Incidence Wide Angle X-ray Scattering

Thin film GIWAXS patterns of neat PTB7-Th and neat PDI-DPP-PDI were collected (as cast and annealed) to gain insight into the crystalline morphology of the neat materials **(Figure 3.18** and **Figure 3.19** respectively**)**. The as cast PTB7-Th film has a (100) lamellar peak at q ≈ 0.26 $Å^{-1}$ oriented along q_r and a (010) π stacking peak at q ≈ 1.59 $Å^{-1}$ oriented along q_z, indicating face on orientation.[166] The orientation of PTB7-Th remained face on for all annealing concentrations. The as cast PDI-DPP-PDI film has diffraction peaks centered around q ≈ 0.38 $Å^{-1}$ and 1.7 $Å^{-1}$ **(Figure 3.19** and **Figure 3.20)**. The peaks are broad and mostly isotropic, indicating an isotropic orientation of weakly ordered material. As PDI-DPP-PDI is annealed at p/p_{sat} = 0.25 there is little change in the GIWAXS pattern or the FWHM of the peak at q ≈ 0.38 $Å^{-1}$. When the chloroform vapour concentration is increased to p/p_{sat} = 0.50 the peak at q ≈ 0.38 $Å^{-1}$ resolves into 3 peaks at q ≈ 0.32 $Å^{-1}$, 0.46 $Å^{-1}$, and 0.66 $Å^{-1}$ indicating an increase in sample crystallinity (best

observed in the linecut along q_z in **Figure 3.20**). The FWHM of the stacking peak at $q \approx 0.32$ Å^{-1} decreases relative to the broad peak at $q \approx 0.38$ Å^{-1} seen in the as cast and $p/p_{sat} = 0.25$ GIWAXS patterns. The exact degree of crystallite growth is difficult to ascertain because the peak in the unannealed sample was likely an overlap of three different peaks, artificially lowering crystallite sizes calculated by the Scherrer equation **(Equation 1.5)**. Slight preferred orientation of the peak at $q \approx 0.32$ Å^{-1} occurs towards the q_z axis, indicating this plane prefers to orient parallel to the substrate **(Figure 3.20)**. An increase in chloroform concentration to $p/p_{sat} = 0.75$ results in an increase in preferred orientation and a further increase in crystallite size as the FWHM of the peak at $q \approx 0.32$ Å^{-1} decreases. Additionally, a new peak at $q \approx 0.60$ Å^{-1} can be resolved and shows preferred orientation. Finally, upon annealing at $p/p_{sat} = 0.95$, the preferred orientation increases in the peaks at $q \approx 0.34$ Å^{-1} and 0.75 Å^{-1} parallel to the substrate. The broad π-π stacking peak breaks into two peaks around $q \approx 1.5$ Å^{-1} and 1.7 Å^{-1}. These peaks are preferentially oriented parallel to the substrate.

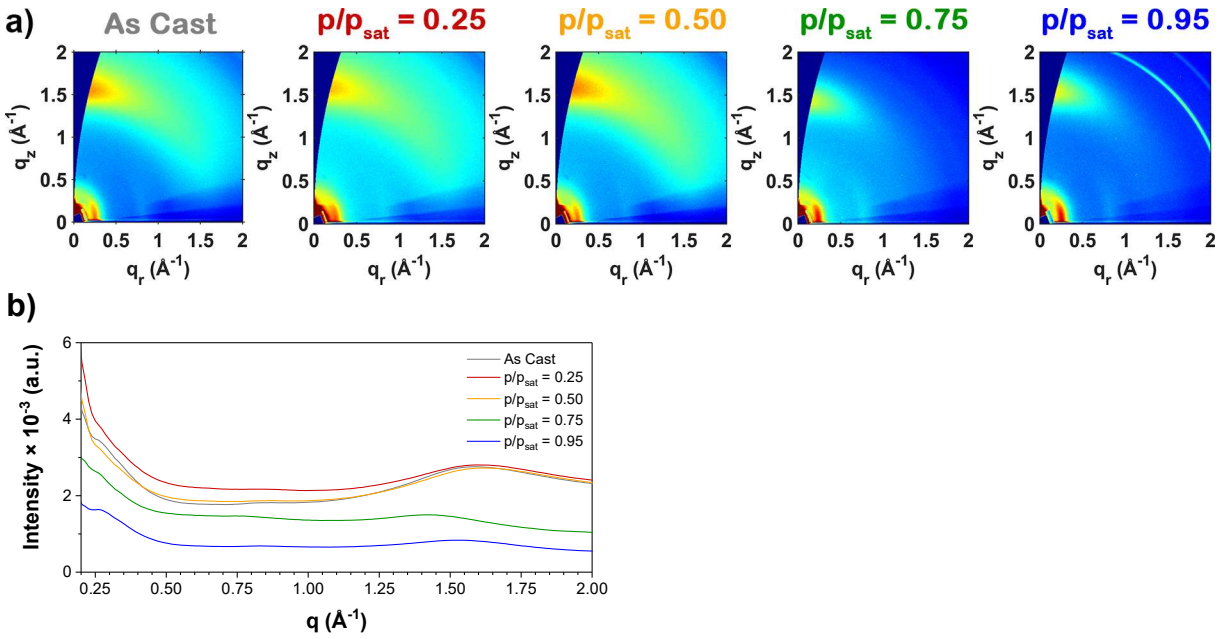

Figure 3.18: (a) GIWAXS patterns of neat PTB7-Th thin films annealed at various chloroform vapour concentrations. (b) Azimuthally-integrated linecuts (from $\chi = -85°$ to 85°) of the GIWAXS patterns from (a).

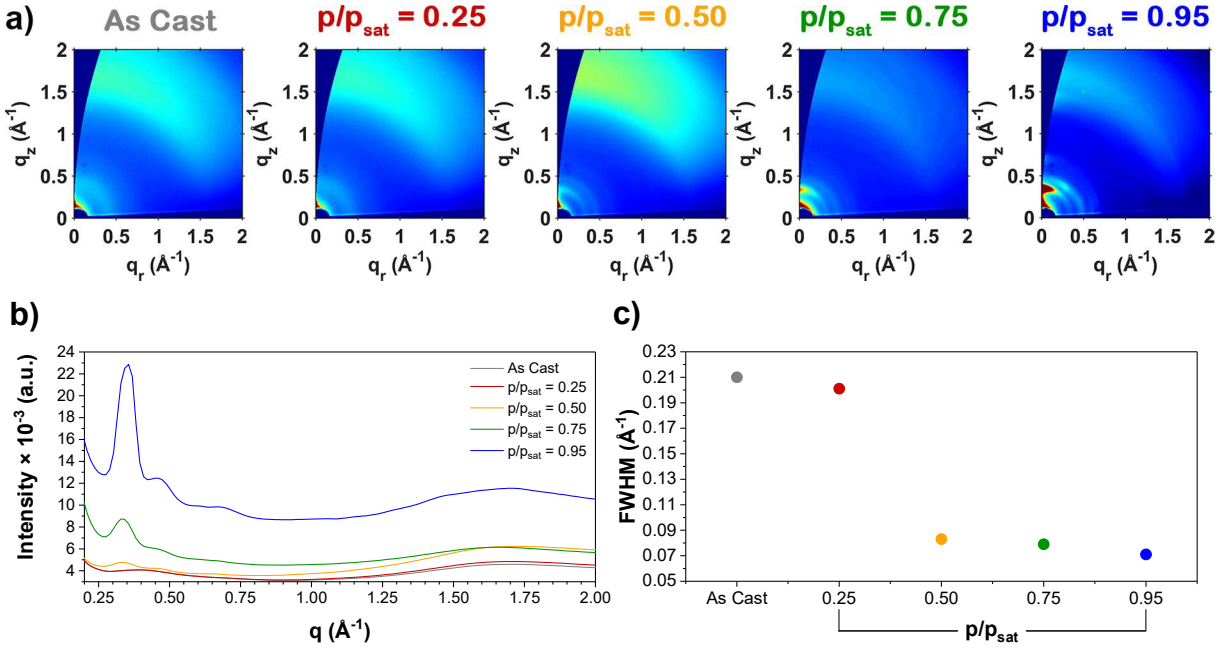

Figure 3.19: (a) GIWAXS patterns of neat PDI-DPP-PDI thin films annealed at various chloroform concentrations. (b) Azimuthally-integrated linecuts (from $\chi = -80°$ to 80°) of the GIWAXS patterns from (a). (c) FWHM of the peak at $q \approx 0.38$ Å^{-1} (as cast and $p/p_{sat} = 0.25$) and $q \approx 0.32$ Å^{-1} ($p/p_{sat} = 0.50$, 0.75, and 0.95).

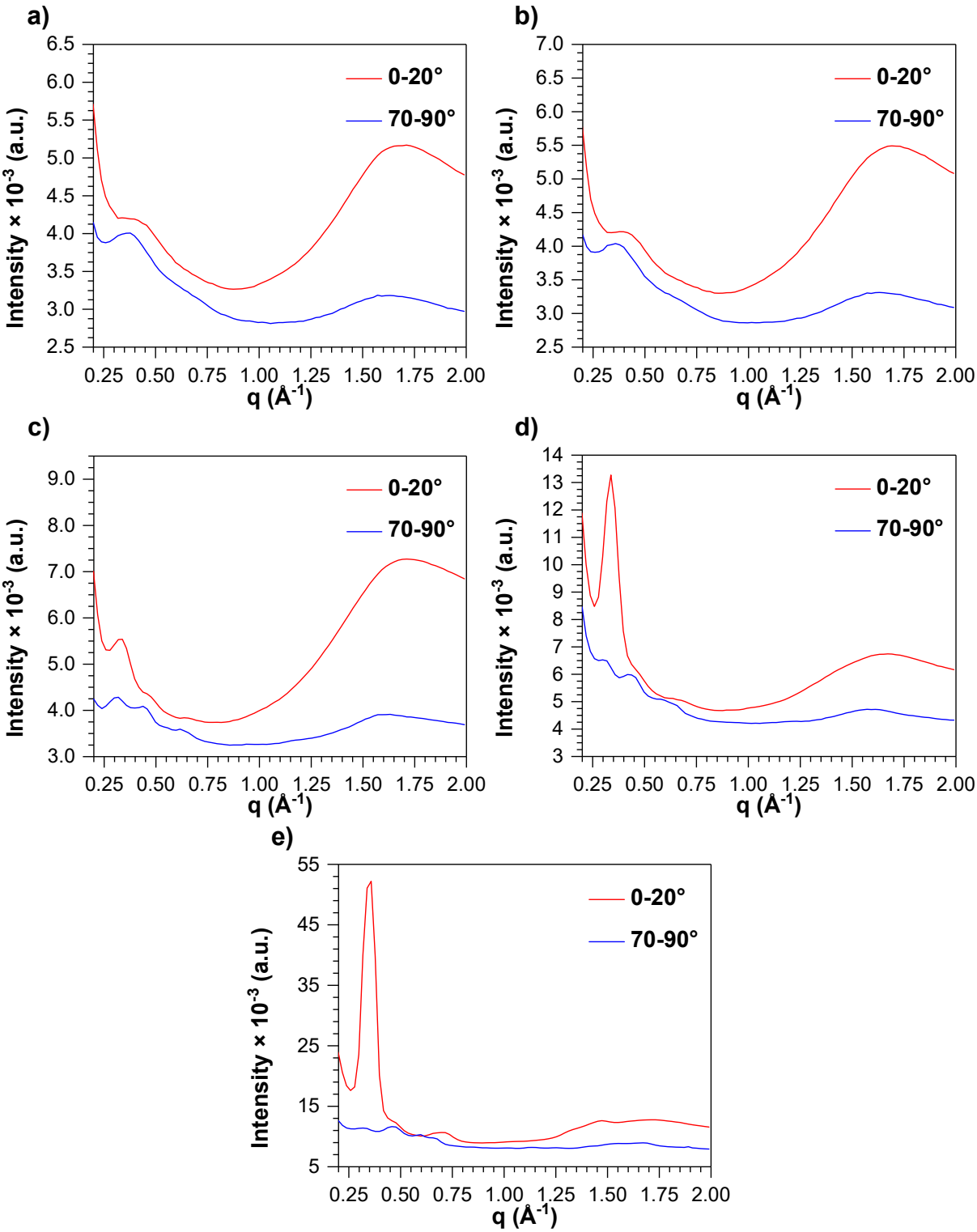

Figure 3.20: GIWAXS linecuts of neat PDI-DPP-PDI thin films, azimuthally-integrated from χ = 0-20° and χ = 70-90°, where χ is the angle between q and q_z. PDI-DPP-PDI films were: (a) as cast, and annealed at (b) 0.25, (c) 0.50, (d) 0.75, and (e) 0.95 p/p_{sat}.

GIWAXS patterns of BHJ films of PTB7-Th:PDI-DPP-PDI were collected to examine the crystallinity of the BHJ blend **(Figure 3.21)**. The mixing of donor and acceptor materials breaks up the stacking of each individual material and reduces the overall crystallinity of both PTB7-Th and PDI-DPP-PDI. The as cast film has a broad lamellar stacking peak at $q \approx 0.32$ Å^{-1} (which is an overlap of the PTB7-Th (100) peak and the first PDI-DPP-PDI peak)[52,166,167] and a weak broad peak centered around $q \approx 1.5$ Å^{-1}. Similar to the neat materials there is no significant change in the GIWAXS pattern upon VP-SVA at a chloroform vapour concentration of $p/p_{sat} = 0.25$; however, there is a large decrease in the FWHM of the peak at $q \approx 0.32$ Å^{-1} indicating an increase in the crystallite sizes of the BHJ materials (again it must be noted that because the peak is an overlap of two peaks, the change in crystallite size of each material cannot be quantified). At $p/p_{sat} = 0.50$ there is a large increase in the degree of preferred orientation for the overlapping peak at $q \approx 0.32$ Å^{-1}, which could be the PDI-DPP-PDI crystallizing and orienting parallel to the substrate (more likely), or the PTB7-Th (100) orienting edge on (less likely)[152] **(Figure 3.22)**. Additionally, the PDI-DPP-PDI peaks at $q \approx 0.43$ Å^{-1} and 0.64 Å^{-1} begin to diffract weakly (primarily on the q_r axis) and there remains a weak broad peak around $q \approx 1.5$ Å^{-1} **(Figure 3.22)**. When the chloroform vapour concentration is increased to $p/p_{sat} = 0.75$, the preferred orientation of PTB7-Th and PDI-DPP-PDI increases further and the signal intensity for the PDI-DPP-PDI peaks at $q \approx 0.44$ Å^{-1} and 0.62 Å^{-1} grow more intense. Additionally, there is another large drop in the FWHM of the lamellar stacking peaks, indicating a further increase in crystallite size. Increasing the chloroform concentration to $p/p_{sat} = 0.95$ results in little further change in the GIWAXS pattern and only a slight decrease in the FWHM of the peak at $q \approx 0.32$ Å^{-1}.

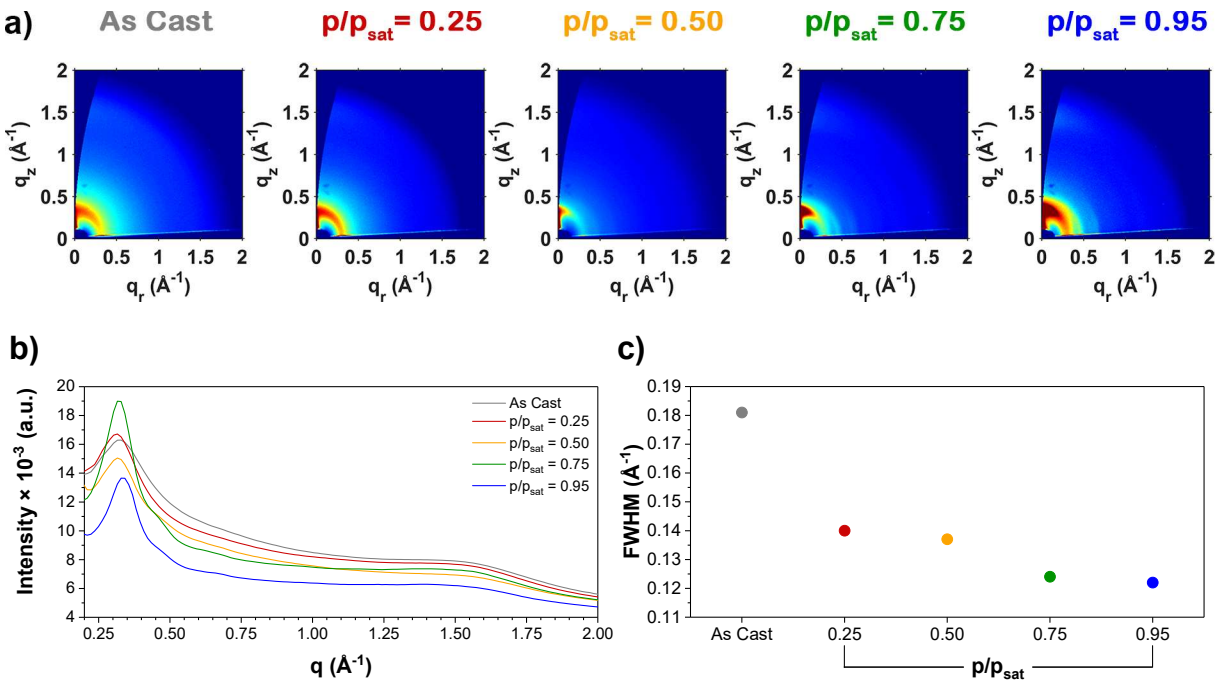

Figure 3.21: (a) GIWAXS patterns of PTB7-Th:PDI-DPP-PDI thin films annealed at various chloroform vapour concentrations. (b) Azimuthally-integrated linecuts (from $\chi = -80°$ to 80°) of the GIWAXS patterns from (a). (c) FWHM of the peak at $q \approx 0.30$ Å^{-1} after background subtraction.

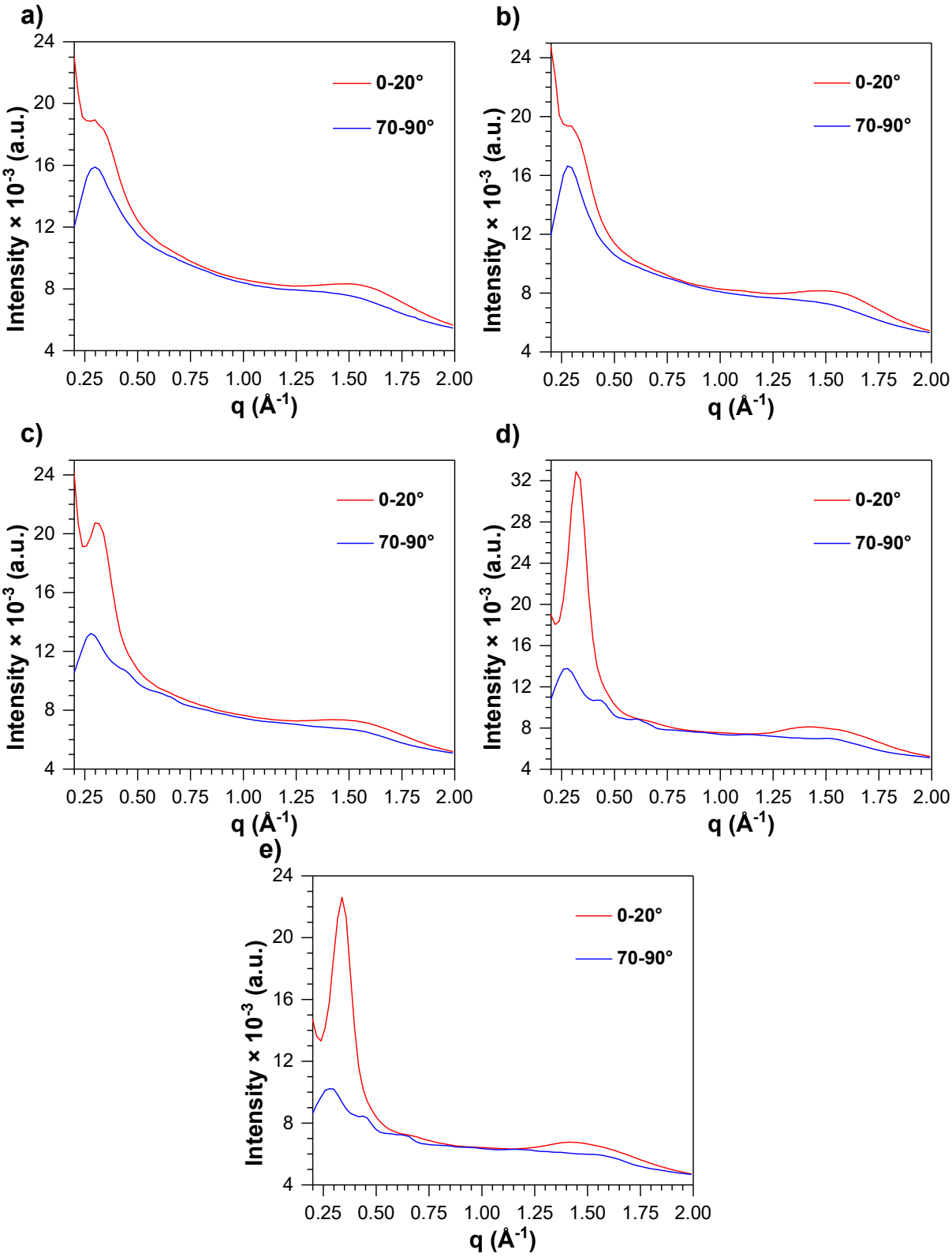

Figure 3.22: GIWAXS linecuts of PTB7-Th:PDI-DPP-PDI thin films, azimuthally-integrated from χ = 0-20° and χ = 70-90°, where χ is the angle between q and q_z. PTB7-Th:PDI-DPP-PDI films were: (a) as cast, and annealed at (b) 0.25, (c) 0.50, (d) 0.75, and (e) 0.95 p/p_{sat}.

3.3.4. Device Performance

To correlate device performance with changes in morphology, PTB7-Th:PDI-DPP-PDI devices were fabricated following literature procedures,[78] and annealed at various chloroform concentrations. As cast devices had a PCE of 1.0 ± 0.3% **(Figure 3.23** and **Table 3.2)**. The poor efficiency is due to poor charge transport indicated by poor J_{SC}, FF, and R_S **(Table 3.2)**. No statistical difference in PCE was seen after SVA with chloroform vapour at p/p_{sat} = 0.25 (PCE = 0.9 ± 0.1%). There was a large increase in PCE after annealing at p/p_{sat} = 0.50 (2.8 ± 0.6%) due to a large increase in J_{SC} and FF, and a decrease in R_S. There was no statistical increase in PCE when the chloroform vapour concentration was increased to p/p_{sat} = 0.75 (3.0 ± 0.5%). At a chloroform concentration of p/p_{sat} = 0.95 the PCE dropped to 2.4 ± 0.8 % as the devices over annealed. The loss in efficiency is primarily attributed to a loss in J_{SC}. Additionally, the substrate to substrate variability in device efficiency rose dramatically as the concentration of chloroform vapour was increased.

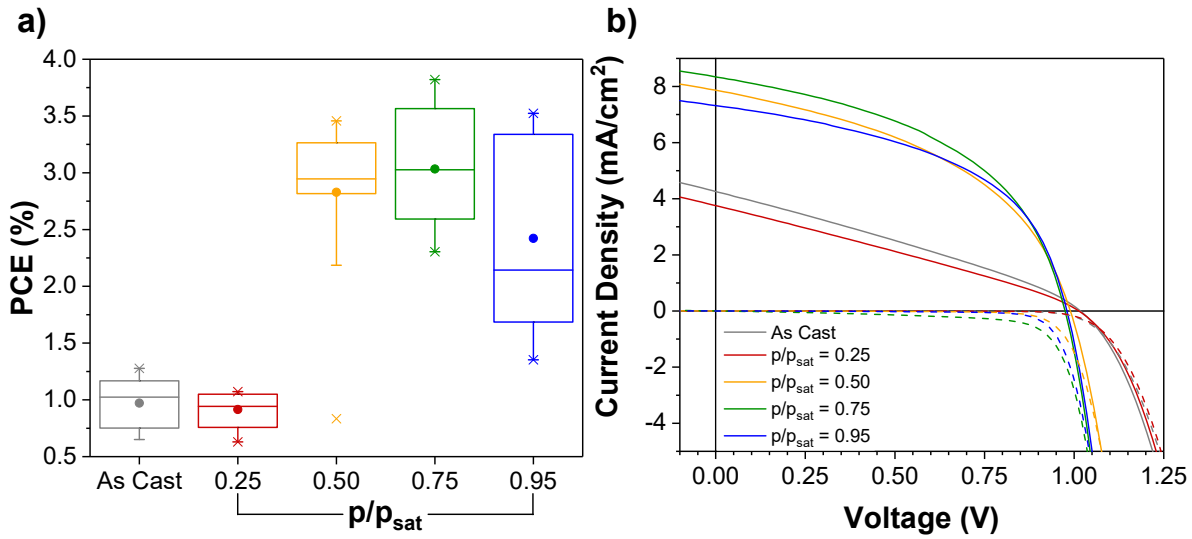

Figure 3.23: (a) Power conversion efficiency of PTB7-Th:PDI-DPP-PDI devices annealed at various chloroform concentrations. The dots represent mean values, and the central lines the medians. The box defines the 25th and 75th percentiles, while the bars define the 5th and 95th percentiles. The maximum and minimum PCE values are each denoted by an ×. Device statistics were derived from measurements on a minimum of 27 devices (8 devices per substrate). (b) J-V curves in the light (solid) and the dark (dashed) for the highest performing PTB7-Th:PDI-DPP-PDI devices annealed at various chloroform concentrations.

Table 3.2: Device performance parameters for PTB7-Th:PDI-DPP-PDI devices annealed at various chloroform vapour concentrations.

Annealing Condition	*N*	V_{oc} (V)	J_{sc} [a] (mA·cm^{-2})	Fill Factor (%)	PCE [a] (%)	R_S [b] (Ω·cm^2)	$R_{Sh} \times 10^{-2}$ [b] (Ω·cm^2)
As Cast	30	0.9 ± 0.2	3.7 ± 0.3	28.8 ± 0.7	1.0 ± 0.3	19 ± 3	3.7 ± 0.5
p/p_{sat} = 0.25	31	0.9 ± 0.1	3.4 ± 0.3	28.4 ± 0.4	0.9 ± 0.1	17 ± 2	4.0 ± 0.2
p/p_{sat} = 0.50	32	0.9 ± 0.1	7.1 ± 0.4	41 ± 4	2.8 ± 0.6	7 ± 1	4.5 ± 0.9
p/p_{sat} = 0.75	27	0.92 ± 0.06	7.8 ± 0.5	42 ± 3	3.0 ± 0.5	14 ± 11	4.5 ± 0.7
p/p_{sat} = 0.95	31	0.9 ± 0.2	6 ± 1	43 ± 5	2.4 ± 0.8	7 ± 3	6 ± 1

[a] J_{sc} and PCE were calculated using the apertured device area (0.0708 cm^2). [b] Resistances were calculated based on the slope at J_{sc} (R_{Sh}) and in the series resistance-limited regime (1.34-1.39 V, R_S), using the non-apertured device area (0.085 cm^2).

There is little indication of morphology change in the UV/Vis spectra or PiFM images of the PTB7-Th:PDI-DPP-PDI thin films annealed at low chloroform concentrations (p/p_{sat} = 0.25, and 0.50). However, there is a jump in PCE between devices annealed at p/p_{sat} = 0.25 and 0.50. The in-plane and out-of-plane linecuts of the PTB7-Th:PDI-DPP-PDI GIWAXS patterns reveal that as

the concentration of chloroform vapour increases to p/p_{sat} = 0.50 there is an increase in PDI-DPP-PDI preferred orientation and crystallinity as new diffraction peaks at q ≈ 0.42 $Å^{-1}$ and q ≈ 0.60 $Å^{-1}$ grow in along the in-plane q_r axis **(Figure 3.22)**. Therefore, the increase in device efficiency at p/p_{sat} = 0.50 could be related to an increase in PDI-DPP-PDI crystallinity, which improves charge transport in the BHJ. From the UV/Vis spectroscopy data it was shown that a new DPP stacking motif is observed when annealing at or above chloroform vapour concentrations of p/p_{sat} = 0.75; while it cannot be determined for certain without single crystal data, the new diffraction peaks could be DPP arranging into a more ordered stacking motif, increasing charge transport.

Over annealing occurs at a chloroform concentration of p/p_{sat} = 0.95 resulting in a loss of photocurrent. The loss of photocurrent is likely due to an increase in geminate recombination resulting from the excessively large domains of PDI-DPP-PDI visible in the PiFM images. Increasing the degree of preferred orientation of the PDI-DPP-PDI could also have a minor contribution to a lack of charge transport in the BHJ system.

Chapter 4: Conclusions

4.1. Summary

Solvent vapour annealing is an important post deposition treatment to increase the efficiency of OPVs. Previous methods of SVA lacked control over the solvent vapour concentration and were inherently small batch processes. In this thesis, flow through variable pressure solvent vapour annealing was successfully used to control the morphology of OPV BHJ blends. P3HT:$PC_{61}BM$ was chosen as a model system to test the VP-SVA system because the morphology of P3HT has been well studied.[43,70,72,77,104,111] Aggregation of P3HT has been shown to increase charge transport within BHJ films. The aggregation of P3HT could be controlled using the VP-SVA system by varying the partial pressure of chloroform vapour inside the annealing chamber, with higher concentrations leading to a higher degree of aggregation as evidenced by UV/Vis spectroscopy. The size and purity of material domains in a BHJ are of the utmost importance for device performance; if the domains are too large or too small, photocurrent is limited by exciton recombination. PiFM was used to image the material domains in the BHJ blend directly, using their unique IR absorbances. It was shown that increasing the concentration of chloroform vapour increased the phase separation, resulting in larger domains of P3HT and $PC_{61}BM$. In many cases, the crystallinity and orientation of materials in a BHJ blend is directly related to their charge transport characteristics. To examine the crystallinity of P3HT, GIWAXS was performed on thin films of P3HT:$PC_{61}BM$. It was shown that films of P3HT:$PC_{61}BM$ cast from chloroform resulted in primarily face on orientation. Annealing P3HT:$PC_{61}BM$ films at increasingly higher chloroform concentrations increased the crystallite size of P3HT. At a chloroform vapour concentration of

p/p_{sat} = 0.95, P3HT chains had enough freedom of movement to rearrange to a more edge on orientation. $PC_{61}BM$ crystallites remained isotropic throughout the annealing process.

P3HT:$PC_{61}BM$ devices were fabricated using the inverted structure and annealed at various chloroform concentrations to correlate device performance to the morphological changes in P3HT:$PC_{61}BM$ films. It was shown that device performance gradually increases as the concentration of chloroform vapour is increased until a critical point where over annealing begins. For P3HT:$PC_{61}BM$, annealing at a chloroform vapour concentration of p/p_{sat} = 0.75 increased the efficiency from 1.6% (as cast) to 2.9%. The increase in efficiency was primarily due to an increase in photocurrent and a decrease in series resistance caused by increased charge transport in highly aggregated P3HT. Increasing the chloroform vapour concentration further to p/p_{sat} = 0.95 resulted in a reduction of photocurrent from over annealing; this reduction in photocurrent was likely due to increased geminate recombination caused by the formation of large globular domains of $PC_{61}BM$.

P3HT is a semi-crystalline homopolymer and does not resemble many modern push-pull polymers, which are more weakly ordered.[103] As a result, not all processes that increase the efficiency of P3HT have worked on modern OPV systems. To validate the flow through VP-SVA method for modern systems, PTB7-Th:PDI-DPP-PDI was chosen as a model system for modern push-pull donor:NFA systems. PTB7-Th:PDI-DPP-PDI has been shown to increase in efficiency with SVA in chloroform; however, it is prone to over annealing, making it an ideal candidate to study the flow through VP-SVA system.[78] To investigate the electronic transitions of PTB7-Th:PDI-DPP-PDI, *in situ* UV/Vis spectroscopy was performed. It was shown that annealing at chloroform vapour concentrations at or above p/p_{sat} = 0.75 induced a rearrangement of the DPP core in the acceptor. Little change in the UV/Vis spectra occurred at lower chloroform

concentrations. This result was mirrored in the domain sizes imaged by PiFM. The as cast film and films annealed at low chloroform concentrations (p/p_{sat} = 0.25 and 0.50) resulted in a mostly homogenous film with small material domains. Once over the threshold of p/p_{sat} = 0.75 there was a large increase in domain size as the films were annealed. A different trend was seen in the crystallinity of the acceptor as monitored by GIWAXS. The BHJ films as cast and annealed at p/p_{sat} = 0.25 were mostly weakly ordered due to the mixing of PTB7-Th and PDI-DPP-PDI. At chloroform concentrations greater than p/p_{sat} = 0.50, new peaks appeared in the diffraction pattern of neat PDI-DPP-PDI and the BHJ blend indicating new crystallite stacking in the acceptor.

Devices of PTB7-Th:PDI-DPP-PDI were fabricated to correlate morphology changes to device performance. It was found that the as cast film and the film annealed at p/p_{sat} = 0.25 had low efficiencies (1.0% and 0.9% respectively), but there was a large jump in efficiency at p/p_{sat} = 0.50 (2.8%). Since there was no change in the UV/Vis spectra or PiFM images between films annealed at p/p_{sat} = 0.25 and 0.50, the increase in efficiency was attributed to increased acceptor crystallinity. The device efficiency was unchanged when the chloroform concentration was increased to p/p_{sat} = 0.75, but increasing the chloroform concentration further to p/p_{sat} = 0.95 resulted in a reduction in device performance due to excessively large material domains. The over annealing of both P3HT:PC_{61}BM and PTB7-Th:PDI-DPP-PDI illustrates the importance of controlling the concentration of annealing solvent vapour to optimize BHJ morphology and device performance.

4.2. Future Work

To be industrially viable, annealing times will need to be decreased to the time scale of roll-to-roll processing. The first short term future direction this project can take is to optimize the annealing time. It is clear from the *in situ* UV/Vis annealing data of P3HT:PC_{61}BM thin films that

the aggregation of P3HT plateaus early in the annealing process for higher chloroform concentrations. It may be possible to reproduce similar device performance with vastly reduced annealing times. While the rearrangement of the DPP in PTB7-Th:PDI-DPP-PDI films does not seem to plateau within 30 minutes of annealing, the films annealed at $p/p_{sat} = 0.95$ exhibit over annealing. With optimization, perhaps an annealing concentration between $p/p_{sat} = 0.75$ and 0.95 can be found where the films anneal quickly to the optimum morphology without over annealing.

A second short term project could be to increase the number of chloroform vapour concentrations tested. The PTB7-Th:PDI-DPP-PDI devices annealed at $p/p_{sat} = 0.50$ and 0.75 had statistically identical efficiencies, despite having largely different morphologies by UV/Vis spectroscopy and PiFM. Additionally, there were large day-to-day variations in the efficiencies, which could have come from slightly different chloroform vapour concentrations caused by temperature fluctuations in the lab. It would be prudent to do a more thorough investigation of the impact of precise changes in chloroform vapour on film morphology and device performance. I propose examining the device morphology and efficiency at intervals of $p/p_{sat} = 0.05$ from $p/p_{sat} = 0.45$ to 0.80 to gain a clearer picture of what is occurring during annealing at chloroform concentrations between $p/p_{sat} = 0.50$ and 0.75.

A long-term direction for this project is to add an additional flow controller and set of solvent bubblers to do multiple solvent SVA. It has been shown in the literature that solvents which can selectively anneal the donor or acceptor are available and can be used to fine tune the morphology of the BHJ.[43,77] Verploegen et. al. showed that THF and chloroform vapour annealing have similar effects on P3HT crystallinity, but THF induced crystallization in $PC_{61}BM$ while chloroform did not.[43] By varying the ratio of chloroform and THF used in the annealing process, the crystallization of P3HT and $PC_{61}BM$ could be tuned independently. Tang et. al. used THF and CS_2 VP-SVA

annealing steps sequentially to control the morphology of P3HT:$PC_{61}BM$ devices.[77] Tang et al.'s solvent system could be used with the flow through VP-SVA system to increase annealing throughput. More importantly however, this idea could be used to selectively anneal each component in modern donor:NFA systems.

Chapter 5: References

(1) Battaglia, C.; Cuevas, A.; De Wolf, S.; Rappich, J.; Korte, L.; Rech, B.; Nickel, N. H.; Pellet, N.; Lee, J. Z.; Gratzel, M.; et al. High-Efficiency Crystalline Silicon Solar Cells: Status and Perspectives. *Energy Environ. Sci.* **2016**, *9*, 1552–1576.

(2) Mazzio, K. A.; Luscombe, C. K. The Future of Organic Photovoltaics. *Chem. Soc. Rev.* **2015**, *44*, 78–90.

(3) Binetti, S.; Breneman, W. C.; Buonassisi, T.; Ceccaroli, B.; Delannoy, Y.; Heuer, M.; Julsrud, S.; Morita, K.; Nadal, C. del C.; Ovrelid, E.; et al. *Solar Silicon Processes Technologies, Challenges, and Opportunities*; CRC Press/Taylor & Francis: Boca Raton FL, 2017.

(4) Neamen, Donald, A. *Semiconductor Physics and Devices*, 3rd ed.; McGraw-Hill: New York, 2003.

(5) Nelson, J. *The Physics of Solar Cells*; Imperial College Press: London UK, 2003.

(6) Sinha, P. Life Cycle Materials and Water Management for CdTe Photovoltaics. *Sol. Energy Mater. Sol. Cells* **2013**, *119*, 271–275.

(7) Poorkazem, K.; Kelly, T. L. Improving the Stability and Decreasing the Trap State Density of Mixed-Cation Perovskite Solar Cells through Compositional Engineering. *Sustain. Energy Fuels* **2018**, *2*, 1332–1341.

(8) Xie, Y.; Tang, Y.; Wu, W.; Wang, Y.; Liu, J.; Li, X.; Tian, H.; Zhu, W.-H. Porphyrin

Cosensitization for a Photovoltaic Efficiency of 11.5%: A Record for Non-Ruthenium Solar Cells Based on Iodine Electrolyte. *J. Am. Chem. Soc.* **2015**, *137*, 14055–14058.

(9) Wallace, S. K.; Mitzi, D. B.; Walsh, A. The Steady Rise of Kesterite Solar Cells. *ACS Energy Lett.* **2017**, *2*, 776–779.

(10) Zhang, S.; Qin, Y.; Zhu, J.; Hou, J. Over 14% Efficiency in Polymer Solar Cells Enabled by a Chlorinated Polymer Donor. *Adv. Mater.* **2018**, 1800868.

(11) Zheng, Z.; Hu, Q.; Zhang, S.; Zhang, D.; Wang, J.; Xie, S.; Wang, R.; Qin, Y.; Li, W.; Hong, L.; et al. A Highly Efficient Non-Fullerene Organic Solar Cell with a Fill Factor over 0.80 Enabled by a Fine-Tuned Hole-Transporting Layer. *Adv. Mater.* **2018**, 1801801.

(12) Davy, N. C.; Sezen-Edmonds, M.; Gao, J.; Lin, X.; Liu, A.; Yao, N.; Kahn, A.; Loo, Y.-L. Pairing of Near-Ultraviolet Solar Cells with Electrochromic Windows for Smart Management of the Solar Spectrum. *Nat. Energy* **2017**, *2*, 17104.

(13) Infinity PV https://infinitypv.com/ (accessed Jan 4, 2018).

(14) Xue, Q.; Xia, R.; Brabec, C. J.; Yip, H.-L. Recent Advances in Semi-Transparent Polymer and Perovskite Solar Cells for Power Generating Window Applications. *Energy Environ. Sci.* **2018**.

(15) Gu, X.; Yan, H.; Kurosawa, T.; Schroeder, B. C.; Gu, K. L.; Zhou, Y.; To, J. W. F.; Oosterhout, S. D.; Savikhin, V.; Molina-Lopez, F.; et al. Comparison of the Morphology Development of Polymer-Fullerene and Polymer-Polymer Solar Cells during Solution-Shearing Blade Coating. *Adv. Energy Mater.* **2016**, *6*, 1601225.

(16) Heliatek http://www.heliatek.com/en/ (accessed Aug 8, 2017).

(17) Burkhart, B.; Thompson, B. C.; Lunt, R. R.; Holmes, R. J.; He, Y.; Po, R.; Carbonera, C.; Bernardi, A.; Camaioni, N.; Yoo, S.; et al. *Organic Solar Cells. Fundamentals, Devices, and Upscaling*; Rand, B. P., Richter, H., Eds.; Pan Stanford Publishing Pte. Ltd.: Singapore, 2014.

(18) National Renewable Energy Laboratory https://rredc.nrel.gov/solar/spectra/am1.5/.

(19) Shen, Y.; Gupta, M. C. Investigation of Electrical Characteristics of P3HT:PCBM Organic Solar Cells. In *2012 38th IEEE Photovoltaic Specialists Conference*; IEEE, 2012; pp 002770–002774.

(20) *CRC Handbook of Chemistry and Physics, 98th Edition*; Rumble, J. R., Ed.; CRC Press/Taylor & Francis, Boca Raton, FL, 2018.

(21) Hedley, G. J.; Ruseckas, A.; Samuel, I. D. W. Light Harvesting for Organic Photovoltaics. *Chem. Rev.* **2017**, *117*, 796–837.

(22) Tang, C. W. Two-layer Organic Photovoltaic Cell. *Appl. Phys. Lett.* **1986**, *48*, 183–185.

(23) Yu, G.; Gao, J.; Hummelen, J. C.; Wudl, F.; Heeger, A. J. Polymer Photovoltaic Cells: Enhanced Efficiencies via a Network of Internal Donor-Acceptor Heterojunctions. *Science* **1995**, *270*, 1789–1791.

(24) Reinspach, J. A.; Diao, Y.; Giri, G.; Sachse, T.; England, K.; Zhou, Y.; Tassone, C.; Worfolk, B. J.; Presselt, M.; Toney, M. F.; et al. Tuning the Morphology of Solution-Sheared P3HT:PCBM Films. *ACS Appl. Mater. Interfaces* **2016**, *8*, 1742–1751.

(25) Galagan, Y.; Fledderus, H.; Gorter, H.; ’t Mannetje, H. H.; Shanmugam, S.; Mandamparambil, R.; Bosman, J.; Rubingh, J.-E. J. M.; Teunissen, J.-P.; Salem, A.; et al.

Roll-to-Roll Slot-Die Coated Organic Photovoltaic (OPV) Modules with High Geometrical Fill Factors. *Energy Technol.* **2015**, *3*, 834–842.

(26) Krebs, F. C. Fabrication and Processing of Polymer Solar Cells: A Review of Printing and Coating Techniques. *Sol. Energy Mater. Sol. Cells* **2009**, *93*, 394–412.

(27) McDowell, C.; Abdelsamie, M.; Toney, M. F.; Bazan, G. C. Solvent Additives: Key Morphology-Directing Agents for Solution-Processed Organic Solar Cells. *Adv. Mater.* **2018**, 1707114.

(28) Kim, M.; Lee, J.; Jo, S. B.; Sin, D. H.; Ko, H.; Lee, H.; Lee, S. G.; Cho, K. Critical Factors Governing Vertical Phase Separation in Polymer–PCBM Blend Films for Organic Solar Cells. *J. Mater. Chem. A* **2016**, *4*, 15522–15535.

(29) Kouijzer, S.; Michels, J. J.; van den Berg, M.; Gevaerts, V. S.; Turbiez, M.; Wienk, M. M.; Janssen, R. A. J. Predicting Morphologies of Solution Processed Polymer:Fullerene Blends. *J. Am. Chem. Soc.* **2013**, *135*, 12057–12067.

(30) Kim, J.-H.; Gadisa, A.; Schaefer, C.; Yao, H.; Gautam, B. R.; Balar, N.; Ghasemi, M.; Constantinou, I.; So, F.; O'Connor, B. T.; et al. Strong Polymer Molecular Weight-Dependent Material Interactions: Impact on the Formation of the Polymer/Fullerene Bulk Heterojunction Morphology. *J. Mater. Chem. A* **2017**, *5*, 13176–13188.

(31) Mei, J.; Bao, Z. Side Chain Engineering in Solution-Processable Conjugated Polymers. *Chem. Mater.* **2014**, *26*, 604–615.

(32) Kim, Y.; Cook, S.; Tuladhar, S. M.; Choulis, S. A.; Nelson, J.; Durrant, J. R.; Bradley, D. D. C.; Giles, M.; McCulloch, I.; Ha, C.-S.; et al. A Strong Regioregularity Effect in Self-

Organizing Conjugated Polymer Films and High-Efficiency Polythiophene:Fullerene Solar Cells. *Nat. Mater.* **2006**, *5*, 197–203.

(33) Ma, W.; Kim, J. Y.; Lee, K.; Heeger, A. J. Effect of the Molecular Weight of Poly(3-Hexylthiophene) on the Morphology and Performance of Polymer Bulk Heterojunction Solar Cells. *Macromol. Rapid Commun.* **2007**, *28*, 1776–1780.

(34) Inoue, S.; Minemawari, H.; Tsutsumi, J.; Chikamatsu, M.; Yamada, T.; Horiuchi, S.; Tanaka, M.; Kumai, R.; Yoneya, M.; Hasegawa, T. Effects of Substituted Alkyl Chain Length on Solution-Processable Layered Organic Semiconductor Crystals. *Chem. Mater.* **2015**, *27*, 3809–3812.

(35) Piliego, C.; Holcombe, T. W.; Douglas, J. D.; Woo, C. H.; Beaujuge, P. M.; Fréchet, J. M. J. Synthetic Control of Structural Order in *N* -Alkylthieno[3,4- *c*]Pyrrole-4,6-Dione-Based Polymers for Efficient Solar Cells. *J. Am. Chem. Soc.* **2010**, *132*, 7595–7597.

(36) Huang, Y.; Kramer, E. J.; Heeger, A. J.; Bazan, G. C. Bulk Heterojunction Solar Cells: Morphology and Performance Relationships. *Chem. Rev.* **2014**, *114*, 7006–7043.

(37) Zhao, J.; Li, Y.; Yang, G.; Jiang, K.; Lin, H.; Ade, H.; Ma, W.; Yan, H. Efficient Organic Solar Cells Processed from Hydrocarbon Solvents. *Nat. Energy* **2016**, *1*, 15027.

(38) Nagarajan, K.; Gopan, G.; Cheriya, R. T.; Hariharan, M. Long Alkyl Side-Chains Impede Exciton Interaction in Organic Light Harvesting Crystals. *Chem. Commun.* **2017**, *53*, 7409–7411.

(39) Aldrich, T. J.; Swick, S. M.; Melkonyan, F. S.; Marks, T. J. Enhancing Indacenodithiophene Acceptor Crystallinity via Substituent Manipulation Increases

Organic Solar Cell Efficiency. *Chem. Mater.* **2017**, *29*, 10294–10298.

(40) Tremel, K.; Ludwigs, S. *Morphology of P3HT in Thin Films in Relation to Optical and Electrical Properties*; 2014; Vol. 265.

(41) Walker, B.; Tamayo, A.; Duong, D. T.; Dang, X.-D.; Kim, C.; Granstrom, J.; Nguyen, T.-Q. A Systematic Approach to Solvent Selection Based on Cohesive Energy Densities in a Molecular Bulk Heterojunction System. *Adv. Energy Mater.* **2011**, *1*, 221–229.

(42) Clark, J.; Chang, J. F.; Spano, F. C.; Friend, R. H.; Silva, C. Determining Exciton Bandwidth and Film Microstructure in Polythiophene Films Using Linear Absorption Spectroscopy. *Appl. Phys. Lett.* **2009**, *94*, 163306.

(43) Verploegen, E.; Miller, C. E.; Schmidt, K.; Bao, Z.; Toney, M. F. Manipulating the Morphology of P3HT–PCBM Bulk Heterojunction Blends with Solvent Vapor Annealing. *Chem. Mater.* **2012**, *24*, 3923–3931.

(44) Machui, F.; Langner, S.; Zhu, X.; Abbott, S.; Brabec, C. J. Determination of the P3HT:PCBM Solubility Parameters via a Binary Solvent Gradient Method: Impact of Solubility on the Photovoltaic Performance. *Sol. Energy Mater. Sol. Cells* **2012**, *100*, 138–146.

(45) Chen, X.; Liu, X.; Burgers, M. A.; Huang, Y.; Bazan, G. C. Green-Solvent-Processed Molecular Solar Cells. *Angew. Chemie Int. Ed.* **2014**, *53*, 14378–14381.

(46) Farahat, M. E.; Perumal, P.; Budiawan, W.; Chen, Y.-F.; Lee, C.-H.; Chu, C.-W. Efficient Molecular Solar Cells Processed from Green Solvent Mixtures. *J. Mater. Chem. A* **2017**, *5*, 571–582.

(47) Dayneko, S. V.; Hendsbee, A. D.; Welch, G. C. Fullerene-Free Polymer Solar Cells Processed from Non-Halogenated Solvents in Air with PCE of 4.8%. *Chem. Commun.* **2017**, *53*, 1164–1167.

(48) Yu, Y.-Y.; Tsai, T.-W.; Yang, C.-C.; Chen, C.-P. Highly Efficient Non-Fullerene Organic Photovoltaics Processed from *o* -Xylene without Using Additives. *J. Phys. Chem. C* **2017**, *121*, 21969–21974.

(49) Oosterhout, S. D.; Savikhin, V.; Burgers, M. A.; Zhang, J.; Zhang, Y.; Marder, S. R.; Bazan, G. C.; Toney, M. F. Absence of Mixed Phase in Organic Photovoltaic Active Layers Facilitates Use of Green Solvent Processing. *J. Phys. Chem. C* **2018**, *122*, 11136–11144.

(50) Peet, J.; Soci, C.; Coffin, R. C.; Nguyen, T. Q.; Mikhailovsky, A.; Moses, D.; Bazan, G. C. Method for Increasing the Photoconductive Response in Conjugated Polymer/Fullerene Composites. *Appl. Phys. Lett.* **2006**, *89*, 252105.

(51) Peet, J.; Kim, J. Y.; Coates, N. E.; Ma, W. L.; Moses, D.; Heeger, A. J.; Bazan, G. C. Efficiency Enhancement in Low-Bandgap Polymer Solar Cells by Processing with Alkane Dithiols. *Nat. Mater.* **2007**, *6*, 497–500.

(52) Tremolet de Villers, B. J.; O'Hara, K. A.; Ostrowski, D. P.; Biddle, P. H.; Shaheen, S. E.; Chabinyc, M. L.; Olson, D. C.; Kopidakis, N. Removal of Residual Diiodooctane Improves Photostability of High-Performance Organic Solar Cell Polymers. *Chem. Mater.* **2016**, *28*, 876–884.

(53) Lee, S.; Kong, J.; Lee, K. Air-Stable Organic Solar Cells Using an Iodine-Free Solvent Additive. *Adv. Energy Mater.* **2016**, *6*, 1600970.

(54) Huang, W.; Gann, E.; Xu, Z.-Q.; Thomsen, L.; Cheng, Y.-B.; McNeill, C. R. A Facile Approach to Alleviate Photochemical Degradation in High Efficiency Polymer Solar Cells. *J. Mater. Chem. A* **2015**, *3*, 16313–16319.

(55) Lee, J. K.; Ma, W. L.; Brabec, C. J.; Yuen, J.; Moon, J. S.; Kim, J. Y.; Lee, K.; Bazan, G. C.; Heeger, A. J. Processing Additives for Improved Efficiency from Bulk Heterojunction Solar Cells. *J. Am. Chem. Soc.* **2008**, *130*, 3619–3623.

(56) Peet, J.; Cho, N. S.; Lee, S. K.; Bazan, G. C. Transition from Solution to the Solid State in Polymer Solar Cells Cast from Mixed Solvents. *Macromolecules* **2008**, *41*, 8655–8659.

(57) Gu, K. L.; Zhou, Y.; Morrison, W. A.; Park, K.; Park, S.; Bao, Z. Nanoscale Domain Imaging of All-Polymer Organic Solar Cells by Photo-Induced Force Microscopy. *ACS Nano* **2018**, *12*, 1473–1481.

(58) Hoven, C. V.; Dang, X.-D.; Coffin, R. C.; Peet, J.; Nguyen, T.-Q.; Bazan, G. C. Improved Performance of Polymer Bulk Heterojunction Solar Cells Through the Reduction of Phase Separation via Solvent Additives. *Adv. Mater.* **2010**, *22*, E63–E66.

(59) Schmidt, K.; Tassone, C. J.; Niskala, J. R.; Yiu, A. T.; Lee, O. P.; Weiss, T. M.; Wang, C.; Fréchet, J. M. J.; Beaujuge, P. M.; Toney, M. F. A Mechanistic Understanding of Processing Additive-Induced Efficiency Enhancement in Bulk Heterojunction Organic Solar Cells. *Adv. Mater.* **2014**, *26*, 300–305.

(60) Schmidt-Hansberg, B.; Sanyal, M.; Klein, M. F. G.; Pfaff, M.; Schnabel, N.; Jaiser, S.; Vorobiev, A.; Müller, E.; Colsmann, A.; Scharfer, P.; et al. Moving through the Phase Diagram: Morphology Formation in Solution Cast Polymer–Fullerene Blend Films for Organic Solar Cells. *ACS Nano* **2011**, *5*, 8579–8590.

(61) Verploegen, E.; Mondal, R.; Bettinger, C. J.; Sok, S.; Toney, M. F.; Bao, Z. Effects of Thermal Annealing Upon the Morphology of Polymer-Fullerene Blends. *Adv. Funct. Mater.* **2010**, *20*, 3519–3529.

(62) Savenije, T. J.; Kroeze, J. E.; Yang, X.; Loos, J. The Effect of Thermal Treatment on the Morphology and Charge Carrier Dynamics in a Polythiophene-Fullerene Bulk Heterojunction. *Adv. Funct. Mater.* **2005**, *15*, 1260–1266.

(63) Padinger, F.; Rittberger, R. S.; Sariciftci, N. S. Effects of Postproduction Treatment on Plastic Solar Cells. *Adv. Funct. Mater.* **2003**, *13*, 85–88.

(64) Yang, X.; Loos, J.; Veenstra, S. C.; Verhees, W. J. H.; Wienk, M. M.; Kroon, J. M.; Michels, M. A. J.; Janssen, R. A. J. Nanoscale Morphology of High-Performance Polymer Solar Cells. *Nano Lett.* **2005**, *5*, 579.

(65) Lindqvist, C.; Sanz-Velasco, A.; Wang, E.; Bäcke, O.; Gustafsson, S.; Olsson, E.; Andersson, M. R.; Müller, C. Nucleation-Limited Fullerene Crystallisation in a Polymer–fullerene Bulk-Heterojunction Blend. *J. Mater. Chem. A* **2013**, *1*, 7174.

(66) Müller, C. On the Glass Transition of Polymer Semiconductors and Its Impact on Polymer Solar Cell Stability. *Chem. Mater.* **2015**, *27*, 2740–2754.

(67) Cho, S.; Seo, J. H.; Park, S. H.; Beaupré, S.; Leclerc, M.; Heeger, A. J. A Thermally Stable Semiconducting Polymer. *Adv. Mater.* **2010**, *22*, 1253–1257.

(68) Müller, C.; Bergqvist, J.; Vandewal, K.; Tvingstedt, K.; Anselmo, A. S.; Magnusson, R.; Alonso, M. I.; Moons, E.; Arwin, H.; Campoy-Quiles, M.; et al. Phase Behaviour of Liquid-Crystalline Polymer/Fullerene Organic Photovoltaic Blends: Thermal Stability and

Miscibility. *J. Mater. Chem.* **2011**, *21*, 10676.

(69) Vogelsang, J.; Brazard, J.; Adachi, T.; Bolinger, J. C.; Barbara, P. F. Watching the Annealing Process One Polymer Chain at a Time. *Angew. Chemie Int. Ed.* **2011**, *50*, 2257–2261.

(70) Li, G.; Shrotriya, V.; Huang, J.; Yao, Y.; Moriarty, T.; Emery, K.; Yang, Y. High-Efficiency Solution Processable Polymer Photovoltaic Cells by Self-Organization of Polymer Blends. *Nat. Mater.* **2005**, *4*, 864–868.

(71) Jin, C.; Olsen, B. C.; Luber, E. J.; Buriak, J. M. Nanopatterning via Solvent Vapor Annealing of Block Copolymer Thin Films. *Chem. Mater.* **2017**, *29*, 176–188.

(72) Park, J. H.; Kim, J. S.; Lee, J. H.; Lee, W. H.; Cho, K. Effect of Annealing Solvent Solubility on the Performance of Poly(3-Hexylthiophene)/Methanofullerene Solar Cells. *J. Phys. Chem. C* **2009**, *113*, 17579–17584.

(73) Zhao, Y.; Xie, Z.; Qu, Y.; Geng, Y.; Wang, L. Solvent-Vapor Treatment Induced Performance Enhancement of Poly(3-Hexylthiophene):Methanofullerene Bulk-Heterojunction Photovoltaic Cells. *Appl. Phys. Lett.* **2007**, *90*, 043504.

(74) Li, G.; Yao, Y.; Yang, H.; Shrotriya, V.; Yang, G.; Yang, Y. "Solvent Annealing" Effect in Polymer Solar Cells Based on Poly(3-Hexylthiophene) and Methanofullerenes. *Adv. Funct. Mater.* **2007**, *17*, 1636–1644.

(75) Hu, S.; Dyck, O.; Chen, H.; Hsiao, Y.; Hu, B.; Duscher, G.; Dadmun, M.; Khomami, B. The Impact of Selective Solvents on the Evolution of Structure and Function in Solvent Annealed Organic Photovoltaics. *RSC Adv.* **2014**, *4*, 27931–27938.

(76) Chen, H.; Hu, S.; Zang, H.; Hu, B.; Dadmun, M. Precise Structural Development and Its Correlation to Function in Conjugated Polymer: Fullerene Thin Films by Controlled Solvent Annealing. *Adv. Funct. Mater.* **2013**, *23*, 1701–1710.

(77) Tang, H.; Lu, G.; Li, L.; Li, J.; Wang, Y.; Yang, X. Precise Construction of PCBM Aggregates for Polymer Solar Cellsvia Multi-Step Controlled Solvent Vapor Annealing. *J. Mater. Chem.* **2010**, *20*, 683–688.

(78) McAfee, S. M.; Dayneko, S. V.; Josse, P.; Blanchard, P.; Cabanetos, C.; Welch, G. C. Simply Complex: The Efficient Synthesis of an Intricate Molecular Acceptor for High-Performance Air-Processed and Air-Tested Fullerene-Free Organic Solar Cells. *Chem. Mater.* **2017**, *29*, 1309–1314.

(79) Sun, K.; Xiao, Z.; Hanssen, E.; Klein, M. F. G.; Dam, H. H.; Pfaff, M.; Gerthsen, D.; Wong, W. W. H.; Jones, D. J. The Role of Solvent Vapor Annealing in Highly Efficient Air-Processed Small Molecule Solar Cells. *J. Mater. Chem. A* **2014**, *2*, 9048–9054.

(80) Viterisi, A.; Gispert-Guirado, F.; Ryan, J. W.; Palomares, E. Formation of Highly Crystalline and Texturized Donor Domains in DPP(TBFu)2:PC71BM SM-BHJ Devices via Solvent Vapour Annealing: Implications for Device Function. *J. Mater. Chem.* **2012**, *22*, 15175.

(81) Zheng, Y.; Li, S.; Zheng, D.; Yu, J. Effects of Different Polar Solvents for Solvent Vapor Annealing Treatment on the Performance of Polymer Solar Cells. *Org. Electron.* **2014**, *15*, 2647–2653.

(82) Lan, S.; Yang, H.; Zhang, G.; Wu, X.; Chen, Q.; Chen, L.; Chen, H.; Guo, T. Importance of Solvent Removal Rate on the Morphology and Device Performance of Organic

Photovoltaics with Solvent Annealing. *ACS Appl. Mater. Interfaces* **2017**, *9*, 20679–20685.

(83) Liu, J.; Liang, Q.; Wang, H.; Li, M.; Han, Y.; Xie, Z.; Wang, L. Improving the Morphology of PCDTBT:PC $_{70}$ BM Bulk Heterojunction by Mixed-Solvent Vapor-Assisted Imprinting: Inhibiting Intercalation, Optimizing Vertical Phase Separation, and Enhancing Photon Absorption. *J. Phys. Chem. C* **2014**, *118*, 4585–4595.

(84) Lu, G.; Li, L.; Yang, X. Morphology and Crystalline Transition of Poly(3-Butylthiophene) Associated with Its Polymorphic Modifications. *Macromolecules* **2008**, *41*, 2062–2070.

(85) Chen, H.; Hsiao, Y.-C.; Hu, B.; Dadmun, M. Control of Morphology and Function of Low Band Gap Polymer–bis-Fullerene Mixed Heterojunctions in Organic Photovoltaics with Selective Solvent Vapor Annealing. *J. Mater. Chem. A* **2014**, *2*, 9883–9890.

(86) Chen, H.; Hsiao, Y.-C.; Hu, B.; Dadmun, M. Tuning the Morphology and Performance of Low Bandgap Polymer:Fullerene Heterojunctions via Solvent Annealing in Selective Solvents. *Adv. Funct. Mater.* **2014**, *24*, 5129–5136.

(87) Sinturel, C.; Vayer, M.; Morris, M.; Hillmyer, M. A. Solvent Vapor Annealing of Block Polymer Thin Films. *Macromolecules* **2013**, *46*, 5399–5415.

(88) Gotrik, K. W.; Hannon, A. F.; Son, J. G.; Keller, B.; Alexander-Katz, A.; Ross, C. A. Morphology Control in Block Copolymer Films Using Mixed Solvent Vapors. *ACS Nano* **2012**, *6*, 8052–8059.

(89) Stahl, B. C.; Kramer, E. J.; Hawker, C. J.; Lynd, N. A. Controlled Co-Solvent Vapor Annealing and the Importance of Quenching Conditions in Thin-Film Block Copolymer

Self-Assembly. *J. Polym. Sci. Part B Polym. Phys.* **2017**, *55*, 1125–1130.

(90) Park, S.; Kim, B.; Xu, J.; Hofmann, T.; Ocko, B. M.; Russell, T. P. Lateral Ordering of Cylindrical Microdomains Under Solvent Vapor. *Macromolecules* **2009**, *42*, 1278–1284.

(91) Zhang, J.; Posselt, D.; Sepe, A.; Shen, X.; Perlich, J.; Smilgies, D.-M.; Papadakis, C. M. Structural Evolution of Perpendicular Lamellae in Diblock Copolymer Thin Films during Solvent Vapor Treatment Investigated by Grazing-Incidence Small-Angle X-Ray Scattering. *Macromol. Rapid Commun.* **2013**, *34*, 1289–1295.

(92) Zhang, J.; Posselt, D.; Smilgies, D.-M.; Perlich, J.; Kyriakos, K.; Jaksch, S.; Papadakis, C. M. Lamellar Diblock Copolymer Thin Films during Solvent Vapor Annealing Studied by GISAXS: Different Behavior of Parallel and Perpendicular Lamellae. *Macromolecules* **2014**, *47*, 5711–5718.

(93) Gunkel, I.; Gu, X.; Sun, Z.; Schaible, E.; Hexemer, A.; Russell, T. P. An *in Situ* GISAXS Study of Selective Solvent Vapor Annealing in Thin Block Copolymer Films: Symmetry Breaking of in-Plane Sphere Order upon Deswelling. *J. Polym. Sci. Part B Polym. Phys.* **2016**, *54*, 331–338.

(94) Bai, W.; Yager, K. G.; Ross, C. A. *In Situ* Characterization of the Self-Assembly of a Polystyrene–Polydimethylsiloxane Block Copolymer during Solvent Vapor Annealing. *Macromolecules* **2015**, *48*, 8574–8584.

(95) Knoll, A.; Magerle, R.; Krausch, G. Phase Behavior in Thin Films of Cylinder-Forming Block Copolymers: Experiments Fluctuation Effects in the Theory of Microphase Separation in Block Copolymers Phase Behavior in Thin Films of Cylinder-Forming ABA Block Copolymers: Experiments. *J. Chem. Phys.* **2004**, *120*, 1105–1117.

(96) Albert, J. N. L.; Bogart, T. D.; Lewis, R. L.; Beers, K. L.; Fasolka, M. J.; Hutchison, J. B.; Vogt, B. D.; Epps, T. H. Gradient Solvent Vapor Annealing of Block Copolymer Thin Films Using a Microfluidic Mixing Device. *Nano Lett.* **2011**, *11*, 1351–1357.

(97) Cavicchi, K. A.; Russell, T. P. Solvent Annealed Thin Films of Asymmetric Polyisoprene−Polylactide Diblock Copolymers. *Macromolecules* **2007**, *40*, 1181–1186.

(98) Albert, J. N. L.; Young, W.-S.; Lewis, R. L.; Bogart, T. D.; Smith, J. R.; Epps, T. H. Systematic Study on the Effect of Solvent Removal Rate on the Morphology of Solvent Vapor Annealed ABA Triblock Copolymer Thin Films. *ACS Nano* **2012**, *6*, 459–466.

(99) Zomerman, D.; Kong, J.; McAfee, S. M.; Welch, G. C.; Kelly, T. L. Control and Characterization of Organic Solar Cell Morphology Through Variable-Pressure Solvent Vapor Annealing. *ACS Appl. Energy Mater.* **2018**, acsaem.8b01214.

(100) Crossland, E. J. W.; Rahimi, K.; Reiter, G.; Steiner, U.; Ludwigs, S. Systematic Control of Nucleation Density in Poly(3-Hexylthiophene) Thin Films. *Adv. Funct. Mater.* **2011**, *21*, 518–524.

(101) Crossland, E. J. W.; Tremel, K.; Fischer, F.; Rahimi, K.; Reiter, G.; Steiner, U.; Ludwigs, S. Anisotropic Charge Transport in Spherulitic Poly(3-Hexylthiophene) Films. *Adv. Mater.* **2012**, *24*, 839–844.

(102) Dang, M. T.; Hirsch, L.; Wantz, G. P3HT:PCBM, Best Seller in Polymer Photovoltaic Research. *Adv. Mater.* **2011**, *23*, 3597–3602.

(103) Kleinschmidt, A. T.; Root, S. E.; Lipomi, D. J. Poly(3-Hexylthiophene) (P3HT): Fruit Fly or Outlier in Organic Solar Cell Research? *J. Mater. Chem. A* **2017**, *5*, 11396–11400.

(104) Andrienko, D.; Brinkmann, M.; Daoulas, K.; Djurado, D.; Hartmann, L.; Kayunkid, N.; Ludwigs, S.; Luscombe, C. K.; Moulé, A. J.; Neher, D.; et al. *P3HT Revisited – From Molecular Scale to Solar Cell Devices*; Ludwigs, S., Ed.; Advances in Polymer Science; Springer Berlin Heidelberg: Berlin, Heidelberg, 2014; Vol. 265.

(105) Schilinsky, P.; Waldauf, C.; Brabec, C. J. Recombination and Loss Analysis in Polythiophene Based Bulk Heterojunction Photodetectors. *Appl. Phys. Lett.* **2002**, *81*, 3885–3887.

(106) McCullough, R. D. The Chemistry of Conducting Polythiophenes. *Adv. Mater.* **1998**, *10*, 93–116.

(107) Holliday, S.; Ashraf, R. S.; Wadsworth, A.; Baran, D.; Yousaf, S. A.; Nielsen, C. B.; Tan, C.-H.; Dimitrov, S. D.; Shang, Z.; Gasparini, N.; et al. High-Efficiency and Air-Stable P3HT-Based Polymer Solar Cells with a New Non-Fullerene Acceptor. *Nat. Commun.* **2016**, *7*, 11585.

(108) Savagatrup, S.; Printz, A. D.; O'Connor, T. F.; Zaretski, A. V.; Rodriquez, D.; Sawyer, E. J.; Rajan, K. M.; Acosta, R. I.; Root, S. E.; Lipomi, D. J. Mechanical Degradation and Stability of Organic Solar Cells: Molecular and Microstructural Determinants. *Energy Environ. Sci.* **2015**, *8*, 55–80.

(109) Spano, F. C.; Silva, C. H- and J-Aggregate Behavior in Polymeric Semiconductors. *Annu. Rev. Phys. Chem.* **2014**, *65*, 477–500.

(110) Telfer, S. G.; McLean, T. M.; Waterland, M. R. Exciton Coupling in Coordination Compounds. *Dalt. Trans.* **2011**, *40*, 3097.

(111) Clark, J.; Chang, J.-F.; Spano, F. C.; Friend, R. H.; Silva, C. Determining Exciton Bandwidth and Film Microstructure in Polythiophene Films Using Linear Absorption Spectroscopy. *Appl. Phys. Lett.* **2009**, *94*, 163306.

(112) Clark, J.; Silva, C.; Friend, R. H.; Spano, F. C. Role of Intermolecular Coupling in the Photophysics of Disordered Organic Semiconductors: Aggregate Emission in Regioregular Polythiophene. *Phys. Rev. Lett.* **2007**, *98*, 206406.

(113) Zhang, S.; Ye, L.; Hou, J. Breaking the 10% Efficiency Barrier in Organic Photovoltaics: Morphology and Device Optimization of Well-Known PBDTTT Polymers. *Adv. Energy Mater.* **2016**, *6*, 1502529.

(114) Cheng, P.; Li, G.; Zhan, X.; Yang, Y. Next-Generation Organic Photovoltaics Based on Non-Fullerene Acceptors. *Nat. Photonics* **2018**, *12*, 131–142.

(115) Yan, C.; Barlow, S.; Wang, Z.; Yan, H.; Jen, A. K.-Y.; Marder, S. R.; Zhan, X. Non-Fullerene Acceptors for Organic Solar Cells. *Nat. Rev. Mater.* **2018**, *3*, 18003.

(116) Hou, J.; Inganäs, O.; Friend, R. H.; Gao, F. Organic Solar Cells Based on Non-Fullerene Acceptors. *Nat. Mater.* **2018**, *17*, 119–128.

(117) Zhang, G.; Zhao, J.; Chow, P. C. Y.; Jiang, K.; Zhang, J.; Zhu, Z.; Zhang, J.; Huang, F.; Yan, H. Nonfullerene Acceptor Molecules for Bulk Heterojunction Organic Solar Cells. *Chem. Rev.* **2018**, *118*, 3447–3507.

(118) Zhou, H.; Yang, L.; You, W. Rational Design of High Performance Conjugated Polymers for Organic Solar Cells. *Macromolecules* **2012**, *45*, 607–632.

(119) Mondal, R.; Ko, S.; Norton, J. E.; Miyaki, N.; Becerril, H. A.; Verploegen, E.; Toney, M.

F.; Brédas, J.-L.; McGehee, M. D.; Bao, Z. Molecular Design for Improved Photovoltaic Efficiency: Band Gap and Absorption Coefficient Engineering. *J. Mater. Chem.* **2009**, *19*, 7195.

(120) Randell, N. M.; Radford, C. L.; Yang, J.; Quinn, J.; Hou, D.; Li, Y.; Kelly, T. L. Effect of Acceptor Unit Length and Planarity on the Optoelectronic Properties of Isoindigo–Thiophene Donor–Acceptor Polymers. *Chem. Mater.* **2018**, acs.chemmater.8b02535.

(121) van Pruissen, G. W. P.; Brebels, J.; Hendriks, K. H.; Wienk, M. M.; Janssen, R. A. J. Effects of Cross-Conjugation on the Optical Absorption and Frontier Orbital Levels of Donor–Acceptor Polymers. *Macromolecules* **2015**, *48*, 2435–2443.

(122) Ganguly, A.; Zhu, J.; Kelly, T. L. Effect of Cross-Conjugation on Derivatives of Benzoisoindigo, an Isoindigo Analogue with an Extended π-System. *J. Phys. Chem. C* **2017**, *121*, 9110–9119.

(123) Engmann, S.; Ro, H. W.; Herzing, A.; Snyder, C. R.; Richter, L. J.; Geraghty, P. B.; Jones, D. J. Film Morphology Evolution during Solvent Vapor Annealing of Highly Efficient Small Molecule Donor/Acceptor Blends. *J. Mater. Chem. A* **2016**, *4*, 15511–15521.

(124) Bin, H.; Yao, J.; Yang, Y.; Angunawela, I.; Sun, C.; Gao, L.; Ye, L.; Qiu, B.; Xue, L.; Zhu, C.; et al. High-Efficiency All-Small-Molecule Organic Solar Cells Based on an Organic Molecule Donor with Alkylsilyl-Thienyl Conjugated Side Chains. *Adv. Mater.* **2018**, *30*, 1706361.

(125) Bin, H.; Yang, Y.; Zhang, Z.-G.; Ye, L.; Ghasemi, M.; Chen, S.; Zhang, Y.; Zhang, C.; Sun, C.; Xue, L.; et al. 9.73% Efficiency Nonfullerene All Organic Small Molecule Solar

Cells with Absorption-Complementary Donor and Acceptor. *J. Am. Chem. Soc.* **2017**, *139*, 5085–5094.

(126) Qiu, B.; Xue, L.; Yang, Y.; Bin, H.; Zhang, Y.; Zhang, C.; Xiao, M.; Park, K.; Morrison, W.; Zhang, Z.-G.; et al. All-Small-Molecule Nonfullerene Organic Solar Cells with High Fill Factor and High Efficiency over 10%. *Chem. Mater.* **2017**, *29*, 7543–7553.

(127) Nielsen, C. B.; Holliday, S.; Chen, H.-Y.; Cryer, S. J.; McCulloch, I. Non-Fullerene Electron Acceptors for Use in Organic Solar Cells. *Acc. Chem. Res.* **2015**, *48*, 2803–2812.

(128) Liu, Z.; Wu, Y.; Zhang, Q.; Gao, X. Non-Fullerene Small Molecule Acceptors Based on Perylene Diimides. *J. Mater. Chem. A* **2016**, *4*, 17604–17622.

(129) Zhan, C.; Yao, J. More than Conformational "Twisting" or "Coplanarity": Molecular Strategies for Designing High-Efficiency Nonfullerene Organic Solar Cells. *Chem. Mater.* **2016**, *28*, 1948–1964.

(130) Zhang, Z.; Zhan, C.; Zhang, X.; Zhang, S.; Huang, J.; Li, A. D. Q.; Yao, J. A Self-Assembly Phase Diagram from Amphiphilic Perylene Diimides. *Chem. - A Eur. J.* **2012**, *18*, 12305–12313.

(131) Yan, Q.; Zhou, Y.; Zheng, Y.-Q.; Pei, J.; Zhao, D. Towards Rational Design of Organic Electron Acceptors for Photovoltaics: A Study Based on Perylenediimide Derivatives. *Chem. Sci.* **2013**, *4*, 4389.

(132) Lin, Y.; Zhan, X. Oligomer Molecules for Efficient Organic Photovoltaics. *Acc. Chem. Res.* **2016**, *49*, 175–183.

(133) Meng, D.; Sun, D.; Zhong, C.; Liu, T.; Fan, B.; Huo, L.; Li, Y.; Jiang, W.; Choi, H.; Kim,

T.; et al. High-Performance Solution-Processed Non-Fullerene Organic Solar Cells Based on Selenophene-Containing Perylene Bisimide Acceptor. *J. Am. Chem. Soc.* **2016**, *138*, 375–380.

(134) Cann, J.; Dayneko, S.; Sun, J.-P.; Hendsbee, A. D.; Hill, I. G.; Welch, G. C. N-Annulated Perylene Diimide Dimers: Acetylene Linkers as a Strategy for Controlling Structural Conformation and the Impact on Physical, Electronic, Optical and Photovoltaic Properties. *J. Mater. Chem. C* **2017**, *5*, 2074–2083.

(135) Zhang, J.; Li, Y.; Huang, J.; Hu, H.; Zhang, G.; Ma, T.; Chow, P. C. Y.; Ade, H.; Pan, D.; Yan, H. Ring-Fusion of Perylene Diimide Acceptor Enabling Efficient Nonfullerene Organic Solar Cells with a Small Voltage Loss. *J. Am. Chem. Soc.* **2017**, *139*, 16092–16095.

(136) Duan, Y.; Xu, X.; Yan, H.; Wu, W.; Li, Z.; Peng, Q. Pronounced Effects of a Triazine Core on Photovoltaic Performance-Efficient Organic Solar Cells Enabled by a PDI Trimer-Based Small Molecular Acceptor. *Adv. Mater.* **2017**, *29*, 1605115.

(137) Yao, H.; Ye, L.; Hou, J.; Jang, B.; Han, G.; Cui, Y.; Su, G. M.; Wang, C.; Gao, B.; Yu, R.; et al. Achieving Highly Efficient Nonfullerene Organic Solar Cells with Improved Intermolecular Interaction and Open-Circuit Voltage. *Adv. Mater.* **2017**, *29*, 1700254.

(138) Bennet, D. W. *Understanding Single-Crystal X-Ray Crystallography*; WILEY-VCH Verlag GmbH & Co KGaA, 2010.

(139) Abakumov, A. M.; Abrahams, J. P.; Andreev, Y. G.; Avilov, A.; Baerlocher, C.; Billinge, S. J. L.; Chukhovskii, F. N.; Cerny, R.; Curfs, C.; David, W. I. F.; et al. *Uniting Electron Crystallography and Powder Diffraction*; Kolb, U., Shankland, K., Meshi, L., Avilov, A.,

David, W., Eds.; Springer: Dordrecht, 2012.

(140) David, W. I. F.; Shankland, K. Structure Determination from Powder Diffraction Data. *Acta Crystallogr. Sect. A Found. Crystallogr.* **2008**, *64*, 52–64.

(141) Patterson, A. L. The Scherrer Formula for X-Ray Particle Size Determination. *Phys. Rev.* **1939**, *56*, 978–982.

(142) Hexemer, A.; Müller-Buschbaum, P. Advanced Grazing-Incidence Techniques for Modern Soft-Matter Materials Analysis. *IUCrJ* **2015**, *2*, 106–125.

(143) Willmott, P. *An Introduction to Synchrotron Radiation: Techniques and Applications*; John Wiley and Sons: West Sussex, 2011.

(144) Jiang, Z.; IUCr. *GIXSGUI* : A MATLAB Toolbox for Grazing-Incidence X-Ray Scattering Data Visualization and Reduction, and Indexing of Buried Three-Dimensional Periodic Nanostructured Films. *J. Appl. Crystallogr.* **2015**, *48*, 917–926.

(145) Wright, A. F.; Talbot, J.; Fender, B. E. F. Nucleation and Growth Studies by Small Angle Neutron Scattering and Results for a Glass Ceramic. *Nature* **1979**, *277*, 366–368.

(146) Jenkins, R.; Snyder, R. L. *Introduction to X-Ray Powder Diffraction*; John Wiley and Sons, 1996.

(147) DeLongchamp, D. M.; Kline, R. J.; Fischer, D. A.; Richter, L. J.; Toney, M. F. Molecular Characterization of Organic Electronic Films. *Adv. Mater.* **2011**, *23*, 319–337.

(148) Yang, H.; LeFevre, S. W.; Ryu, C. Y.; Bao, Z. Solubility-Driven Thin Film Structures of Regioregular Poly(3-Hexyl Thiophene) Using Volatile Solvents. *Appl. Phys. Lett.* **2007**, *90*, 172116.

(149) Gargi, D.; Kline, R. J.; DeLongchamp, D. M.; Fischer, D. A.; Toney, M. F.; O'Connor, B. T. Charge Transport in Highly Face-On Poly(3-Hexylthiophene) Films. *J. Phys. Chem. C* **2013**, *117*, 17421–17428.

(150) Sirringhaus, H.; Brown, P. J.; Friend, R. H.; Nielsen, M. M.; Bechgaard, K.; Langeveld-Voss, B. M. W.; Spiering, A. J. H.; Janssen, R. A. J.; Meijer, E. W.; Herwig, P.; et al. Two-Dimensional Charge Transport in Self-Organized, High-Mobility Conjugated Polymers. *Nature* **1999**, *401*, 685–688.

(151) DeLongchamp, D. M.; Vogel, B. M.; Jung, Y.; Gurau, M. C.; Richter, C. A.; Kirillov, O. A.; Obrzut, J.; Fischer, D. A.; Sambasivan, S.; Richter, L. J.; et al. Variations in Semiconducting Polymer Microstructure and Hole Mobility with Spin-Coating Speed. *Chem. Mater.* **2005**, *17*, 5610–5612.

(152) Zhao, F.; Wang, C.; Zhan, X. Morphology Control in Organic Solar Cells. *Adv. Energy Mater.* **2018**, 1703147.

(153) Dang, M. T.; Hirsch, L.; Wantz, G.; Wuest, J. D. Controlling the Morphology and Performance of Bulk Heterojunctions in Solar Cells. Lessons Learned from the Benchmark Poly(3-Hexylthiophene):[6,6]-Phenyl-C 61 -Butyric Acid Methyl Ester System. *Chem. Rev.* **2013**, *113*, 3734–3765.

(154) Bao, Z.; Dodabalapur, A.; Lovinger, A. J. Soluble and Processable Regioregular Poly(3-hexylthiophene) for Thin Film Field-effect Transistor Applications with High Mobility. *Appl. Phys. Lett.* **1998**, *69*, 4108.

(155) Wang, D.; Russell, T. P. Advances in Atomic Force Microscopy for Probing Polymer Structure and Properties. *Macromolecules* **2018**, *51*, 3–24.

(156) Tennyson, E. M.; Gong, C.; Leite, M. S. Imaging Energy Harvesting and Storage Systems at the Nanoscale. *ACS Energy Lett.* **2017**, *2*, 2761–2777.

(157) *Atomic Force Microscopy in Biomedical Research*; Braga, P. C., Ricci, D., Eds.; Methods in Molecular Biology; Humana Press: Totowa, NJ, 2011; Vol. 736.

(158) Gross, L.; Mohn, F.; Moll, N.; Liljeroth, P.; Meyer, G. The Chemical Structure of a Molecule Resolved by Atomic Force Microscopy. *Science* **2009**, *325*, 1110–1114.

(159) García, R.; San Paulo, A. Attractive and Repulsive Tip-Sample Interaction Regimes in Tapping-Mode Atomic Force Microscopy. *Phys. Rev. B* **1999**, *60*, 4961–4967.

(160) Tamayo, J.; García, R. Relationship between Phase Shift and Energy Dissipation in Tapping-Mode Scanning Force Microscopy. *Appl. Phys. Lett.* **1998**, No. 73, 2926.

(161) McLean, R. S.; Sauer, B. B. Tapping-Mode AFM Studies Using Phase Detection for Resolution of Nanophases in Segmented Polyurethanes and Other Block Copolymers. *Macromolecules* **1997**, *30*, 8314–8317.

(162) Jovanov, V.; Yumnam, N.; Müller, A.; Gruber, M.; Wagner, V. Determining Material-Specific Morphology of Bulk-Heterojunction Organic Solar Cells Using AFM Phase Imaging. *J. Phys. Chem. C* **2017**, *121*, 9173–9180.

(163) Nowak, D.; Morrison, W.; Wickramasinghe, H. K.; Jahng, J.; Potma, E.; Wan, L.; Ruiz, R.; Albrecht, T. R.; Schmidt, K.; Frommer, J.; et al. Nanoscale Chemical Imaging by Photoinduced Force Microscopy. *Sci. Adv.* **2016**, *2*, e1501571.

(164) Hotta, S.; Rughooputh, S. D. D. V.; Heeger, A. J.; Wudl, F. Spectroscopic Studies of Soluble Poly(3-Alkylthienylenes). *Macromolecules* **1987**, *20*, 212–215.

(165) Payne, A.-J.; Rice, N. A.; McAfee, S. M.; Li, S.; Josse, P.; Cabanetos, C.; Risko, C.; Lessard, B. H.; Welch, G. C. Donor or Acceptor? How Selection of the Rylene Imide End Cap Impacts the Polarity of π-Conjugated Molecules for Organic Electronics. *ACS Appl. Energy Mater.* **2018**, *1*, 4906–4916.

(166) Al-Hussein, M.; Herzig, E. M.; Schindler, M.; Löhrer, F.; Palumbiny, C. M.; Wang, W.; Roth, S. V.; Müller-Buschbaum, P. Comparative Study of the Nanomorphology of Spray and Spin Coated PTB7 Polymer: Fullerene Films. *Polym. Eng. Sci.* **2016**, *56*, 889–894.

(167) Chao, P.; Mu, Z.; Wang, H.; Mo, D.; Chen, H.; Meng, H.; Chen, W.; He, F. Chlorination of Side Chains: A Strategy for Achieving a High Open Circuit Voltage Over 1.0 V in Benzo[1,2-b:4,5-B′]Dithiophene-Based Non-Fullerene Solar Cells. *ACS Appl. Energy Mater.* **2018**, *1*, 2365–2372.